

Computational analysis of Asphalt binder based on Phase Field Method

Yue Hou

Dissertation submitted to the faculty of
Virginia Polytechnic Institute and State University
in partial fulfillment of the requirements for the degree of

Doctor of Philosophy
in
Civil Engineering

Linbing Wang, Chair
Pengtao Yue
Joseph Dove
Marwan Al-Haik,
Muhammad Hajj

March 17, 2014
Blacksburg, Virginia

Keywords: Asphalt binder; Computational analysis; Phase field modeling;
Microstructure evolution

Copyright 2014, Yue Hou

Computational analysis of Asphalt binder based on Phase Field Method

Yue Hou

(Abstract)

The mechanical performance evaluation of asphalt binder has always been a challenging issue for pavement engineers. Recently, the Phase Field Method (PFM) has emerged as a powerful computational tool to simulate the microstructure evolution of asphalt binder. PFM analyzes the structure from the free energy aspect and can provide a view of the whole microstructure evolution process. In this dissertation, asphalt binder performance is analyzed by PFM in three aspects: first, the relationship between asphalt chemistry and performance is investigated. The components of asphalt are simplified to three: asphaltene, resin and oil. Simulation results show that phase separation will occur under certain thermal conditions and result in an uneven distribution of residual thermal stress. Second, asphalt cracking is analyzed by PFM. The traditional approach to analyze crack propagation is Classic Fracture Mechanics first proposed by Griffith, which needs to clearly depict the crack front conditions and may cause complex cracking topologies. PFM describes the microstructure using a phase-field variable which assumes positive one in the intact solid and negative one in the crack void. The fracture toughness is modeled as the surface energy stored in the diffuse interface between the intact solid and crack void. To account for the growth of cracks, a non-conserved Allen-Cahn equation is adopted to evolve the phase-field variable. The energy based formulation of the phase-field method handles the competition between the growth of surface energy and release of elastic energy in a natural way: the crack propagation is a result of the energy minimization in the direction of the steepest descent. Both the linear elasticity and phase-field equation are solved in a unified finite element frame work, which is implemented in the commercial software COMSOL. Different crack mode simulations are performed for validation. It was discovered that the onset of crack propagation agrees very well with the Griffith criterion and experimental results. Third, asphalt self-healing phenomenon is studied based on the Atomic Force Microscopy (AFM) technology. The self-healing mechanism is simulated in two ways: thermodynamic approach and mechanical approach. Cahn-Hilliard dynamics and Allen-Cahn dynamics are adopted, respectively.

ACKNOWLEDGEMENTS

First, the author would like to give his sincere appreciation to his advisor, Dr Linbing Wang. Under his visionary advising, kind encouragement, persistent support, the author can finish the PhD research.

The author would also like to thank his co-advisor Dr Pengtao Yue for his patient guidance and valuable advices in the phase field research and applied mathematics area.

The author wants to thank all his committee members Dr Marwan Al-Hiak, Dr Muhammad Hajj and Dr Joseph Dove for their kind help and advises.

The author would also want to thank Dr Dong Wang, Dr Troy Pauli and Wenjuan Sun and all his friends for their kind help in this thesis and assistance during his PhD study at Virginia Polytechnic Institute and State University.

CONTENTS

Chapter 1. Introduction and Literature Review.....	1
1.1 Background.....	1
1.2 Free energy and phase-field equations.....	2
1.3 Application of PFM in asphalt analysis	4
1.4 Literature review and weak forms of Allen-Cahn dynamics and Cahn-Hilliard dynamics	6
REFERENCES	15
Chapter 2. Asphalt mechanical property based on asphalt chemistry by Phase-field modeling.....	22
2.1 Introduction.....	22
2.2 Marcusson model based on asphalt chemistry	23
2.3 Phase field model.....	24
2.4 Numerical simulations and results	28
2.4.1 Initialization of model.....	28
2.4.2 Coupled process of a diffuse interface model	29
2.5 Conclusions and Challenge.....	36
REFERENCES	37

Chapter 3. Fracture failure of asphalt binder by PFM	40
3.1 Introduction and literature review	40
3.2 Mode I cracking	43
3.2.1 Free energy.....	43
3.2.2 Phase-field model.....	45
3.2.3 Generalized Eshelby tensor and J - integral	47
3.2.4 Simulation of mode I crack propagation.....	50
3.2.5 Experiments and comparisons	53
3.2.6 Summary	62
3.3 Mode II cracking.....	63
3.4 Mixed Mode Cracking (Mode I & II)	67
3.4.1 Generalized Eshelby tensor and J - integral.....	67
3.4.2 A simple simulation	71
3.4.3 Cracking experiments and comparisons.....	74
3.4.4 Summary and conclusions	79
3.5 Crack interaction.....	80
3.5.1 Generalized Eshelby tensor and J - integral.....	81

3.5.2 Numerical simulation.....	82
3.5.3 Experiments and comparisons	86
3.5.4 Summary	89
REFERENCES	90
Chapter 4. Investigation of Asphalt Self-healing Mechanism Using Phase-field Model	94
4.1 Introduction.....	94
4.2 Atomic Force Microscopy	95
4.3 Phase-field Model	104
4.3.1 Material re-arrangement approach	104
4.3.2 Mechanical approach	111
4.4 Summary and conclusions	115
REFERENCES	116
Chapter 5. A Multi-scale Approach of Mode I crack in ettringite based on Phase-field Theory and Molecular Dynamic Simulation	119
5.1 Introduction.....	119
5.2 Multi-scale Modeling.....	122
5.2.2 Computational theory.....	123

5.2.3 Multi-scale Approach.....	125
5.3 Summary and discussion.....	134
REFERENCES	134
Chapter 6. Conclusions and future work.....	136
6.1 Overview.....	136
6.2 Major findings.....	136
6.3 Recommendations for future work	139
PUBLICATIONS SUMMARY	143

LIST OF FIGURES

Figure 2-1 A double-well potential.....	25
Figure 2-2 (a) The unstructured triangular mesh generated by COMSOL	28
Figure 2-3 Phase separation at $t= 0, 0.05s, 0.5s, 2s, 2.2s$ and $t =3 s$	30
Figure 2-4 Phase field variable distribution at the bottom boundary at $t=0.5s$	31
Figure 2-5 Contour plot of Von mises stress at $t= 0, 0.05s, 0.5s, 2s, 2.2s$ and $3s$	32
Figure 2-6 z component of stress tensor at $t=0.05s$	33
Figure 2-7 (a) xx component (b) yy component of stress tensor of bottom boundary at $t=0.5s$	35
Figure 2-8 xy component of stress tensor of bottom boundary at $t=0.5s$	35
Figure 2-9 Average stress distribution.....	36
Figure 3-1 Three modes of crack.....	41
Figure 3-2 Mode I cracking contour.....	49
Figure 3-3 (a) Unstructured triangular mesh generated by COMSOL (b) Magnified view of the crack.....	51
Figure 3-4 Pure tension loading is applied on our model.....	52
Figure 3-5 Magnified view of crack propagation.....	53
Figure 3-6 Geometry of asphalt binder specimen for crack testing.....	55
Figure 3-7 One representative fracture process with initial crack length 9 mm.....	56
Figure 3-8 One representative fracture process with initial crack length 8 mm.....	56
Figure 3-9 One representative fracture process with initial crack length 5 mm.....	57
Figure 3-10 The broken specimen after tension loading.....	57

Figure 3-11 Determination of the failure load with an initial V notch crack.....	61
Figure 3-12 Comparison of failure load with respect to surface energy between experiment and PFM.....	61
Figure 3-13 (a) Unstructured triangular mesh generated by COMSOL with interfacial refinement (b) Magnified view of crack.....	64
Figure 3-14 Opposite movements happens on top and bottom boundaries.....	65
Figure 3-15 Magnified view of crack propagation. The snapshots are taken at $t=0, 15 \Delta t, 20 \Delta t$ and $60 \Delta t$ where $\Delta t = 0.01s$ is the time step used in the simulation. $\gamma = 100 J/m^2$	65
Figure 3-16 Magnified view of von Mises stress distribution near crack tip at $t=30 \Delta t$	66
Figure 3-17 Phase field contour in the mixed mode cracking.....	69
Figure 3-18 (a) Unstructured triangular mesh generated by COMSOL with interfacial refinement. (b) Magnified view of the crack.....	71
Figure 3-19 Tension loading applied on the mixed mode cracking.....	73
Figure 3-20 Magnified view of crack propagation. The snapshots are taken at time step 0, 75, 76 and 84 where $\Delta t = 0.001s$. $\gamma = 200 J/m^2$. $E = 5.8 Mpa$	73
Figure 3-21 von Mises stress distribution at $t=0.076s$	74
Figure 3-22 The direction tension tester by Interlaken Technology Corporation.....	75
Figure 3-23 Geometry of standard asphalt binder specimen on DTT and the modified specimen by inserting aluminum sheet as the initial crack in Mode I cracking simulation.....	76
Figure 3-24 (a) The new made sample with crack length = 12 mm (b) broken sample after testing.....	79

Figure 3-25 Crack contour in crack interaction.....	81
Figure 3-26 (a) Unstructured triangular mesh generated by COMSOL with one initial crack (b) Mesh with two initial cracks.....	83
Figure 3-27 Pure tension loading is applied on our model.....	83
Figure 3-28 Crack interaction at different time instants.....	85
Figure 3-29 von Mises stress distribution.....	86
Figure 3-30 Geometry of asphalt binder specimen for crack testing.....	87
Figure 3-31 The broken specimen after tension loading.....	88
Figure 4-1 AFM images (l.h.s, phase contrast scans, r.h.s. topography scan) of AAC-1-C5 in a temperature increasing process at 19°C, 25°C and 28°C.....	100
Figure 4-2 AFM images of AAC-1-C5 in a temperature increasing process at 31°C, 34°C and 37°C.....	101
Figure 4-3 AFM images of AAC-1-C5 in a temperature increasing process at 40°C, 43°C, 46°C.....	102
Figure 4-4 AFM images of AAC-1-C5 in a decreasing temperature at 40 °C, 31 °C and 21°C.....	103
Figure 4-5 Schematic view of phase separation in terms of free energy and phase diagram.....	105
Figure 4-6 Phase separation during the temperature dropping process and the corresponding von Mises stress distribution contour plot.....	108
Figure 4-7 Phase mixing during the temperature rising process and the corresponding von Mises stress contour plot.....	109
Figure 4-8 Uneven double well potential.....	113

Figure 4-9 Cracking and self-healing at different time steps.....	115
Figure 5-1 Flowchart of multi-scale modeling scheme.....	121
Figure 5-2 Volume percentage of different phases in hydrated Portland cement paste, water/cement ratio = 0.5, hydrated for 14 months.....	123
Figure 5-3 2×2×1 supercell molecular structure of ettringite.....	125
Figure 5-4 (a) Unstructured triangular mesh generated by COMSOL with interfacial refinement. (b) Magnified view of the crack.....	127
Figure 5-5 Molecular structure of ettringite 2x4x1 in the molecular dynamics (MD) model: (a) & (b) initial view molecular structure of ettringite from different views (c) molecular structure after tension failure.....	128
Figure 5-6 Crack propagation in the multi-scale modeling at different time instants.....	130
Figure 5-7 Crack tip region in multi-scale system at t = 1.53s.....	131
Figure 5-8 Von mises stress distribution and magnified view of crack tip region by Phase-field at 1.53s.....	133
Figure 5-9 von Mises stress distribution after the multi-scale coupling.....	133
Figure 6-1 Phase-field Mode I viscoelastic fracture calculation flowchart.....	142

LIST OF TABLES

Table 2-1 The three - composition method of Asphalt based on Marcusson method.....	24
Table 3-1 Comparison of Critical Fracture Stress by Three Approaches.....	59
Table 3-2 Comparison of The Failure Load Between Experiment and PFM.....	62
Table 3-3 Comparison between experiment and PFM.....	89
Table 5-1 Elastic constants of ettringite by MD Simulation.....	126
Table 5-2 Stress comparison between Phase-field and MD.....	132

Chapter 1. Introduction and Literature Review

1.1 Background

Asphalt binder, known as the most important pavement material, is a product of the petrol industry. Due to its high use in the pavement structures, the mechanical performance of asphalt binder has always attracted the attention of pavement engineers. The traditional methods such as the Finite Element Method (FEM) have been successfully employed in the asphalt analysis with satisfactory accuracy [1, 2]. New methods including Discrete Element Method (DEM) [3] and Molecular Dynamic Simulation [4] are currently under development and have achieved significant progress.

Recently, Phase Field Method (PFM), which has a great advantage in simulation especially in visualization, is emerged as a new approach to solve the asphalt problem. The Phase-Field Method (PFM) was originally proposed by Cahn and Hilliard for the spinodal decomposition in phase transition [5]. In this model, a phase-field variable ϕ is introduced to identify different phases, based on which a free energy functional is constructed. The whole system evolves toward the direction which minimizes this free energy. Recently, this methodology has been extended to a variety of problems, e.g., fracture [6], interfacial flow [7], and tumor growth [8]. The phase field variable ϕ is used to identify different phases in the system, which is driven by the chemical potential that is the variation of the free energy with respect to the phase-field variable. Generally, PFM tries to solve the structural problem from the free energy aspect and can give a real-time development of the microstructure.

1.2 Free energy and phase-field equations

Considering an isothermal system, a model for a phase field can be constructed by physical arguments if one has an explicit expression for the free energy of the system.

$$\text{Gibbs free energy (G) [9]: NPT. } G = H - TS \quad (1-1)$$

$$\text{Helmholtz free energy (F) [9]: NVT. } F = U - TS \quad (1-2)$$

Consider Gibbs free energy (G) in our system. Under the isothermal and isobaric conditions, the spontaneous process is determined by $\Delta G < 0$ [9].

That is $\Delta G < 0$, the process is spontaneous;

$\Delta G > 0$, the process is not spontaneous;

$\Delta G = 0$, system comes to equilibrium.

Landau, Ginzburg *et al.* suggest a theory that combines the free energy F and the field variable ϕ [10]. It gives us the microstructure evolution process including the structure domain and the interface domain. The phase-field variable is defined and used to describe the whole domain state, e.g. for different state of the domain and corresponds to different chemical potentials.

Here we consider the phase-field parameter as the molar fraction. Suppose there exist n_A A atoms and n_B B atoms mixing together, the phase-field variable of A is defined as

$\phi = \frac{n_A}{n_A + n_B}$. Based on this definition, phase-field variable represents the quantitative measurement of concentration.

In the classic Landau-Ginzburg theory, the free energy is determined through the diffuse interface. The total free energy of an inhomogeneous microstructure system described by a set of conserved (c_1, c_2, \dots) and non-conserved (η_1, η_2, \dots) field variable is given by [11]

$$F = \int [f(c_1, c_2, \dots, c_n, \eta_1, \eta_2, \dots, \eta_n) + \sum_{i=1}^n \alpha_i (\nabla c_i)^2] + \sum_{i=1}^3 \sum_{j=1}^3 \sum_{k=1}^3 \beta_{ij} \nabla_i \eta_k \nabla_j \eta_k] d^3r + \iint G(r - r') d^3r d^3r' \quad (1-3)$$

where f is the local free energy, α_i and β_{ij} are the gradient energy coefficients, $G(r - r')$ refers to the nonlocal term that contributes to the total free energy density from long-range interactions.

A simple model of the total free energy can be given as

$$F = \int_{\Omega} f(\phi) + \frac{1}{2} \kappa |\nabla \phi|^2 d\Omega \quad (1-4)$$

where the first term $f(\phi)$ can be obtained by Molecular Dynamics (MD) Simulation or by doing experiments. The second term relates to the interfacial tension.

Based on Equation (1-4), the chemical potential G can be obtained as

$$G = \frac{\delta F}{\delta \phi} = f'(\phi) - \kappa \nabla^2 \phi \quad (1-5)$$

The physical meaning of the chemical potential is measurement of the maximum work that a system can make to alter itself [9].

The microstructure evolution is governed by two equations. For non-conservative situation, the development of microstructure is determined by the chemical potential and we have Allen-Cahn dynamics shown as [12]

$$\frac{\partial \phi}{\partial t} = -MG = M(\kappa \nabla^2 \phi - f'(\phi)) \quad (1-6)$$

For conservative situation, the development of microstructure is determined by the gradient of chemical potential and we adopt Cahn-Hilliard dynamics [5]

$$\frac{\partial \phi}{\partial t} = \nabla \cdot (M \nabla G) = \nabla \cdot [M \nabla (f'(\phi) - \kappa \nabla^2 \phi)] \quad (1-7)$$

Based on the abovementioned concepts of phase-field equations, it is obviously that PFM can depict the whole problem by using a concise phase-field variable whereas the traditional approach is unable to. Besides, there are only two governing equations (1-6) and (1-7)

considered in PFM and covers most of the situations we may counter in the actual problems: either conserve or non-conserve. And in this way, it is reasonable to apply PFM in the asphalt binder analysis.

1.3 Application of PFM in asphalt analysis

In our research, the asphalt microstructure is the key to understanding the asphalt mechanical performance. By employing the governing equations (1-6), (1-7) and apply the corresponding boundary conditions, the microstructure evolution process can then be determined and the corresponding mechanical performance at each time instant is obtained.

And then our problem comes to the solving of Equation (1-6) & (1-7). Note that both of the two are Partial Differential Equation (PDE), which can be mathematically solved by Finite Element Method (FEM) [13] and Finite Difference Method (FDM) [14]. In our analysis, we use a commercial finite element software COMSOL Multiphysics.

In this paper, we are trying to apply Phase field Method in the analysis of asphalt consisting of three parts:

The first is to determine the relationship between asphalt chemistry and the physical properties.

The chemical components of asphalt can be simplified into three components: asphaltene, resin, oil [15]. Consider that asphaltene takes a small portion in the asphalt, we believe resin and oil mainly dominate the asphalt physical and chemical property and a binary phase field model is then developed. Given different thermal conditions, phase separation will occur and lead to the change of local microstructure. The corresponding residual thermal stress can then be calculated.

The second is to determine the fracture failure of asphalt binder under different conditions. In the classic fracture mechanical theory, the single crack modes are divided into three: Mode I

(opening crack), Mode II (In-plane shear crack) and Mode III (Out-of-plane shear crack). In PFM, it describes the microstructure using a phase-field variable ϕ which assumes one in the intact solid and negative one in the crack region. The fracture toughness is modeled as the surface energy stored in the diffuse interface between the intact solid and crack void. To account for the growth of cracks, a non-conserved Allen-Cahn equation is adopted to evolve the phase-field variable. The energy based formulation of the phase-field method handles the competition between the growth of surface energy and release of elastic energy in a natural way: the crack propagation is a result of the energy minimization in the direction of the steepest descent. Both the linear elasticity and phase-field equation are solved in a unified finite element framework, which is implemented in the commercial software COMSOL. The mode I crack, mode II crack, mixed mode cracking (Mode I & II) and crack interaction simulation are performed with validation of corresponding experiments. It was discovered that the onset of crack propagation agrees very well with the Griffith criterion and experimental results.

The third is to study the self-healing mechanism of asphalt binder. Self-healing is always a challenging issue in the pavement industry. In this paper, we are trying to explain the self-healing mechanism of asphalt by using the Phase-field Model in two ways: thermodynamic approach and mechanical approach. In the thermodynamic approach, self-healing is considered as a material-phase-rearrangement process based on the Cahn-Hilliard dynamics. Micro-cracks will form and disappear in the stress concentration zone near the phase interfaces because of phase separation that is demonstrated by AFM results; in the mechanical approach, the microstructure is described using a phase-field variable which assumes positive one in the intact solid and negative one in the existing crack void. Allen-Cahn dynamics is adopted to evolve the

phase-field variable that the surface energy will result in the “wetting” of two surfaces and finally leads to self-healing.

Besides the three research fields, another interesting topic is the aging mechanism of asphalt binder, which is also a complex physical and chemical process while current researches are mainly considering the oxidation process as the main factor. Note that the oxidation is a process of diffusion, which is similar to the phenomenon describe by Equation (1-6) and (1-7). And aging may be a research hotspot of Phase field in the future.

1.4 Literature review and weak forms of Allen-Cahn dynamics and Cahn-Hilliard dynamics

The original Cahn-Hilliard theory is a modified equation, which is a continuous conservative model for the scalar order parameter ϕ , in the dimensionless form as [16]

$$\frac{\partial \phi}{\partial t}(\mathbf{r}, t) = \nabla^2 \left(\frac{\varepsilon}{2} \phi + 2\phi^3 - \nabla^2 \phi \right) + \xi(\mathbf{r}, t) \quad (1-8)$$

Note that $\varepsilon = \frac{T-T_c}{T_c}$, where T_c is the critical temperature of phase transition, is the controlling parameter in the system, $\xi(\mathbf{r}, t)$ is the random white noise, whose amplitude is proportional to the square root of the temperature [16].

Yue *et al.* (2004) expressed the mixing energy density as a function of ϕ and its gradient as [17]

$$f_{mix}(\phi, \nabla \phi) = \frac{1}{2} \lambda |\nabla \phi|^2 + f_0(\phi) \quad (1-9)$$

where the double-well potential for $f_0(\phi)$ is [17]

$$f_0(\phi) = \frac{\lambda}{4\varepsilon^2} (\phi^2 - 1)^2 \quad (1-10)$$

Note that in Phase-field model, the diffuse interface modeling is adopted. There have been many researches take advantage of the diffuse interface to circumvent certain numerical difficulties in tracking the interface in the classical sharp-interface model [18, 19, 20].

Boyer *et al.* (2010) constructed a three-phase free energy as [21]

$$F_{\Sigma}(\phi_1, \phi_2, \phi_3) = \int_{\Omega} \left[\frac{12}{\varepsilon} F(\phi_1, \phi_2, \phi_3) + \frac{3}{8} \varepsilon \Sigma_1 |\nabla \phi_1|^2 + \frac{3}{8} \varepsilon \Sigma_2 |\nabla \phi_2|^2 + \frac{3}{8} \varepsilon \Sigma_3 |\nabla \phi_3|^2 \right] \quad (1-13)$$

where ϕ_1, ϕ_2, ϕ_3 represents three different phases, respectively.

Wang *et al.* (2001) introduced crystalline energy as the local free energy density as [22]

$$f(\phi) = \Delta f \sin^2(\pi\phi) \quad (1-14)$$

where Δf is the energy barrier between two neighboring minima. The advantage of equation (1-14) is that it has infinite minima located at $\phi = -\infty, \dots, -1, 0, +1, \dots, +\infty$ [22].

The coupling of phase field with other physical field is a hot topic recently. Caginalp *et al.* (1992) suggested a equation coupling with temperature field as [23]

$$f(\phi, T) = 4\Delta f \left(-\frac{1}{2} \phi^2 + \frac{1}{4} \phi^4 \right) + \frac{15\alpha}{8} \left(\phi - \frac{2}{3} \phi^3 + \frac{1}{5} \phi^5 \right) (T - T_m) \quad (1-15)$$

where α is a positive constant, and T_m is the equilibrium melting temperature.

Nambu *et al.* (1994) gave the coupling of phase field with local electric polarization field for domain structure evolution during a cubic to tetragonal ferroelectric phase transition as [24]

$$\begin{aligned} f(P_1, P_2, P_3) = & A_1(P_1^2 + P_2^2 + P_3^2) + A_{11}(P_1^4 + P_2^4 + P_3^4) \\ & + A_{12}(P_1^2 P_2^2 + P_2^2 P_3^2 + P_1^2 P_3^2) + A_{111}(P_1^6 + P_2^6 + P_3^6) \\ & + A_{112}[P_1^4(P_2^2 + P_3^2) + P_2^4(P_1^2 + P_3^2) + P_3^4(P_1^2 + P_2^2)] \\ & + A_{123} P_1^2 P_2^2 P_3^2 \end{aligned} \quad (1-16)$$

The phase field could be employed in grain growth by extending the double well potential to one with finite number of minima as [25]

$$f(\phi_1, \phi_2, \dots) = 4\Delta f \left(-\frac{1}{2} \sum_i \phi_i^2 + \frac{1}{4} \sum_i \phi_i^4 \right) + \alpha \sum_i \sum_{j>1} \phi_i^2 \phi_j^2 \quad (1-17)$$

where α is a positive coefficient, and Δf is the energy barrier among the minima.

Braun *et al.* (1998) and Wang *et al.* (1998) introduced the local free-energy function in solid state phase transformations [26, 27]. In precipitation of an order phase in binary alloy, the local free energy density function is given by [24, 25, 26]

$$f(c, \eta_1, \eta_2, \eta_3) = f_d(c, T) + \frac{1}{2} A_2(c, T)(\eta_1^2 + \eta_2^2 + \eta_3^2) + \frac{1}{3} A_3(c, T)\eta_1\eta_2\eta_3 + \frac{1}{4} A_{41}(c, T)(\eta_1^4 + \eta_2^4 + \eta_3^4) + \frac{1}{4} A_{42}(c, T)(\eta_1^2\eta_2^2 + \eta_2^2\eta_3^2 + \eta_1^2\eta_3^2) \quad (1-18)$$

where $f_d(c, T)$ is the free energy of the disordered phase, and A_2 , A_3 , A_{41} and A_{42} are the expansion coefficients that are functions of temperature and composition [26, 27, 28].

Wang *et al.* (1997) gave the local free energy density following sixth-order expression for a cubic to tetragonal transformation as [29]

$$f(\eta_1, \eta_2, \eta_3) = \frac{1}{2} A \sum_{k=1}^3 \eta_k^2 - \frac{1}{4} B \sum_{k=1}^3 \eta_k^4 + \frac{1}{6} C (\sum_{k=1}^3 \eta_k^2)^3 \quad (1-19)$$

where A , B and C are positive constants.

Takada *et al.* (2006) coupled phase field with Navier-Stokes (N-S) equation in the fluid flow as [30]

$$\frac{\partial \rho}{\partial t} + \mathbf{u} \cdot \nabla \rho = 0 \quad (1-20)$$

$$\frac{\partial \mathbf{u}}{\partial t} + (\mathbf{u} \cdot \nabla) \mathbf{u} = \frac{1}{\rho} [-\nabla \cdot \mathbf{P} + \nabla \cdot \{\mu(\nabla \mathbf{u} + \nabla \mathbf{u}^T)\}] + (\rho - \rho_c) \mathbf{g} \quad (1-21)$$

$$\frac{\partial \phi}{\partial t} + \nabla \cdot (\phi \mathbf{u}) = -\nabla \cdot [-\Gamma \phi \nabla \eta] \quad (1-22)$$

where t is the time, \mathbf{u} the flow velocity and ρ is the density of two-phase fluid, \mathbf{g} is the gravity, \mathbf{P} the pressure tensor, μ the viscosity, and ρ_c denotes the density in continuous phase [30].

Badalassi *et al.* (2003) also suggested a coupled N-S phase field equation as [31]

$$Re \left(\frac{\partial \mathbf{u}}{\partial t} + \mathbf{u} \cdot \nabla \mathbf{u} \right) = -\nabla p + \nabla \cdot \theta (\nabla \mathbf{u} + \nabla \mathbf{u}^T) + \frac{1}{Ca} \mu \nabla \phi \quad (1-23)$$

where $\theta = \eta/\eta_c$ is the normalized viscosity, $\mu = \phi^3 - \phi - \nabla^2 \phi$ is the dimensionless chemical potential. The dimensionless groups used are Renolds number and capillary number given by

$$Re = \frac{\rho U_c \xi}{\eta}, Ca = \frac{\alpha \eta U_c}{\beta^2 \xi} = \frac{2 \eta U_c}{3 \sigma} \quad (1-24)$$

The above paragraph introduces different phase field model with different local free energy density form. It could also be noted that for different applications of phase-field method, they will have different interface energy (also known as gradient energy). Reference [28] gave a detailed history of phase-field method and its application in different research areas. In references [28], different interface energy model are also introduced based on the previous researches of phase-field.

The commonly used interface gradient energy density is [32]

$$f_{gr} = \frac{1}{2} \lambda |\nabla \phi|^2 \quad (1-25)$$

where λ is the mixing energy density coefficient with the dimension of force.

Wheeler *et al.* (1993) suggested the directional dependence of the gradient energy coefficient as [33]

$$\sqrt{\lambda} = a [1 + b(n_x^4 + n_y^4 + n_z^4)] \quad (1-26)$$

where n_x , n_y and n_z are the x , y and z components of a unit vector \mathbf{n} .

There are also many researches in the multi-phase modeling. Ofori-Opoku *et al.* (2010) suggested a ternary system as [34]

$$\frac{\partial n}{\partial t} = M_n \nabla^2 \left\{ n - \eta \frac{n^2}{2} + \chi \frac{n^3}{3} + \omega \Delta F_{mix}^{ter} - C_{eff}^{ter} n \right\} \quad (1-27)$$

$$\frac{\partial c_A}{\partial t} = M_A \nabla^2 \left\{ \omega (n + 1) \frac{\delta \Delta F_{mix}^{ter}}{\delta c_A} - \frac{1}{2} n \frac{\delta C_{eff}^{ter}}{\delta c_A} - \kappa_A \nabla^2 c_A \right\} \quad (1-28)$$

$$\frac{\partial c_B}{\partial t} = M_b \nabla^2 \left\{ \omega(n+1) \frac{\delta \Delta F_{mix}^{ter}}{\delta c_B} - \frac{1}{2} n \frac{\delta c_{eff}^{ter}}{\delta c_B} - \kappa_B \nabla^2 c_B \right\} \quad (1-29)$$

where M_n , M_{cA} and M_{cB} are dimensionless mobility coefficients for density and composition fields.

Benke's model is shown as [35]

$$\dot{\phi}_\alpha = \sum_\beta \mu_{\alpha\beta} \left[\sigma_{\alpha\beta}^* K_{\alpha\beta} + \frac{\pi}{\eta} \sqrt{\phi_\alpha \phi_\beta} (\Delta G_{\alpha\beta}^{ch} + \Delta G_{\alpha\beta}^{me}) \right] \quad (1-30)$$

$$\dot{\vec{c}} = grad \sum_{\alpha=1}^N \phi_\alpha D_\alpha grad \vec{c}_\alpha \text{ and } div \sigma = 0 \quad (1-31)$$

where $\mu_{\alpha\beta}$ is the mobility of the interface, $\sigma_{\alpha\beta}^*$ is the interface stiffness and $K_{\alpha\beta} = \phi_\alpha grad^2 \phi_\beta - \phi_\beta grad^2 \phi_\alpha + \frac{\pi^2}{\eta^2} (\phi_\alpha - \phi_\beta)$ defines the generalized curvature operator of the interface. The chemical driving $\Delta G_{\alpha\beta}^{ch}$ refers to the interaction between the interface ϕ^α and ϕ^β .

Besides, Voyiadjis *et al.* (2013) studied the nonlocal damage model using the phase-field theory [36]. Boettinger *et al.* (2002) presented how the phase-field method could be implemented in solidification modeling [37]. Abu Al-Rub *et al.* (2003) coupled the anisotropic damage with plasticity for ductile materials by using Phase-field method [38]. Aranson *et al.* (2000) developed continuum phase-field model for crack propagation in brittle amorphous solids [39]. Their model could capture almost all important phenomenology of cracking: initiation, propagation, dynamic fracture instability, sound emission, crack branching and fragmentation [39]. Bates *et al.* (2009) proposed a stable, convergent Phase-field model to solve the long-range spatial interaction [40]. Borden *et al.* (2012) introduced phase-field method in the dynamic brittle fracture, which does not require numerical tracking of discontinuities in the displacement field and greatly reduced implementation complexity [41]. Guo *et al.* (2008) developed an elastoplastic phase-field model to simulate the morphology evolution of hydride precipitation in zirconium bulk material [42]. Feng *et al.* (2002) proposed and analyzed the mean curvature flows by using a conserved phase-

field model [43]. Choi *et al.* (2009) showed the unconditionally gradient stable numerical method for solving the conserved phase-field governing equation [44]. Chen *et al.* (1998) employed the semi-implicit Fourier-spectral method to solve the time-dependent phase-field equations (Ginzburg-Landau equation and Cahn-Hilliard equation) [45]. Karma (2001) showed the phase-field formulation for quantitative modeling of alloy solidification [46]. Hunter *et al.* (2008) calculated the gradient plasticity by phase-field model [47]. Feng *et al.* (2006) implemented an adaptive moving meshing method for phase-field equations [48]. Cha *et al.* (2001) studied the isothermal solidification of multicomponent alloys by phase-field method [49]. Cahn *et al.* (1977) presented the phase-field solution for Fe-Al alloy domain growth kinetics [50]. Koslowski *et al.* (2002) developed a phase-field theory of dislocation dynamics, strain hardening and hysteresis in ductile single crystals [51]. Miehe *et al.* (2010) simulated a diffusive crack modeling to overcome the complex crack topologies of traditional fracture mechanics based on the crack phase-field [52]. Nauman *et al.* (1989) studied the phase equilibrium based on the Landau-Ginzburg free energy and phase field model [53]. Moelans *et al.* (2008) introduced various phase-field models and the coupling with other physical phenomena in microstructure evolution [54]. Onuki (1989) analyzed the elastic effects in phase separation of solids based on Ginzburg-Landau Approach [55]. Levitas *et al.* (2002) presented a three-dimensional Landau theory of stress-induced martensitic phase transformation [56]. Sankarasubramanian (2011) conducted microstructural evolution in elastically-stressed solid by phase-field method [57]. Rodney *et al.* (2003) presented a general formalism for incorporating dislocations in Phase-field method [58]. Generally, the Phase field method has a large applicability in material microstructure evolution modeling and thus it is reasonable to implement this convenient in asphalt structure evolution analysis.

Note that the Phase-field method consists of several governing partial differential equations (PDE). Weak formulations for these PDEs are adopted to obtain the numerical solutions. In a weak formulation, an equation is no longer required to hold absolutely [59].

Given a mixture with free energy as $F = \int_{\Omega} [\frac{1}{2}\kappa|\nabla\phi|^2 + f(\phi)] d\Omega$. Note The chemical potential is the variational derivative of the total free energy. Normally, the Euler-Lagrange Theorem is employed to calculate the chemical potential shown as

$$\frac{\delta F}{\delta\phi} = f'(\phi) - \kappa\nabla^2\phi \quad (1-32)$$

The Allen-Cahn equation depicts the non-conserved dynamics in Phase-field.

$$\frac{\partial\phi}{\partial t} = -M \frac{\delta F}{\delta\phi} \quad (1-33)$$

Substitute the form of the chemical potential, we have

$$\frac{\partial\phi}{\partial t} = M(-f'(\phi) + \kappa\nabla^2\phi) \quad (1-34)$$

Multiply the test function $\tilde{\phi}$ on both sides of the equation and integrate over the calculation domain, we have

$$\int_{\Omega} \frac{\partial\phi}{\partial t} \tilde{\phi} d\Omega = \int_{\Omega} M(\kappa\nabla \cdot \nabla\phi\tilde{\phi} - f'(\phi)\tilde{\phi}) d\Omega \quad (1-35)$$

Using Divergence Theorem, we have

$$\int_{\Omega} \frac{\partial\phi}{\partial t} \tilde{\phi} d\Omega = \int_{\partial\Omega} M(\kappa\nabla\phi \cdot \vec{n}\tilde{\phi}) dS - \int_{\Omega} M(\kappa\nabla\phi \cdot \nabla\tilde{\phi}) d\Omega - \int_{\Omega} Mf'(\phi)\tilde{\phi} d\Omega \quad (1-36)$$

The essential boundary condition is $\phi = \alpha$ on $\partial\Omega$ while the natural boundary condition is $\nabla\phi \cdot \vec{n} = \beta$ on $\partial\Omega$. Consider the natural boundary condition $\nabla\phi \cdot \vec{n} = 0$ we further have

$$\int_{\Omega} \frac{\partial\phi}{\partial t} \tilde{\phi} d\Omega + \int_{\Omega} M (\kappa \nabla\phi \cdot \nabla\tilde{\phi}) d\Omega + \int_{\Omega} M f'(\phi) \tilde{\phi} d\Omega = 0 \quad (1-37)$$

And this is the weak of Allen-Cahn dynamics.

The Cahn-Hilliard equation describes the conserved dynamics in Phase-field and known as

$$\frac{\partial\phi}{\partial t} = \nabla \cdot \left(M \nabla \frac{\delta F}{\delta\phi} \right) = \nabla \cdot (M \nabla G) = \nabla \cdot [M \nabla (f'(\phi) - \kappa \nabla^2 \phi)] \quad (1-38)$$

where G is the chemical potential.

Multiply the test function $\tilde{\phi}$ on both sides and integrate over the calculation domain Ω and we have

$$\int_{\Omega} \frac{\partial\phi}{\partial t} \tilde{\phi} d\Omega = \int_{\Omega} \nabla \cdot (M \nabla G) \tilde{\phi} d\Omega \quad (1-39)$$

Using Divergence theorem, we further have

$$\int_{\Omega} \frac{\partial\phi}{\partial t} \tilde{\phi} d\Omega = \int_{\partial\Omega} \tilde{\phi} M \nabla G \cdot \vec{n} dS - \int_{\Omega} M \nabla G \cdot \nabla \tilde{\phi} d\Omega \quad (1-40)$$

Since

$$G = \frac{\delta F}{\delta\phi} = f'(\phi) - \kappa \nabla^2 \phi \quad (1-41)$$

We can get

$$\int_{\Omega} \frac{\partial \phi}{\partial t} \tilde{\phi} d\Omega = \int_{\partial\Omega} \tilde{\phi} M \nabla (f'(\phi) - \kappa \nabla^2 \phi) \cdot \vec{n} dS - \int_{\Omega} M \nabla f'(\phi) \cdot \nabla \tilde{\phi} d\Omega + \int_{\Omega} M \nabla (\kappa \nabla^2 \phi) \cdot \nabla \tilde{\phi} d\Omega \quad (1-42)$$

And we can further derive as

$$\int_{\Omega} \frac{\partial \phi}{\partial t} \tilde{\phi} d\Omega = \int_{\partial\Omega} \tilde{\phi} M \nabla (f'(\phi) - \kappa \nabla^2 \phi) \cdot \vec{n} dS - \int_{\Omega} M \nabla f'(\phi) \cdot \nabla \tilde{\phi} d\Omega + \int_{\partial\Omega} \kappa \nabla^2 \phi M \nabla \tilde{\phi} \cdot \vec{n} dS - \int_{\Omega} \kappa \nabla^2 \phi \nabla \cdot (M \nabla \tilde{\phi}) \quad (1-43)$$

For essential boundary condition, we needs to know $\frac{\partial \phi}{\partial n}$.

The last term in this equation contains $\int \nabla^2 \phi \nabla^2 \tilde{\phi}$, thus the second derivative of $\phi, \tilde{\phi}$ is square integrable. We split the 4th order equation into two 2nd order ones shown as

$$\begin{cases} \frac{\partial \phi}{\partial t} = \nabla \cdot (M \nabla G) & (1-44) \\ G = f'(\phi) - \kappa \nabla^2 \phi & (1-45) \end{cases}$$

Multiply the test function \tilde{u} in both sides of equation (1-44) and integrate over the calculation domain as

$$\int_{\Omega} \frac{\partial \phi}{\partial t} \tilde{u} d\Omega = \int_{\partial\Omega} \tilde{u} M \nabla G \cdot \vec{n} dS - \int_{\Omega} M \nabla G \cdot \nabla \tilde{u} d\Omega \quad (1-46)$$

We rewrite it as

$$\int_{\Omega} \frac{\partial \phi}{\partial t} \tilde{u} d\Omega - \int_{\partial\Omega} \tilde{u} M \nabla G \cdot \vec{n} dS + \int_{\Omega} M \nabla G \cdot \nabla \tilde{u} d\Omega = 0 \quad (1-47)$$

The natural boundary condition $\nabla G \cdot \vec{n} = 0$

Multiply the test function \tilde{v} in both sides of equation (1-45) and integrate over the calculation domain as

$$\int_{\Omega} G \tilde{v} d\Omega = \int_{\Omega} f'(\phi) \tilde{v} d\Omega - \int_{\partial\Omega} \kappa \tilde{v} \nabla \phi \cdot \vec{n} dS + \int_{\Omega} \nabla \kappa \tilde{v} \cdot \nabla \phi d\Omega \quad (1-48)$$

We rewrite it as

$$\int_{\Omega} G \tilde{v} d\Omega - \int_{\Omega} f'(\phi) \tilde{v} d\Omega + \int_{\partial\Omega} \kappa \tilde{v} \nabla \phi \cdot \vec{n} dS - \int_{\Omega} \nabla \kappa \tilde{v} \cdot \nabla \phi d\Omega = 0 \quad (1-49)$$

The boundary condition $\nabla \phi \cdot \vec{n} = \alpha$

Equation (1-47) and equation (1-49) are the weak forms of Cahn-Hilliard dynamics.

REFERENCES

1. Wang, D., Wang, L., Gu, X. and Zhou, G. (2013). "Effect of Basalt Fiber on the Asphalt Binder and Mastic at Low Temperature." *Journal of Materials in Civil Engineering*, 25(3), 355-364.
2. Buttlar, W., Paulino, G. and Song, S. (2006). "Application of Graded Finite Element for Asphalt Pavements." *Journal of Engineering Mechanics*, 132(3), 240-249.
3. Fu, Y., Wang, L., Tumay, M., and Li, Q. (2008). "Quantification and Simulation of Particle Kinematics and Local Strains in Granular Materials Using X-ray Tomography Imaging and Discrete Element Method". *Journal of Engineering Mechanics*, 134(2), 143-154.

4. Bhasin, A., Bommavaram, R., Greenfield, M. and Little, D. (2011). "Use of Molecular Dynamic to Investigate Self-Healing Mechanisms in Asphalt Binders." *Journal of Materials in Civil Engineering*, 23(4), 485-492.
5. Cahn, J., and Hilliard, J. (1958). "Free Energy of a Nonuniform System. I. Interfacial Free Energy." *Journal of Chemical Physics*, 28, 258-267.
6. Karma, A., Kessler, D. and Levine, H. (2001). "Phase-field model of mode III dynamic fracture." *Physical Review Letter*, Vol. 87, 045501.
7. Jacqmin, D. (1999). "Calculation of two-phase Navier-Stokes flow using phase-field modeling." *Journal of Computational Physics*, 155, 96-127.
8. Wise, S., Lowengrub J., Frieboes, H. and Cristini, V. (2008) "Three-dimensional multispecies nonlinear tumor growth - I. Model and numerical method." *Journal of Theoretical Biology*, 255, 257-274.
9. Greiner, W., Neise, L., Stocker, H. (1995) Thermodynamics and statistical mechanics. Springer- Verlag.
10. V.L. Ginzburg and L.D. Landau, Zh. Eksp. Teor. Fiz. 20, 1064 (1950). English translation in: L. D. Landau, Collected papers (Oxford: Pergamon Press, 1965) pp. 546.
11. Chen, L. "Phase-field models for Microstructure evolution." (2002). *Annu. Rev. Mater. Res.*, 32:113-40.
12. Allen, S. and Cahn, J. (1972) "Ground State Structures in Ordered Binary Alloys with Second Neighbor Interactions." *Acta Met.*, 20, 423.
13. Strang, G. and Fix, G. (1973). An Analysis of The Finite Element Method. Prentice Hall. ISBN 0-13-032946-0.

14. Morton, K. and Mayers, D. (2005). Numerical Solution of Partial Differential Equations, An Introduction. Cambridge University Press, 2005.
15. Marcusson, Naturlichen J D., “und Kunstlichen Asphalte”, Wilhels Englemann Co., Leipzig, 1931.
16. Villain-Guillot, S. (2004). “Coalescence in the 1D Cahn-Hilliard model.” *Journal of Physics A: Mathematical and General*, 37(27): 6929-6941.
17. Yue, P., Feng, J., Liu, C. and Shen, J. (2004). “A diffuse-interface method for simulating two-phase flows of complex fluids.” *Journal of Fluid Mechanics*, 515: 293-317.
18. Anderson, D.M., McFadden, G.B. and Wheeler, A.A. (1998). “Diffuse-interface methods in fluid mechanics.” *Annu. Rev. Fluid Mech.*, 30: 139–165.
19. Kim, J. and Lowengrub, J. (2005). “Phase field modeling and simulation of three-phase flows.” *Int. Free Bound.*, 7:435–466.
20. Kim, J. (2007). “Phase field computations for ternary fluid flows.” *Comput. Methods Appl. Mech. Eng.*, 196: 45–48.
21. Boyer, F., Lapuerta, C., Minjeaud, S., Piar, B. and Quintard, M. (2010). “Cahn-Hilliard/Navier-Stokes Model for the simulation of Three-Phase Flows.” *Transp Porous Med*, 82: 463-483.
22. Wang, Y., Jin, Y.M., Cuitino, A.M., Khachatryan, A.G. (2001). “Phase field microelasticity theory and modeling of multiple dislocation dynamics.” *Applied Physics Letters*, 78(16): 2324-2326.
23. Caginalp, G., Chen, X. (1992). “Phase field equations in the singular limit of sharp interface problems.” In *On the Evolution of Phase Boundaries*, ed. ME Gurtin, GB Mcfadden, 43:1-27. New York: Springer-Verlag.

24. Nambu, S., Sagala, D. (1994). "Domain formation and elastic long-range interaction in ferroelectric perovskites." *Physical Review B*, 50:5838-5847.
25. Chen, L, Yang, W. (2004). "Computer simulation of the domain dynamics of a quenched system with a large number of nonconserved order parameters: The grain-growth kinetics." *Physical Review B*, 50(21): 15752.
26. Braun, R., Cahn, J., McFadden, G., Rushmeier, H. and Wheeler, A. (1998). "Theory of anisotropic growth rates in the ordering of an f.c.c. alloy." *Acta Materialia*, 46(1): 1-12.
27. Wang, Y., Banerjee, D., Su, C. and Khachaturyan. (1998). "Field kinetic model and computer simulation of precipitation of L1₂ ordered intermetallics from f.c.c solid solution." *Acta Materialia*, 46(9): 2983-3001.
28. Chen, L. (2002). "Phase-field models for microstructure evolution." *Annu. Rev. Mater. Res.*, 32: 113-40.
29. Wang, Y. and Khachaturyan, A. (1997). "Three-dimensional field model and computer modeling of martensitic transformations." *Acta Materialia*, 45:759-773.
30. Takada, N., Misawa, M. and Tomiyama, A. (2006). "A phase-field method for interface tracking simulation of two-phase flows." *Mathematics and Computers in Simulation*, 72: 220-226.
31. Badalassi, V., Ceniceros, H. and Banerjee. (2003). "Computation of multiphase systems with phase field models." *Journal of Computational Physics*, 190(2): 371-397.
32. Yue, P., Zhou, C., Feng, J., Ollivier-Gooch, C. and Hu, H. (2006). "Phase-field simulations of interfacial dynamics in viscoelastic fluids using finite elements with adaptive meshing." *Journal of Computational Physics*, 219:47-67.

33. Wheeler, A., Murray, B. and Schaefer, R. (1993). "Computation of dendrites using a phase field model." *Physica. D.*, 66:243-262.
34. Ofori-Opoku, N., Fallah, V., Greenwood, M., Esmaeili, S. and Provatas, N. (2013). "A Multi-Component Phase Field Model for Structural Transformations in Metal Alloys." *Physical Review B*, 87: 134105.
35. Benke, S. (2008). "A multi-phase-field model including inelastic deformation for solid state transformations." *Proc. Appl. Math. Mech.*, 8:10407-10408.
36. Voyiadjis, G. and Mozaffari, N. (2013). "Nonlocal damage model using the phase field method: Theory and applications." *International Journal of Solids and Structures*, 50: 3136-3151.
37. Boettinger, W., Warren, J., Beckermann, C. and Karma, A. (2002). "Phase-field simulation of solidification 1." *Annual Review of Materials Research*, 32:163–194.
38. Abu Al-Rub, R., and Voyiadjis, G. (2003). "On the coupling of anisotropic damage and plasticity models for ductile materials." *International Journal of Solids and Structures*, 40:2611-2643.
39. Aranson, I., Kalatsky, V., Vinokur, V. (2000). "Continuum field description of crack propagation." *Physical Review Letters*, 85:118–121.
40. Bates, P., Brown, S. and Han, J. (2009). "Numerical analysis for a nonlocal Allen–Cahn equation." *Numerical Analysis and Modeling*, 6:33–49.
41. Borden, M., Verhoosel, C., Scott, M., Hughes, T. and Landis, C. (2012). "A phase-field description of dynamic brittle fracture." *Computer Methods in Applied Mechanics and Engineering*, 217-220, pp. 77-95.

42. Guo, X., Shi, S., Zhang, Q. and Ma, X. (2008). “An elastoplastic phase-field model for the evolution of hydride precipitation in zirconium. Part I: Smooth specimen.” *Journal of Nuclear Materials*, 378(1): 110-119.
43. Feng, X. and Prohl, A. (2003). “Numerical analysis of the Allen–Cahn equation and approximation for mean curvature flows.” *Numerische Mathematik*, 94:33–65.
44. Choi, J., Lee, H., Jeong, D. and Kim, J. (2009). “An unconditionally gradient stable numerical method for solving the Allen–Cahn equation.” *Physica A: Statistical Mechanics and its Applications*, 388: 1791–1803.
45. Chen, L. and Shen, J. (1998). “Applications of semi-implicit Fourier-spectral method to phase field equations.” *Computer Physics Communications*, 108: 147–158.
46. Karma, A. (2001). “Phase-field formulation for quantitative modeling of alloy solidification.” *Physical Review Letters*, 87:115701.
47. Hunter, A. and Koslowski, M. (2008). “Direct calculations of material parameters for gradient plasticity.” *Journal of the Mechanics and Physics of Solids*, 56: 3181– 3190.
48. Feng, W., Yu, P., Hu, S., Liu, Z., Du, Q. and Chen, L. (2006). “Spectral implementation of an adaptive moving mesh method for phase-field equations.” *Journal of Computational Physics*, 220: 498–510.
49. Cha, P., Yeon, D. and Yoon, J.K. (2001). “A phase field model for isothermal solidification of multicomponent alloys.” *Acta Materialia*, 49:3295–3307.
50. Cahn, J., Allen, S. (1977). “A microscopic theory for domain wall motion and its experimental verification in Fe–Al alloy domain growth kinetics.” *Le Journal de Physique Colloques*, 38: C7-51-C7-54.

51. Koslowski, M., Cuitino, A. and Ortiz, M. "A phase-field theory of dislocation dynamics, strain hardening and hysteresis in ductile single crystals." *Journal of the Mechanics and Physics of Solids*, 50: 2597-2635.
52. Miehe, C., Welschinger, F. and Hofacker, M. (2010). "Thermodynamically consistent phase-field models of fracture: variational principles and multi-field FE implementations." *International Journal for Numerical Methods in Engineering*, 83: 1273–1311.
53. Nauman, E., Balsara, N. (1989). "Phase equilibria and the Landau–Ginzburg functional." *Fluid Phase Equilibria*, 45:229–250
54. Moelans, N., Blanpain, B. and Wollants, P. (2008). "An introduction to phase-field modeling of microstructure evolution." *Calphad*, 32:268–294.
55. Onuki, A. (1989). "Ginzburg–Landau approach to elastic effects in the phase separation of solids." *Journal of the Physical Society of Japan*, 58:3065–3068.
56. Levitas, V. and Preston, D. (2002). "Three-dimensional Landau theory for multivariant stress-induced martensitic phase transformations. I: Austenite to Mmartensite." *Physical Review B*, 66:134206.
57. Sankarasubramanian, R. (2011). "Microstructural evolution in elastically-stressed solids: a phase-field simulation." *Defence Science Journal*, 61: 383–393.
58. Rodney, D., Le Bouar, Y. and Finel, A. (2003). "Phase field methods and dislocations." *Acta Materialia*, 51:17–30.
59. Lax, P.; Milgram, Arthur N. (1954). "Parabolic equations". *Contributions to the theory of partial differential equations*. Annals of Mathematics Studies, no. 33. Princeton, N. J.: Princeton University Press. pp. 167–190.

Chapter 2. Asphalt mechanical property based on asphalt chemistry by Phase-field modeling¹

2.1 Introduction

Asphalt is the most important pavement material and has been widely used by civil engineers all through the world. Asphalt, as the petroleum product, consists of asphaltene, wax, aromatics, resin and many other chemical components [1, 2]. It is reasonable to believe that these chemical components will have negative effects in the asphalt physical properties and mechanical behaviors that may lead to cracking failure.

A major failure is the cracking caused by thermal loading. In the US, the performance specification of asphalt binder has been developed in the Strategic Highway Research Program (SHRP) [3]. Griffith's cracking theory [4] is a powerful tool which has been widely used in the analysis of cracking. However, there still lacks a way to analyze the mechanical behavior of asphalt binder based on asphalt chemistry from a microscopic perspective. In this chapter, combined with the Phase kinetics theory, we analyze how the asphalt components will affect the asphalt performance under given thermal conditions.

¹ Part of this chapter is submitted to *The Baltic Journal of Road and Bridge Engineering* for review.

Wang, L., Hou, Y., Yue, P and Pauli, T. (2014). "A phase field approach for computing residual thermal stress in asphalt binder." *The Baltic Journal of Road and Bridge Engineering*. (Submitted 1/21/2014)

2.2 Marcusson model based on asphalt chemistry

Asphalt is a product of the petroleum industry and its compositions are very complex. It is primarily a mixture of highly condensed hydrocarbons which are very difficult to separate from each other. The oldest and the most common determination criterion of asphalt compositions was suggested by Marcusson (1931) in 1931 [5]. In this method, different compositions are separated based on the solubility in different solvents. Later improvements were made by Hubbard *et al.* (1948) [6], Koots *et al.* (1975) [7], Lian *et al.* (1994) [2]. Based on the results of these researchers, some national standards, such as the Standard test methods of bitumen and bituminous mixture for highway engineering in China (2000) [8], have emerged for the determination of asphalt chemistry.

According to the standard Marcusson model, there are generally two ways to distinguish the asphalt compositions: one is the three-composition method and the other is the four-composition method. In our analysis, the former is employed, which is shown in the Table 3-1. Dunstan *et al.* (1931) proposed an assumption that asphalt has a colloidal structure in which the asphaltene particles are wrapped by resin and dispersed in the oil phase [9]. If we further consider the fact that the molar fraction of asphaltene is smaller than the other two, we can simplify the Marcusson model to two compositions: resin and oil. We believe that these two components dominate the phase separation and mechanical properties in the asphalt binder. The evolution of microstructures in the resulted binary mixture can be explored by the phase-field method.

Table 2-1 The three - composition method of Asphalt based on Marcusson method

Compositions	Features	Average molecule weight	C/H ratio	Content %	Relative Density (with water)
Oil	Transparent liquid	200~700	0.5~0.7	45~60	0.910~0.925
Resin	Brown half-solid	800~3000	0.7~0.8	15~30	Lager than 1
Asphaltene	Solid particle	1000~5000	0.8~1.0	5~30	1.100~1.500.

2.3 Phase field model

The phase field model uses an phase field parameter ϕ to describe the status of the coarse-grained microstructures. ϕ assumes -1 in the oil and +1 in the resin. The interface between the two components, i.e., two phases, is represented by the $\phi = 0$ level set. For a mixture that occupies a computation domain Ω , the free energy can be written in the Landau-Ginzburg form

$$F(\phi) = \int_{\Omega} (f_{gr} + f_{loc})dV, \quad (2-1)$$

where

$$f_{gr} = \frac{1}{2}\kappa|\nabla\phi|^2 \quad (2-2)$$

is the gradient energy density, κ controls the interfacial thickness.

$$f_{loc} = (1 - \phi^2)^2 \quad (2-3)$$

is the local free energy density. Here, κ is related to the interfacial tension and can be determined by experiments. f_{loc} , also known as the double-well potential (Figure 2-1), is minimized at $\phi =$

-1 and $\phi = 1$, i.e., completely separated components in asphalt. It should be noted that the minimization of the gradient energy tends to generate a mixture with uniform ϕ . The competition between the gradient and local energies result into a diffuse interface that allows finite miscibility between the two phases.

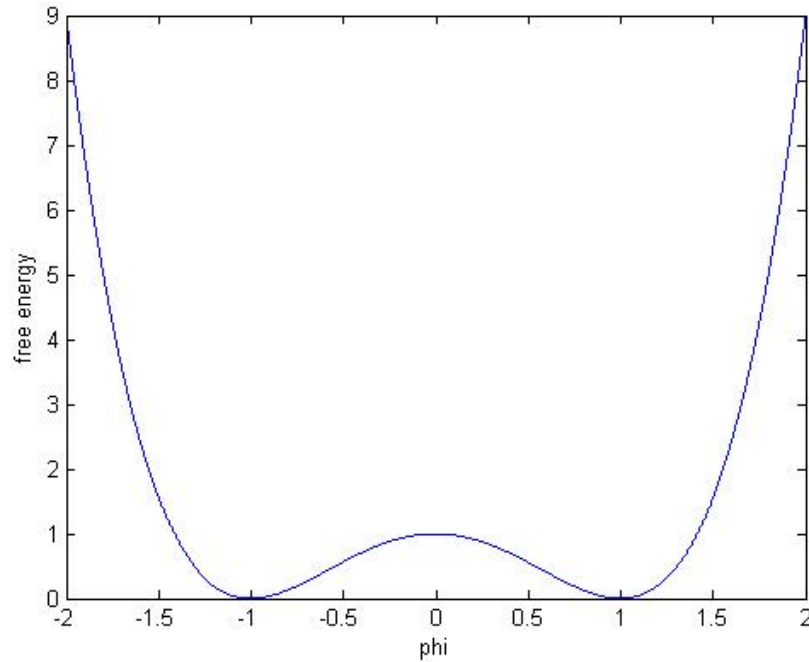


Figure 2-1 A double-well potential

For the stress field, we consider the static equilibrium

$$\nabla \cdot \sigma = 0. \tag{2-4}$$

Considering the asphalt binder at a low temperature as a linear elastic material and according to Hook's law, the stress can be expressed as

$$\sigma = E(\phi):(\varepsilon - \varepsilon_0), \tag{2-5}$$

where $E(\phi)$ is the phase-dependent elastic modulus.

The strain tensor ε is obtained by

$$\varepsilon = \frac{1}{2}(\nabla \mathbf{u} + (\nabla \mathbf{u})^T) \quad (2-6)$$

where \mathbf{u} is the displacement field. The strain tensor ε_0 , at which the stress is zero, is given by

$$\varepsilon_0 = (\alpha \Delta T)I, \quad (2-7)$$

where, α is the thermal expansion coefficient, ΔT is the temperature change, and I is the identify tensor.

The elastic energy density can be formulated as

$$f_{el} = \frac{1}{2}(\varepsilon - \varepsilon_0):[E(\phi):(\varepsilon - \varepsilon_0)]. \quad (2-8)$$

Based on Euler–Lagrange equation, the chemical potential of the system can be calculated as the variational derivative of the free energy

$$G = \frac{\delta F}{\delta \phi} = \frac{1}{2}(\varepsilon - \varepsilon_0):[E'(\phi):(\varepsilon - \varepsilon_0)] - 4\phi(1 - \phi^2) - \kappa \Delta \phi. \quad (2-9)$$

For simplicity we neglect the contribution of f_{el} to the chemical potential and only consider the last two terms on the right hand side of the equation above. Since this process is mass conserved, the Cahn-Hillard equation

$$\frac{\partial \phi}{\partial t} = \nabla \cdot (M \nabla G) = \nabla \cdot \left(M \nabla \frac{\delta F}{\delta \phi} \right) = \nabla \cdot [M \nabla (-4\phi(1 - \phi^2) - \kappa \Delta \phi)] \quad (2-10)$$

is employed to describe the evolution process, where M is the mobility parameter which controls the rate of the diffusion process.

After obtaining both physics model, the coupling of the two physics should be taken into consideration. In our analysis, the main purpose is to find the effect of phase separation on the residual thermal stress. Therefore, we only consider the one-way coupling, i.e., the phase

separation has a significant effect on the thermal stress but not vice versa. The coupling is mainly reflected on the physical properties of asphalt, such as the elastic modulus C , Poisson's ratio ν , etc. For simplicity, only the elastic modulus is considered as phase-dependent. The other physical parameters are considered uniform in the mixture. Following Wise *et al.* [10], we formulate the elastic modulus as

$$C_{ijkl}(\phi) = C_{ijkl}^0 + h(\phi)(C_{ijkl}^1 - C_{ijkl}^0), \quad (2-11)$$

where C_{ijkl}^0 and C_{ijkl}^1 are the elastic modulus at $\phi = -1$ and $+1$, respectively.

$$h(\phi) = -\frac{1}{4}\phi^3 + \frac{3}{4}\phi + \frac{1}{2} \quad (2-12)$$

is the fitting function that satisfies $h(-1) = 0$, $h(1) = 1$, $h'(-1) = h'(1) = 0$. It should be noted that the elastic modulus in oil is nearly zero and the Poisson's ratio is undefined. However, to avoid numerical singularity in elasticity calculations, we assume that $C^0 = 0.01C^1$ and $\nu = 0.3$ throughout the computational domain.

The von Mises yield criterion [11] is frequently used to judge whether an elastic material yields under a given stress field. Therefore,

Generally, we have the Von mises stress expressed as

$$\sigma_v = \sqrt{\frac{(\sigma_{xx}-\sigma_{yy})^2+(\sigma_{yy}-\sigma_{zz})^2+(\sigma_{xx}-\sigma_{zz})^2+6(\sigma_{xy}^2+\sigma_{yz}^2+\sigma_{zx}^2)}{2}} \quad (2-13)$$

where σ_{ij} is the stress tensor component calculated in the thermal loading process.

2.4 Numerical simulations and results

2.4.1 Initialization of model

An Eulerian mesh is used for the phase-field computation as shown in Figure 2- 2. Generally 7-10 mesh points across the interface are required to sufficiently resolve the diffuse interface. However, if we use uniform mesh with cell size determined by the interfacial thickness, then the computational mesh will be prohibitively large. To resolve this problem, we use an adaptive mesh which only refines on the interface.

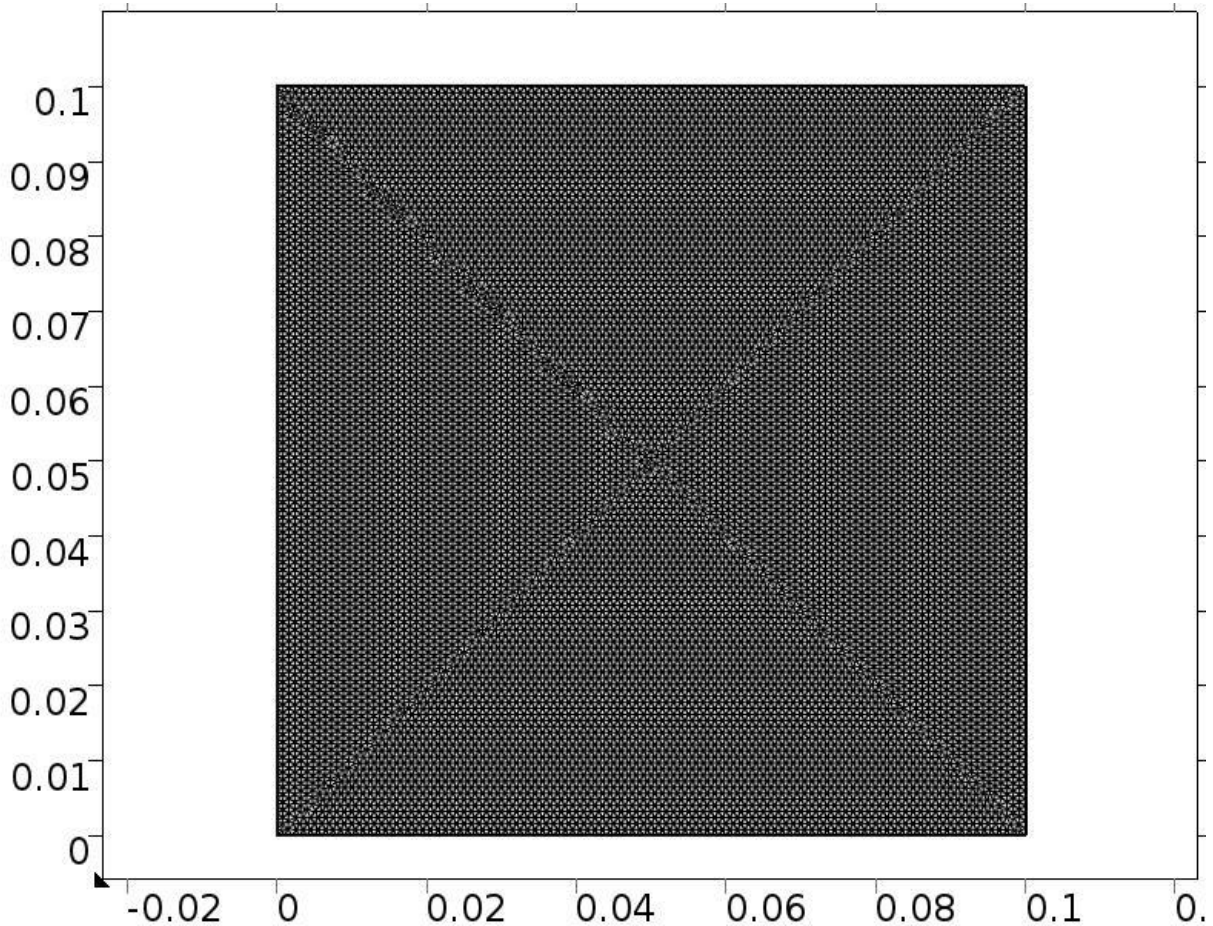


Figure 2-2 The unstructured triangular mesh generated by COMSOL

The commonly used physical properties of asphalt are: density $\rho = 1010 \text{ kg/m}^3$, Poisson's ratio $\nu = 0.3$, Young's modulus $E=5 \text{ MPa}$, thermal expansion coefficient $\alpha = 6 \times 10^{-4}$, thermal conductivity is $0.75 \text{ W/m} \cdot \text{K}$, and heat capacity is $120 \text{ J/K} \cdot \text{kg}$. Note that the last two parameters are not used in our current computations.

According to Table 2-1, a resin-to-oil ratio of 1:2 is elected for our calculations. The initial value of order parameter is set such that $\frac{\phi+1}{2} = \frac{1}{3}$, which gives $\phi = -0.33$ uniformly in the computational domain. The double-well potential $f_{loc}(\phi)$ has two inflection points at ± 0.5774 , between which the homogeneous mixture is unstable and the two phases separate via the spinodal decomposition. The current mixture composition just lies in this spinodal region. To initiate the instability, we perturb the uniform ϕ by a random distribution with a maximum magnitude of 0.1.

2.4.2 Coupled process of a diffuse interface model

We consider a fast cooling from $T=333.15 \text{ K}$ to 273.15 K . The high mobility parameter is selected as 2.5 s/kg so that the evolution process will be fast.

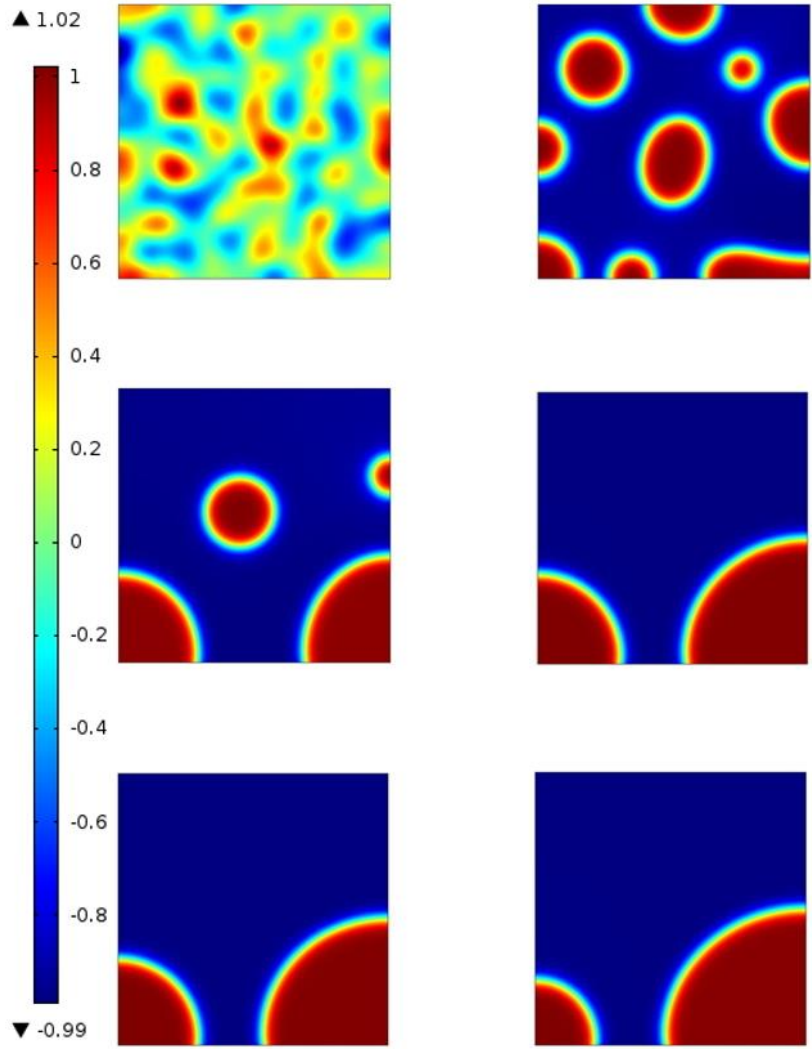


Figure 2-3 Phase separation at $t= 0, 0.05s, 0.5s, 2s, 2.2s$ and $t =3 s$

A typical phase separation process is shown in Figure 2-3. The dark phase is oil while the white one is resin. The interfaces between the two phases tend to assume a planar or spherical shape to minimize surface energy. Figure 2-4 shows the phase field variable distribution on bottom boundary at $t= 0.5s$. We can easily see the diffuse interface between the two phases represented by 1 and -1.

Figure 2-5 shows the distribution of von Mises stress during the phase separation process. Obviously, σ_v has a large gradient on the interface between resin and oil, due to the disparity of elastic modulus. The unit is Pa.

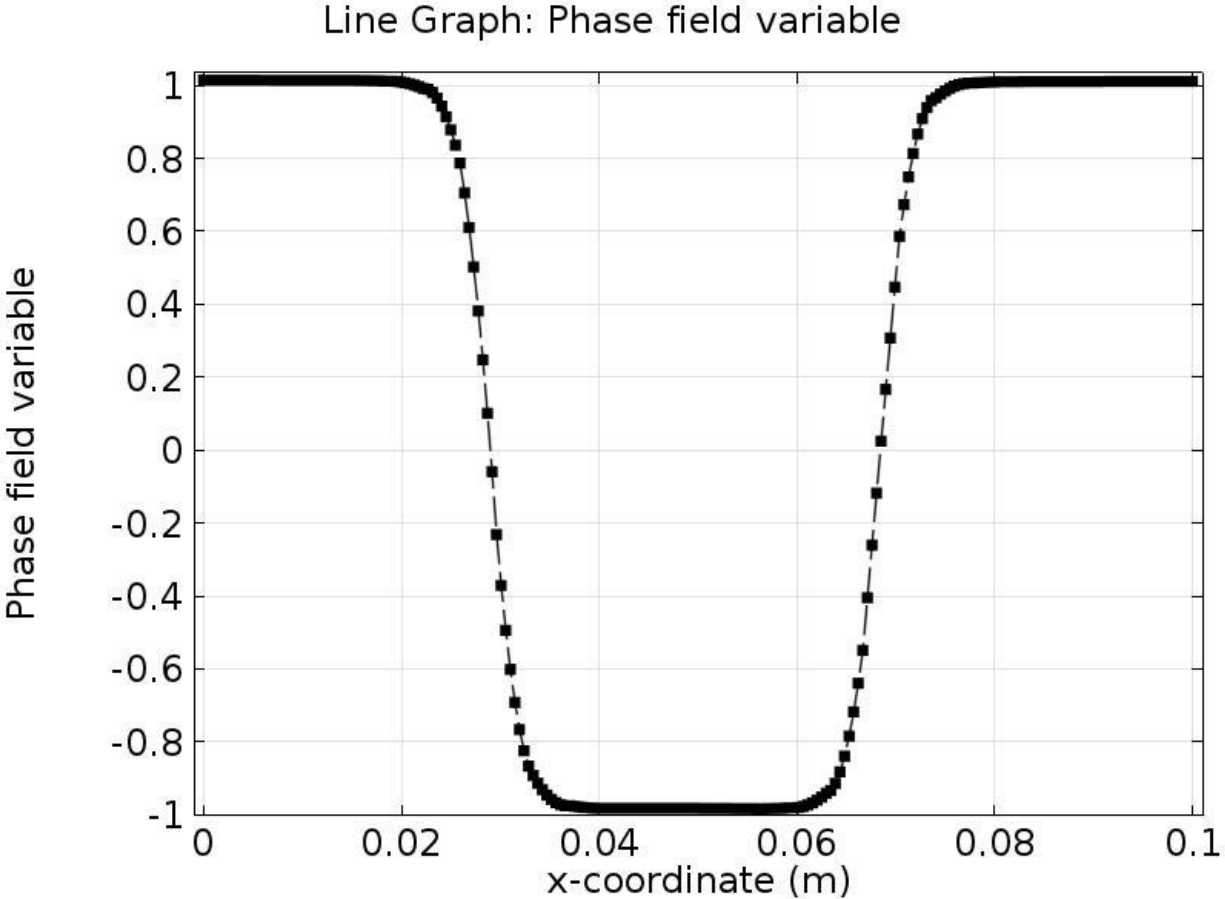


Figure 2-4 Phase field variable distribution at the bottom boundary at t=0.5s

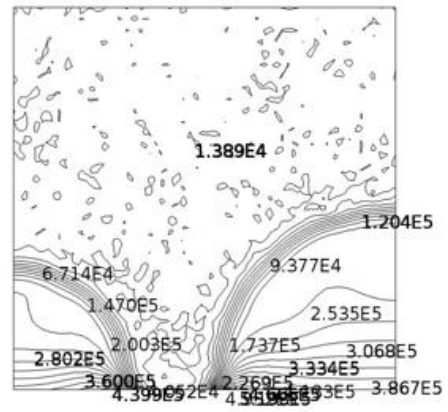
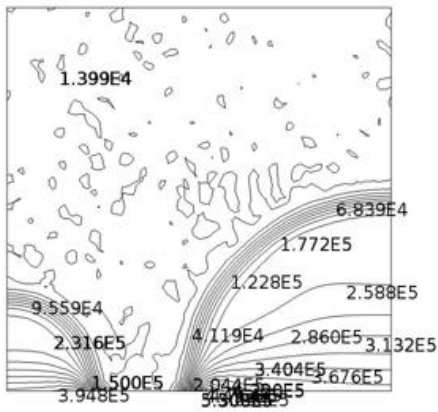
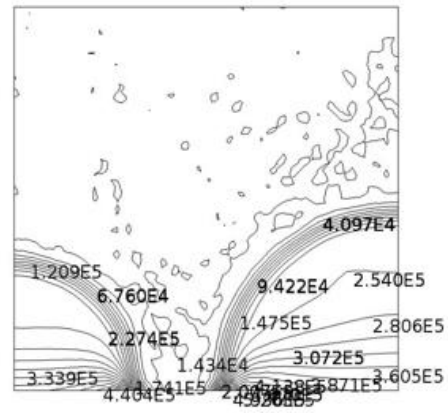
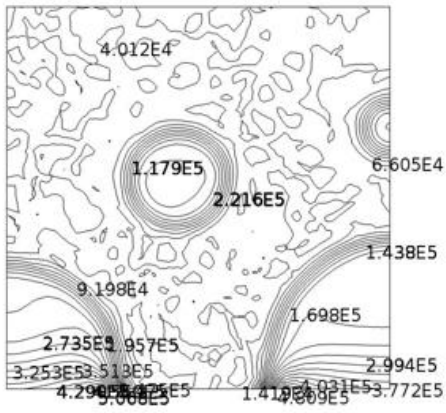
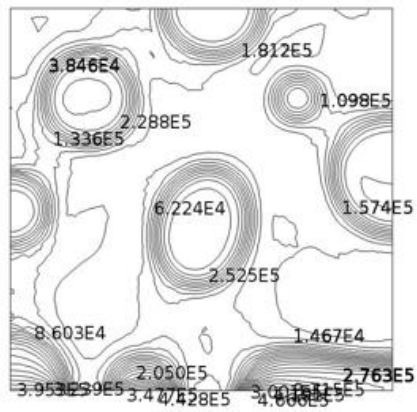
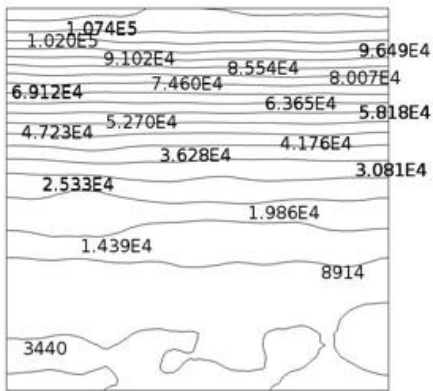


Figure 2-5 Contour plot of Von mises stress at $t= 0, 0.05s, 0.5s, 2s, 2.2s$ and $3s$

Von mises stress distributes along the interface between resin and oil. Note that there exists a high Von mises stress zone at the interface. It is easy to conclude that the diffuse interface has lowered the stress concentration than the sharp interface. The reason why there exists a high stress gradient is because of our 2D assumptions: we assume a ‘plane-strain’ situation and thus in the z direction there will exist a high stress zone, which is caused by phase separation as show in Figure 2-6.

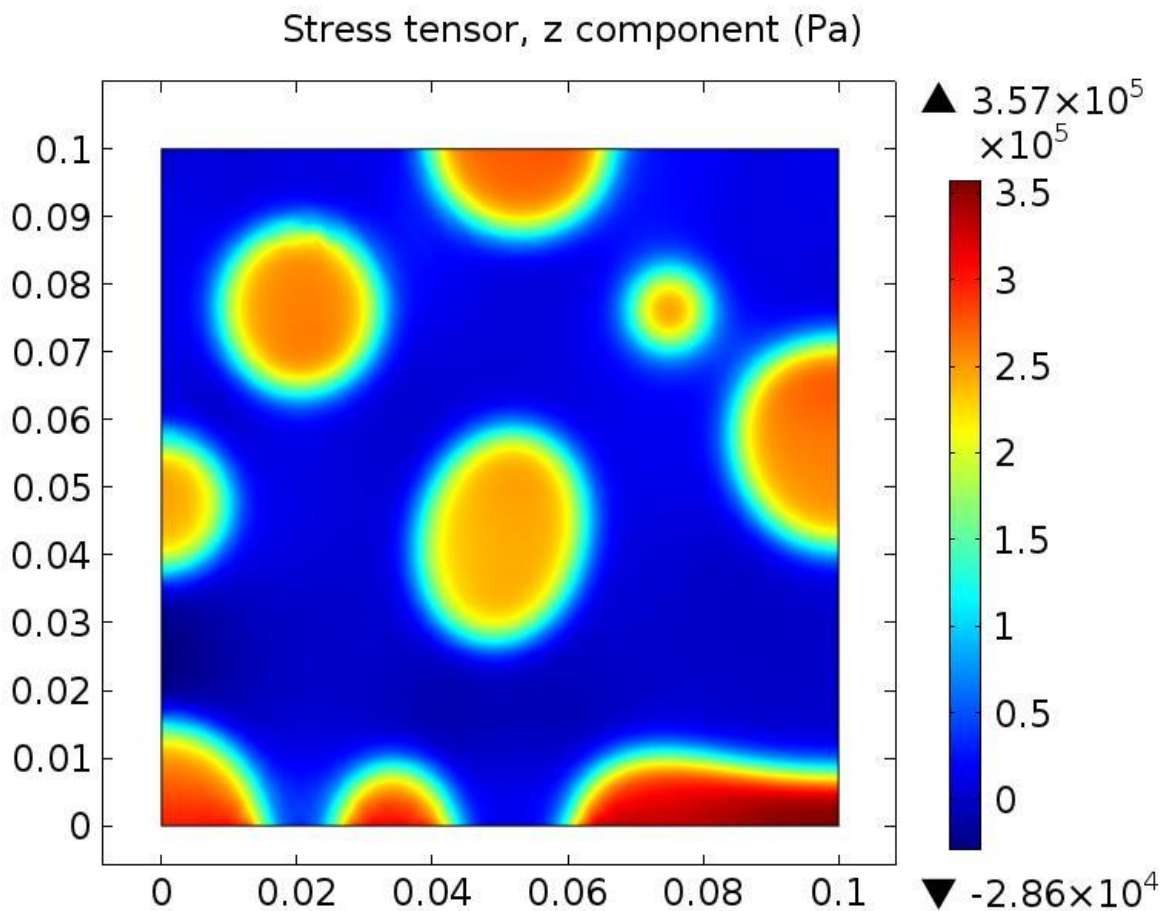


Figure 2-6 z component of stress tensor at $t=0.05s$

Interestingly, Uehara (2011) also discovered that a high equivalent stress distribution occurs at the interface [12]. Almost the same conclusions in different physical process demonstrate that high stress gradient zone across interface is reasonable.

The above analysis demonstrates that the phase field variable has a strong effect on the stress distribution. Since the bottom boundary shows the stress concentration in most of the figures, it is picked up to study the relationship of the two. Figure 2-7 (a), (b) give the xx component and yy component of stress tensor of the bottom boundary at $t=0.5s$, respectively. Compare with the phase separation process at the same time instant in Figure 2-3, it is not strange that the middle part of the Figure 2-7 (a) shows very low stress since this region represents the oil. A sharp contrast is that the two side of the plot show a high value since resin can resist a relatively high stress and the stable stress distribution of the two sides demonstrates the complete separation of resin and oil. It is expected that the boundary condition contributes to the occurrence of high stress zone, but a variance along the boundary gives the strong support of the phase separation effect. Besides, due to the existence of the diffuse interface, stress gradually changes across the interface. Figure 2-7 (b) reveals that the stress σ_{yy} increases greatly from the oil phase (middle part) to a certain region of the interface (either left or right side). Then it suddenly decreases to zero and changes the sign after crossing the interface and finally reaches a stable negative value in the resin phase. A possible reason for the stress distribution is that the resin phase is compressive in the y direction. The oil phase has almost no stress tensor and the interface is the transition zone from a tensile state to a compressive state. Note that the discontinuity in the σ_{yy} curve is due to the limitation of computational ability.

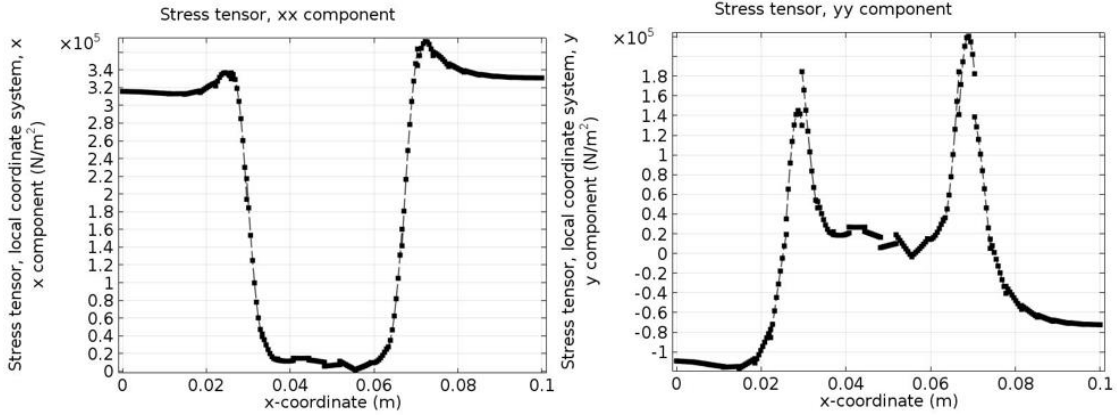


Figure 2-7 (a) xx component (b) yy component of stress tensor of bottom boundary at $t=0.5s$

Figure 2-8 shows the shear stress tensor σ_{xy} at the given time instant $t = 0.5 s$. Different signs of the two sides of the plot indicate that shear stresses have different directions. They reach the peak value near the interfaces and in the resin phase shear stress decreases to zero since two shear stresses induced by the two sides are ‘neutralized’.

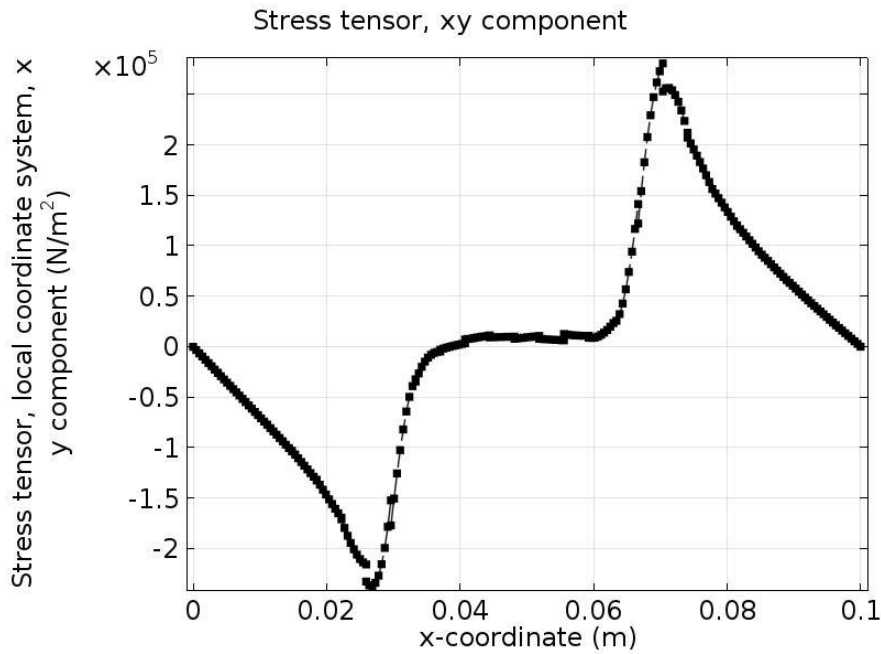


Figure 2-8 xy component of stress tensor of bottom boundary at $t=0.5s$

If we combine σ_{xx} and σ_{yy} together to get the average stress distribution, we get a result shown in Figure 2-9 perfect agreeing with what Hu *et al.* (2002) obtained in the PFM modeling of composition evolution in the presence of structural defects [13]. Calculation results indicate that the peak value of stress occurs at the interface. The only difference is that we have two peak values while the other has only one peak value. This is because we have two interfaces in the bottom boundary while Hu *et al.* (2002) consider the system has only one interface [13].

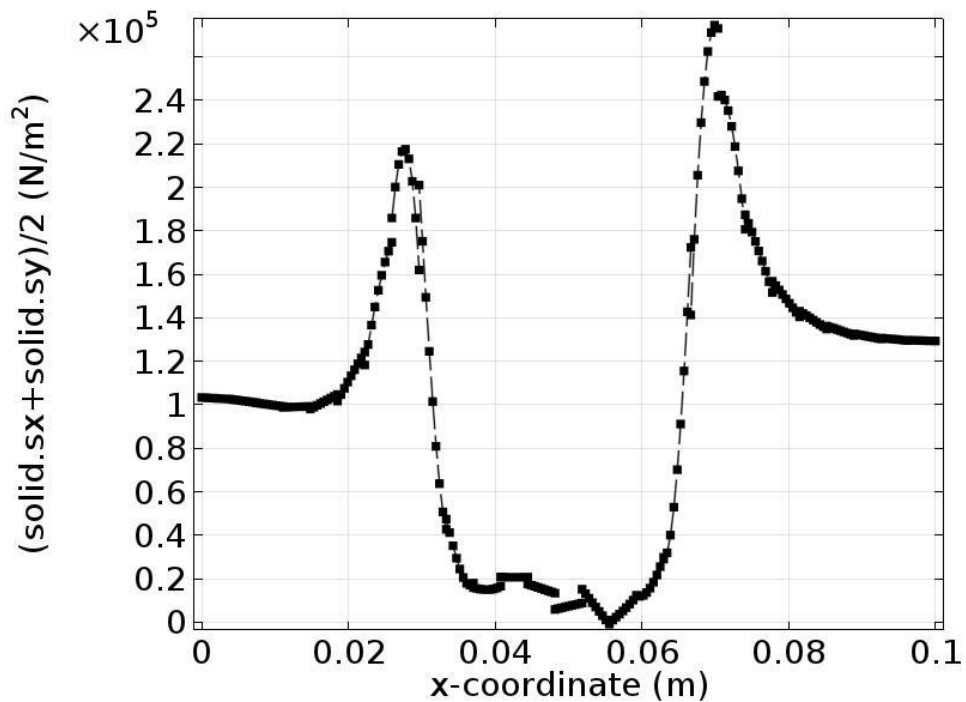


Figure 2-9 Average stress distribution

2.5 Conclusions and Challenge

In this chapter, based on the Phase Field Method, a new approach to calculate the residual stress of asphalt binder under a given thermal loading process is presented. This method is given by using the simplified Marcusson model of asphalt chemistry. Asphalt is considered to have two

main components resin and oil that will affect the physical properties. By doing a one-way coupling, the effect of the phase separation process on the residual thermal stress is studied.

Generally, the following conclusions can be draw from our numerical simulation results:

- 1) An overall view of the thermal loading process demonstrates that phase separation does have an effect of significance on the residual stress. Due to the phase separation, the stress distribution becomes non-uniform and especially, stresses in some regions of the system show an increase while stresses in some other regions show a large decrease. The main reason why it behaves so is that the elastic modulus is not uniform after phase separation;
- 2) High stress zone occurs at the interface between the resin phase and the oil phase. It appears and moves with the interface. Our calculation results has a perfect agreement with the previous research results;

REFERENCES

- [1] Koots, J. and Seight, J. (1975) "Relation of petroleum resins to asphaltenes." *Fuel*, 54, 179-184.
- [2] Lian H., Lin J. and Yen F. (1994) "Peptization studies of asphaltene and solubility parameter spectra", *Fuel*, 73, 423-428.
- [3] Anderson, D., Christensen D., Bahia H., Sharma M., Antle C. and Button J. (1994) "Binder Characterization and Evaluation", Strategic Highway Research Program (SHRP) A-369, National Research Council, Washington, D.C.

- [4] Griffith, A. (1921) "The phenomena of rupture and flow in solids", *Philosophical Transactions of the Royal Society of London, Seria A*, 221, 163-197.
- [5] Marcusson, Naturlichen J D., "und Kunstlichen Asphalte", Wilhels Englemann Co., Leipzig, 1931.
- [6] Hubbard R. and Stanfield K. (1948) "Determination of asphaltenes, oils and resins in asphalt." *Analytical Chemistry*, 20(5).
- [7] Koots J. and Seight J. (1975) "Relation of petroleum resins to asphaltenes", *Fuel*, 54, 179-184.
- [8] Standard test methods of bitumen and bitumous mixtures for Highway Engineering (JTJ 052-2000), Ministry of Transport of the People's Republic of China, 2000.
- [9] Dunstan A., Morrell J. and Egloff G. and Gurwitsch L. "Collidal Chemistry of Petroleum", The Chemical Catalog Co., Inc., New York, 1931.
- [10] Wise S., Lowengrub J., Kim J. and Johnson W. (2004) "Efficient phase-field simulation of quantum dot formation in a strained heteroepitaxial film", *Superlattices and Microstructures*, 36, 293-304.
- [11] Kazimi, S. (1982). Solid Mechanics. Tata McGraw-Hill. ISBN 0-07-451715-5.
- [12] Uehara, T. (2011) "Computer simulation of Microscopic Stress Distribution in Complex Microstructure Using a Phase Field Model", *Journal of Shanghai Jiaotong University (Science)*, 16, 291-295.

[13] Hu S. and Chen L. (2002). "Diffuse-interface modeling of composition evolution in the presence of structural defects." *Computational Material Science*, 23, 270-282.

Chapter 3. Fracture failure of asphalt binder by PFM¹

In this chapter, the asphalt binder cracking analysis based on Phase Field Method is proposed including Mode I, Mode II, mixed mode cracking and crack interaction.

3.1 Introduction and literature review

One of the most serious problems that may lead to pavement failure in winter is cracking in asphalt binder, which may be caused by traffic overloading, thermal loading, and material internal structure changes due to the lower temperature. The cracking dynamics of asphalt binder and asphalt mixture has always been a challenging issue for pavement engineers [1,2]. Generally,

¹ Part of this chapter is published as journal papers or under review.

Hou, Y., Yue, P., Xin, Q., Pauli, T, Sun, W. and Wang, L. (2014) “Fracture Failure of Asphalt Binder in Mixed Mode (Mode I & Mode II) by Using Phase Field Model.” *Road Materials and Pavement Design*, 15(1): 167-181. DOI: 10.1080/14680629.2013.866155.

Hou, Y., Wang, L., Yue, P., Pauli, T and Sun, W. (2013). “Cracking Failure (Mode I) in Asphalt Binder by using a non-conserved Phase Field Model.” *Journal of Materials in Civil Engineering*, 10.1061/(ASCE)MT.1943-5533.0000874, in press, proofreading.

Hou, Y., Wang, L., Yue, P., and Pauli, T. (2013). “Mode II Cracking Failure in Asphalt Concrete by Using A Non-conserved Phase Field Model.” *Multi-Scale Model. & Charact. Of Infrastruct. Mater.*, RILEM 8, pp 127-138.

Hou, Y., Sun, W, Wang, L. and Pauli, T. (2014). “A phase field approach of viscoelastic fracture failure in asphalt mixture.” *International Journal of Pavement Engineering*. (Under review, submitted 2/16/2014)

current research of the asphalt cracking failure is focused on the single mode cracking, which is caused by compressive, tensile or torsion loading as shown in Figure 3-1:

- 1) Mode I crack- Opening mode (a tensile stress normal to the plane of the crack)
- 2) Mode II crack- Sliding mode (a shear stress acting parallel to the plane of the crack and perpendicular to the crack front)
- 3) Mode III crack – Tearing mode (a shear stress acting parallel to the plane of the crack and parallel to the crack front)

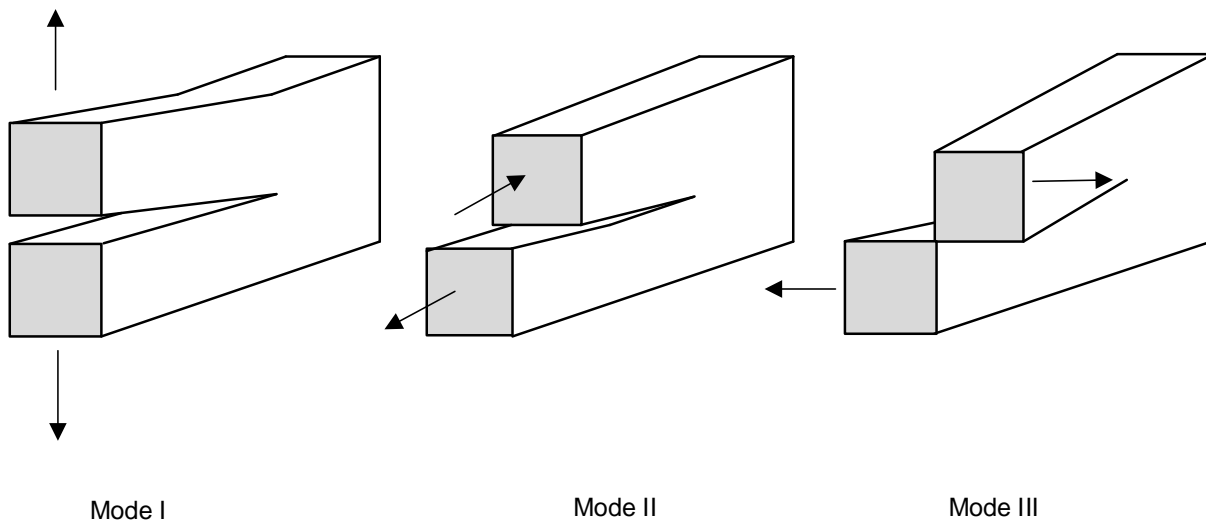


Figure 3-1 Three modes of crack

Asphalt fracture properties such as fracture toughness have been obtained from experiments. The Strategic Highway Research Program (SHRP) was the first to realize the importance of the fracture properties of asphalt binder [3]. The direct tension test (DTT) was used in SHRP to determine the strain-stress relationship and further determine the fracture properties of asphalt binders. Ponniah *et al.* followed the ASTM standard procedure [4] and obtained the fracture

energy of five different binders at $-30\text{ }^{\circ}\text{C}$ [5]. They also suggested that fracture energy can be used as a performance indicator of asphalt binders at low temperature. Hoare *et al.* followed Ponniah's experiment and tested some modified asphalt binders [6]. Their results show that the modified ones have larger fracture energy than the common asphalt binder and thus have a better resistance against tensile loading in the Mode I cracking test at a low temperature. Hesp summarized the previous research work and carried out very accurate experiments using an improved mold [7]. Till now, most of the analyses of fractures in asphalt binder are still based on the Classical Fracture Mechanics (CFM) [8] and thus limited by the initial crack geometry that is strictly defined in CFM.

In fracture, the phase field variable is used to identify the unbroken solid and the fully broken phase inside the crack, which is essentially not sensitive to the crack geometry and thus can be applied in a wider range than CFM. The system is driven by the chemical potential, which is the variation of the free energy with respect to the phase-field variable. There have been many versions of phase-field formulations for crack propagation. Both the non-conserved Allen-Cahn [9, 10] and conserved Cahn-Hilliard dynamics [11] have been used to evolve the phase-field variable, which all can successively capture the onset of crack propagation that agree with the Griffith criterion under certain pure mode loading conditions. Due to the non-conserved nature of crack growth, the Allen-Cahn dynamics has dominated the phase-field modeling of fractures. For example, Kuhn *et al.* adopted a non-double-well potential in his Allen-Cahn formulation and still captured the onset of crack propagation correctly [12]. Schanzel *et al.* applied the phase-field method to the crack propagation in rubber-like materials [13]. Song *et al.* used the phase-field method to investigate the effect of electric field on the crack propagation in a ferroelectric single crystal [14].

In this section, the development of an Allen-Cahn phase-field model that can be implemented in the commercial software COMSOL is presented. We will study Mode I, Mode II, Mixed Mode cracking and cracking interaction, respectively. The ultimate goal is to simulate the crack propagations in asphalt binder under complex loading conditions, which occurs in reality.

3.2 Mode I cracking

3.2.1 Free energy

As mentioned earlier, the phase field method uses a phase-field variable ϕ to describe the microstructure surface. In our model, the phase-field variable is set as $\phi = -1$ for the broken phase and $\phi = +1$ for the intact phase, and a diffuse interface separates the two phases. Following Yue *et al.* [15], the total free energy in the system can be written in the Landau-Ginzburg form:

$$F = \int_{\Omega} (f_{gr} + f_{loc} + f_{el})dV, \quad (3-1)$$

where

$$f_{gr} = \frac{1}{2}\lambda|\nabla\phi|^2 \quad (3-2)$$

is the gradient energy density,

$$f_{loc} = \frac{\lambda}{4\epsilon^2}(1 - \phi)^2(1 + \phi)^2 \quad (3-3)$$

is the local free energy (double-well potential) which has two minima at the two bulk phases, and f_{el} is the elastic energy. Here λ is the mixing energy density; and ϵ controls the interface thickness. The relationship between λ and ϵ is given in [16] as

$$\lambda = \frac{3\gamma\epsilon}{\sqrt{8}}, \quad (3-4)$$

where γ is the surface energy. In fracture simulations, $\gamma = \frac{G_c}{2}$, where G_c is the fracture energy, which is a material parameter.

Numerous experimental studies have shown that asphalt binders exhibit linear elastic isotropic behavior at high strain rates and low temperatures [17]. Consequently, the elastic energy density can be expressed as

$$f_{el} = \frac{E(\phi)}{2(1+\nu)} \left(\frac{\nu}{1-2\nu} (\varepsilon_{ii})^2 + \varepsilon_{ik}\varepsilon_{ik} \right), \quad (3-5)$$

where $E(\phi)$ is the elastic modulus and ν is Poisson's ratio. Based on the work of Wise *et al.* [18], we express $E(\phi)$ as

$$E(\phi) = E + (E - E_0)h(\phi) \quad (3-6)$$

where E and E_0 are the elastic moduli of the intact material and the broken phase respectively, and

$$h(\phi) = -\frac{1}{4}\phi^3 + \frac{3}{4}\phi + \frac{1}{2} \quad (3-7)$$

is an interpolation function that satisfies $h(-1) = 0$, $h(1) = 1$, and $h'(-1) = h'(1) = 0$. It should be noted that the elastic modulus in broken phase (which is physically a vacuum) should be zero and the Poisson's ratio is undefined. However, to avoid numerical singularity in elasticity calculations, we assume $E_0 = 0.01E$ due to the computational capability. It is expected that the smaller E_0 is, the more accurate the result will be. The Poisson's ratio is set to be $\nu = 0.3$ throughout the computational domain.

In a Lagrangian system, the infinitesimal strain tensor $\boldsymbol{\varepsilon}$ is obtained by

$$\boldsymbol{\varepsilon} = \frac{1}{2}(\nabla\mathbf{u} + (\nabla\mathbf{u})^T), \quad (3-8)$$

where \mathbf{u} is the displacement field. According to Hooke's law, the elastic stress is given by

$$\sigma_{ik} = \frac{E(\phi)}{1+\nu} \left(\varepsilon_{ik} + \frac{1}{1-2\nu} \delta_{ik} \varepsilon_{ii} \right). \quad (3-9)$$

The stress satisfies the force balance

$$\nabla \cdot \boldsymbol{\sigma} = 0, \quad (3-10)$$

which is eventually used to determine the displacement field. This elasticity part is handled by the structural analysis module in COMSOL.

3.2.2 Phase-field model

After we obtain the elastic energy, we can plug it into the phase-field model. Considering the fact that the volume of the crack phase grows during crack propagation, the following non-conserved Allen-Cahn equation is adopted:

$$\frac{\partial \phi}{\partial t} = -M\psi \quad (3-11)$$

where M is the mobility parameter that controls the propagation in asphalt, t means time and ψ is the chemical potential

$$\psi = \frac{\delta F}{\delta \phi} = -\nabla \cdot \lambda \nabla \phi + \frac{\lambda}{\epsilon^2} (\phi^2 - 1)\phi + \frac{\partial f_{el}}{\partial \phi} \quad (3-12)$$

The mobility parameter is usually expressed as $M = \chi \epsilon^2$ where χ is called the mobility tuning parameter which reflects the crack propagation speed. Note that $\frac{\partial f_{el}}{\partial \phi}$ is simply

$$\frac{\partial f_{el}}{\partial \phi} = h'(\phi) \frac{E-E_0}{2(1+\nu)} \left(\frac{\nu}{1-2\nu} (\varepsilon_{ii})^2 + \varepsilon_{ik} \varepsilon_{ik} \right) \quad (3-13)$$

Weak form of Equation (3-11) is needed for the calculation in COMSOL. From Equation (3-11) and (3-12), we get

$$\frac{\partial \phi}{\partial t} = -\lambda \chi (-\epsilon^2 \nabla \cdot \nabla \phi + (\phi^2 - 1)\phi + \frac{\epsilon^2}{\lambda} \frac{\partial f_{el}}{\partial \phi}) \quad (3-14)$$

Multiplying Equation (3-14) by the test function $\tilde{\phi}$ and then integrating over the computational domain, we get the weak form

$$\int_{\Omega} \frac{\partial \phi}{\partial t} \tilde{\phi} d\Omega = \int_{\Omega} -\lambda \chi (-\epsilon^2 (\nabla \cdot \nabla \phi) \tilde{\phi} + (\phi^2 - 1)\phi \tilde{\phi} + \frac{\epsilon^2}{\lambda} \frac{\partial f_{el}}{\partial \phi} \tilde{\phi}) d\Omega \quad (3-15)$$

Using Divergence Theorem, this equation can be further expressed as

$$\int_{\Omega} \frac{\partial \phi}{\partial t} \tilde{\phi} d\Omega = \int_{\Omega} -\lambda \chi \left(\epsilon^2 \nabla \phi \cdot \nabla \tilde{\phi} + (\phi^2 - 1)\phi \tilde{\phi} + \frac{\epsilon^2}{\lambda} \frac{\partial f_{el}}{\partial \phi} \tilde{\phi} \right) d\Omega + \int_{\partial \Omega} -\lambda \chi (\epsilon^2 \nabla \phi \cdot \mathbf{n} \tilde{\phi}) ds \quad (3-16)$$

Consider a stable situation of crack which means no flux across the boundary and thus the natural boundary condition is adopted

$$\nabla \phi \cdot \mathbf{n} = 0 \quad (3-17)$$

where \mathbf{n} is the unit vector outward pointing normal to $\partial \Omega$ such that the surface integral on $\partial \Omega$ vanishes. Consequently, Equation (3-17) is simplified to

$$\int_{\Omega} \frac{\partial \phi}{\partial t} \tilde{\phi} d\Omega = \int_{\Omega} -\lambda \chi \left(\epsilon^2 \nabla \phi \cdot \nabla \tilde{\phi} + (\phi^2 - 1)\phi \tilde{\phi} + \frac{\epsilon^2}{\lambda} \frac{\partial f_{el}}{\partial \phi} \tilde{\phi} \right) d\Omega \quad (3-18)$$

which is the equation that we input to COMSOL for solution.

3.2.3 Generalized Eshelby tensor and J - integral

In phase-field, the total energy potential is denoted as $\Psi = \Psi(\varepsilon_{ij}, \mathbf{x}, \phi, \nabla\phi)$ and the potential gradient is then obtained as shown in equation (3-19) based on the chain rule

$$\nabla\Psi = \frac{\partial\Psi}{\partial\varepsilon_{ij}}\nabla\varepsilon_{ij} + \frac{\partial\Psi}{\partial\phi}\nabla\phi + \frac{\partial\Psi}{\partial\nabla\phi} \cdot \nabla\nabla\phi + \left(\frac{\partial\Psi}{\partial\mathbf{x}}\right)_{expl} \quad (3-19)$$

where the explicit derivative of Ψ is given as as [19]

$$\left(\frac{\partial\Psi}{\partial x_k}\right)_{expl} = \frac{\partial}{\partial x_k} \Psi(\varepsilon_{ij}, x_m) |_{\varepsilon_{ij}=const., x_m=const. \text{ for } m \neq k} \quad (3-20)$$

The configurational force balance gives

$$\nabla \cdot \mathbf{b} + \mathbf{g} = 0 \quad (3-21)$$

where \mathbf{b} is the generalized Eshelby tensor given as [12]

$$\mathbf{b} = \Psi \mathbf{1} - \nabla \mathbf{u}^T \boldsymbol{\sigma} - \frac{\partial\Psi}{\partial\nabla\phi} \nabla\phi \quad (3-22)$$

and \mathbf{g} is the configurational body force term shown as [12]

$$\mathbf{g} = \frac{\partial\phi}{\partial t} \nabla\phi - \left(\frac{\partial\Psi}{\partial\mathbf{x}}\right)_{expl} \quad (3-23)$$

The traditional method to describe the cracking is by using the J – integral [20] shown as

$$J = \int_{\partial\Omega} (f_{el} dy - \mathbf{e}_x \cdot \nabla \mathbf{u}^T \cdot \mathbf{T} dS) \quad (3-24)$$

where f_{el} is the elastic strain energy in Equation (3-5), \mathbf{e}_x is the unit vector along x direction which is also the crack propagation direction and dS is the length increment along the given path $\partial\Omega$ shown in Figure 3-1. $\mathbf{T} = \boldsymbol{\sigma} \cdot \mathbf{n}$ is the traction vector, where $\hat{\mathbf{n}}$ is the unit vector normal to $\partial\Omega$.

Kuhn *et al.* (2010) split the generalized Eshelby tensor in Equation (3-22) to two parts as the elastic energy part and the gradient energy part [12]. In our formulation, we denote them as

$$\mathbf{b}^{el} = f_{el} \mathbf{1} - \nabla \mathbf{u}^T \boldsymbol{\sigma} \quad (3-25)$$

and

$$\mathbf{b}^{gr} = (f_{local} + f_{gr}) \mathbf{1} - \frac{\partial \Psi}{\partial \nabla \phi} \nabla \phi = \left(\frac{\lambda}{4\epsilon^2} (1 - \phi)^2 (1 + \phi)^2 + \frac{1}{2} \lambda |\nabla \phi|^2 \right) \delta_{ij} - \frac{\partial \Psi}{\partial \nabla \phi} \nabla \phi \quad (3-26)$$

Based on Equation (3-21) and integrate the configurational force over the body, we have

$$\int_{\Omega} \nabla \cdot \mathbf{b} \, dV + \int_{\Omega} \mathbf{g} \, dV = 0 \quad (3-27)$$

Using Divergence Theorem, we rewrite the integral of the divergence of Eshelby tensor \mathbf{b} as a contour integral on the boundary $\partial\Omega$, which is

$$\int_{\partial\Omega} \mathbf{b} \cdot \mathbf{n} \, dS + \int_{\Omega} \mathbf{g} \, dV = 0 \quad (3-28)$$

Note that the contour boundary $\partial\Omega$ can be split into two parts as shown in Figure 3-2: $\partial\Omega: A \rightarrow B$ on the integration circle $\partial\Omega$ and $\partial\Omega: B \rightarrow A$ on the same calculation domain, which means

$$\int_{\partial\Omega: B \rightarrow A} \mathbf{b} \cdot \mathbf{n} \, dS + \int_{\partial\Omega: A \rightarrow B} \mathbf{b} \cdot \mathbf{n} \, dS + \int_{\Omega} \mathbf{g} \, dV = 0 \quad (3-29)$$

And further

$$\int_{\partial\Omega:B \rightarrow A} \mathbf{b}^{el} \cdot \mathbf{n} dS + \int_{\partial\Omega:B \rightarrow A} \mathbf{b}^{gr} \cdot \mathbf{n} dS + \int_{\partial\Omega:A \rightarrow B} \mathbf{b}^{el} \cdot \mathbf{n} dS + \int_{\partial\Omega:A \rightarrow B} \mathbf{b}^{gr} \cdot \mathbf{n} dV + \int_{\Omega} \mathbf{g} dV = 0 \quad (3-30)$$

Since the elastic energy and stress vanish in the internal crack the elastic integral over $\partial\Omega: B \rightarrow A$ can be neglected. As the gradient energy only exists across crack surface, it vanishes on $\partial\Omega: A \rightarrow B$.

$$\int_{\partial\Omega:B \rightarrow A} \mathbf{b}^{gr} \cdot \mathbf{n} dS + \int_{\partial\Omega:A \rightarrow B} \mathbf{b}^{el} \cdot \mathbf{n} dS + \int_{\Omega} \mathbf{g} dV = 0 \quad (3-31)$$

Over $\partial\Omega: A \rightarrow B$ where the phase-field variable $\phi = 1$, the integral $\int_{\partial\Omega:A \rightarrow B} \mathbf{b}^{el} \cdot \mathbf{n} dS = \begin{pmatrix} J \\ 0 \end{pmatrix}$ degenerates to the classic J -integral as we have stated in Equation (3-24).

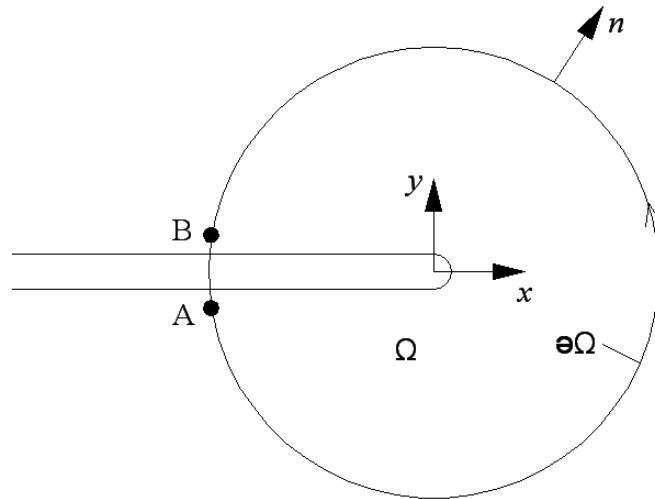


Figure 3-2 Mode I cracking contour

To solve the integral of the gradient part on $\Omega: B \rightarrow A$, we consider the one-dimensional situation of equation (26) and obtained the result based on the contributions of Yue *et al.* [21], which reads

$$\int_{B \rightarrow A} \mathbf{b}^{gr} \cdot \hat{\mathbf{n}} dS = - \int \left(\frac{2f_{surf}}{0} \right) dS = - \left(\frac{2\gamma}{0} \right) \quad (3-32)$$

where γ is the surface energy. Here we have used the relation that $f_{surf} = \int_{-\infty}^{+\infty} \left\{ \frac{\lambda}{4\epsilon^2} (1 - \phi)^2 (1 + \phi)^2 + \frac{1}{2} \lambda \left(\frac{d\phi}{dx} \right)^2 \right\} dx = \gamma$ for a planar diffuse interface. Note that two diffuse interfaces are crossed from B to A, so we have -2γ in Equation (3-32), which is different from Kuhn's result [12]. And finally the x -component of Equation (3-31) can be expressed as

$$J - 2\gamma + \int_{\Omega} g_x dV = 0, \quad (3-33)$$

where $g_x = \frac{1}{M} \frac{\partial \phi}{\partial t} \frac{\partial \phi}{\partial x}$ is the x -component of \mathbf{g} and we have neglected $\left(\frac{\partial \Psi}{\partial x} \right)_{expl.}$ in Equation (3-23).

For crack propagation, $\frac{\partial \phi}{\partial t} \leq 0$ and $\frac{\partial \phi}{\partial x} > 0$, thus $\int_{\Omega} g_x dV \leq 0$, which gives $J \geq 2\gamma$. This shows that under Mode I cracking our phase-field theory fundamentally agrees with the Griffith's theory, in which the crack propagates when the elastic energy is large enough to created two new surfaces.

3.2.4 Simulation of mode I crack propagation

A two-dimensional finite element model is established in COMSOL for the fracture analysis under tension loading. A fixed Eulerian mesh is used to describe the internal interfaces between the intact solid and crack void. Six-node triangular elements (P2) are used in our finite element

calculations. 30,283 elements are used in the initial mesh. The mesh refines adaptively at the interface, as shown in Figure 3-3, to resolve the ϕ profile across the interface.

We consider plane strain and the computational domain is a square with side length $L = 0.1 \text{ m}$. We choose the interfacial thickness $\epsilon = 0.01 L = 0.001 \text{ m}$ and the initial crack length $a = 20\epsilon = 0.02 \text{ m}$. Because of the diffuse nature of the phase-field method, we need to impose a finite crack width, which we use $W = 0.005 \text{ m}$ in this simulation. The finest mesh size is set to be $\Delta x = \frac{1}{33} W$ (i.e., $\epsilon \approx 6.6\Delta x$) which sufficiently resolves the diffuse interface [15, 16].

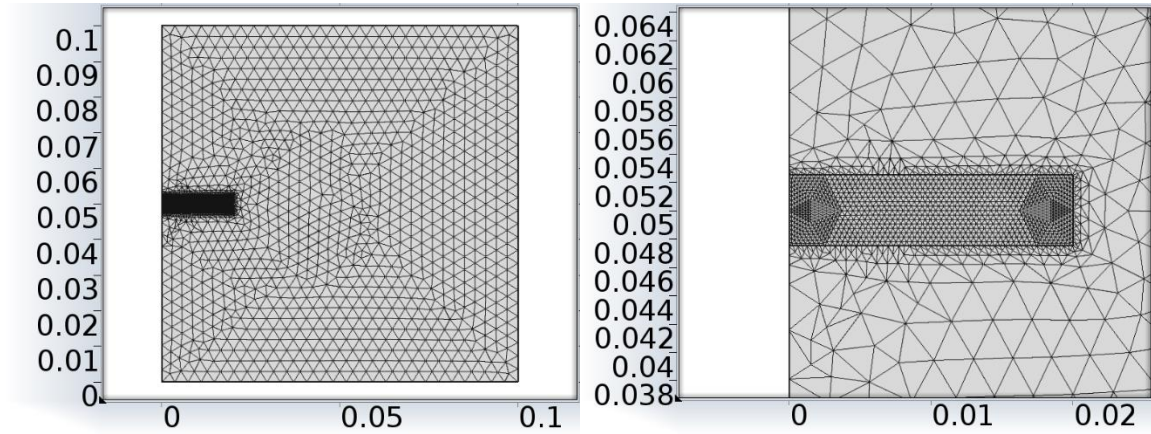


Figure 3-3 (a) Unstructured triangular mesh generated by COMSOL (b) Magnified view of the crack

Figure 3-4 shows that pure tension loading is applied on top and bottom boundaries. For convenience we set the bottom boundary as fixed in our simulation. Kuhn *et al.* suggested a tension loading that increases linearly with time until the critical loading, at which the crack starts to propagate, is reached [12]. We follow this idea and choose $\sigma(t) = \frac{\sigma_0}{t_0} \cdot t$ where $\frac{\sigma_0}{t_0} = 2 \times 10^6 \frac{\text{N}}{\text{m}^2\text{s}}$ to simulate the fracture process.

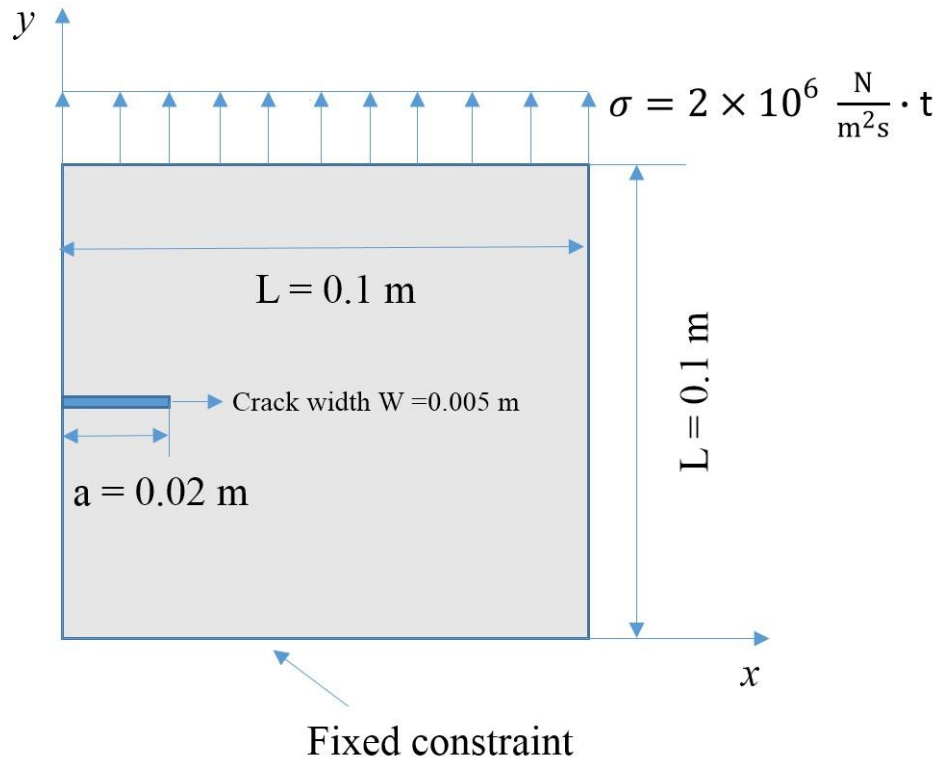


Figure 3-4 Pure tension loading is applied on our model

Crack propagation at different time instants is shown in Figure 3-5. The snapshots are taken at time steps = 0, 72, 76 and 83 respectively, where the time step interval $\Delta t = 0.001 \text{ s}$, $\gamma = 183.77 \text{ J/m}^2$, $E = 5.8 \text{ Mpa}$. Note that the elastic modulus and surface energy are chosen to be the same as the asphalt binder in the Direct Tension Test in the next section. Poisson's ratio is chosen as 0.3. It can be clearly seen that crack propagates along the x direction while there is a diffuse interface between the crack phase and the intact phase. It should be noted that ϕ may not be exactly in $[-1, 1]$ in the simulations. However, the deviation is always less than 3%, and therefore can be neglected. Limited by our computational power, we use a relatively coarse mesh which may smooth out the possible crack branching as shown by Spatschek *et al.* [22]. The crack direction is almost straight along the x axis, which is reasonable since the stress field is

symmetric about the crack. An expected result of the propagation is the model failure, the direction of which should be straight along the x axis.

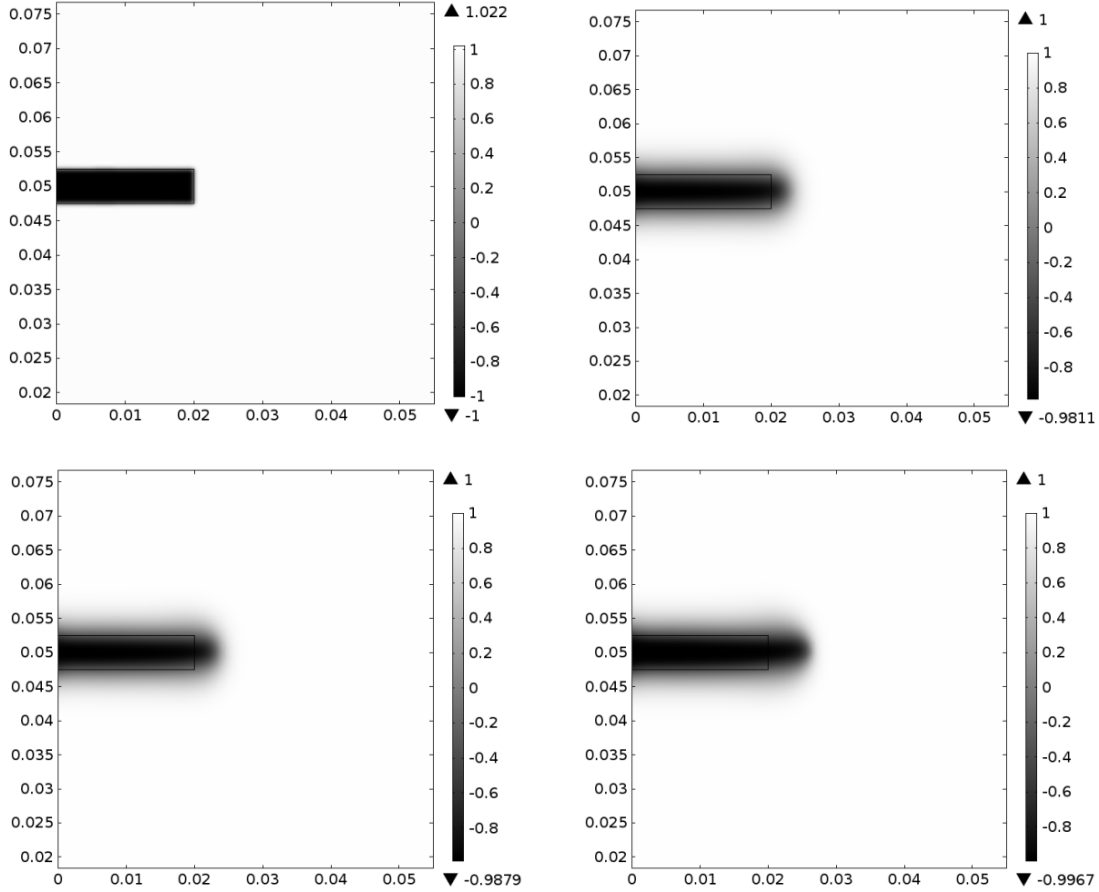


Figure 3-5 Magnified view of crack propagation

3.2.5 Experiments and comparisons

In order to verify the PFM for mode I cracking, we simulate two types of standard test specimens used in fracture toughness measurements.

3.2.5.1 Direct tension test

Experiments are conducted to find out reasonable fracture parameters and to provide benchmarks for our phase-field simulations. The Direct Tension Tester (DTT) of Interlaken Technology Corporation is the main instrument used for testing.

The asphalt binder used in our experiment is a pure asphalt binder with PG 64-22 based on Superpave specification. The binder is obtained from the Asphalt Plant of the Roanoke city. Figure 3-6 shows the geometry of an asphalt binder specimen and the thickness is 6mm. The specimen is prepared in an aluminum mold, and glycerin mixture is brushed on the mold surface to prevent asphalt binder from sticking onto the mold. Two plastic ends are attached to the specimen so that the specimen can be put in the Direct Tension Tester. An initial crack is cut at one edge of the specimen. Five crack lengths are adopted to provide benchmarks for PFM: 5 mm, 8 mm, 9 mm, 11 mm and 13 mm. The specimen is then put in a chamber that keeps the temperature at -20°C using the Julabo cooling system. There are two reasons why the crack length a cannot be too small or too large. First, in the numerical simulations, the crack width is not negligible. To fully resolve the crack, we choose the crack width to be $10\epsilon = 0.5\text{mm}$. In order to reduce the effect of finite width on the cracking simulations, we have to choose a crack length which is much larger than the width. We have found that the computational results are acceptable when the crack length is at least 10 times of the width. Second, in the experiments, if the crack length is too large, the specimen may break due to the disturbances during preparation.

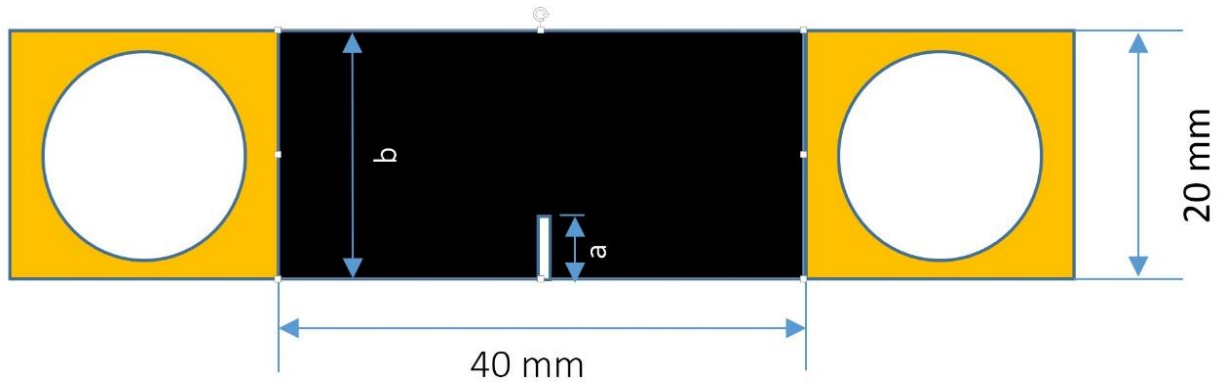


Figure 3-6 Geometry of asphalt binder specimen for crack testing

The asphalt binder specimen is fixed on the right end, and a tensile force that increases with time is applied on the left end at a rate of 10 N/s. Both the force and the corresponding displacement are recorded in the computer throughout the experiment. At -20 °C, the specimen will suddenly break apart when the tensile load reaches a critical value. The corresponding stress intensity factor can be calculated using Equation (3-35).

In order to reduce the random errors, 10 specimens are prepared for each crack length. The direct tension test is conducted on all the specimens, and the average critical load is selected as the representative critical load for the specimen with that crack length. Figure 3-7 to Figure 3-9 show three typical fracture test results. There are some negative displacements because the machine calibrates the displacement measurement in each test. It is noted that the load-stroke relationship is almost linear during loading. Figure 3-10 shows the broken asphalt specimen after DTT test.

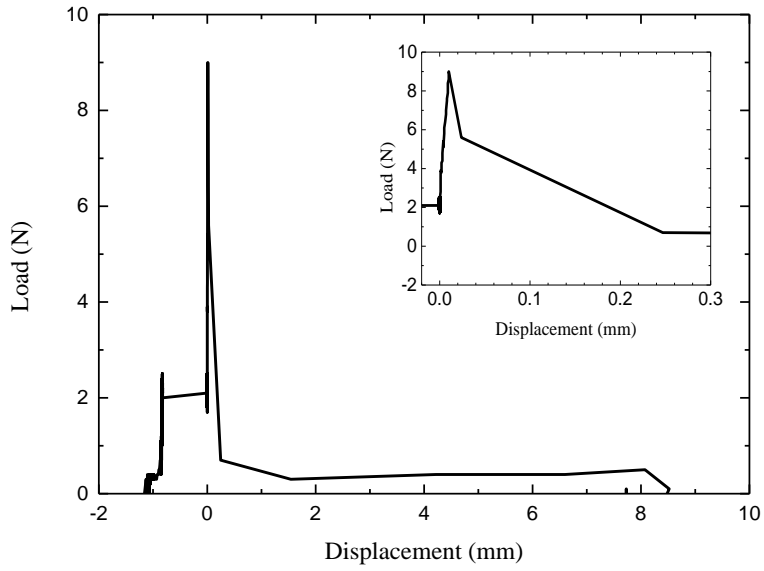


Figure 3-7 One representative fracture process with initial crack length 9 mm

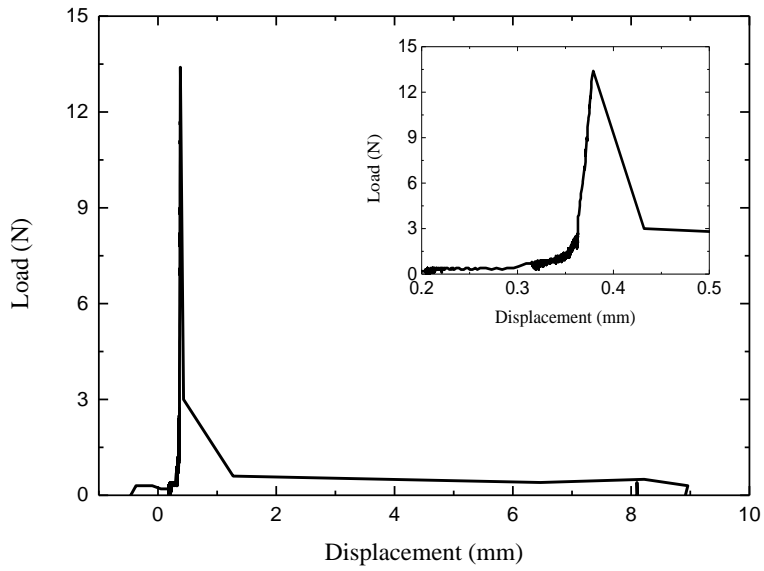


Figure 3-8 One representative fracture process with initial crack length 8 mm

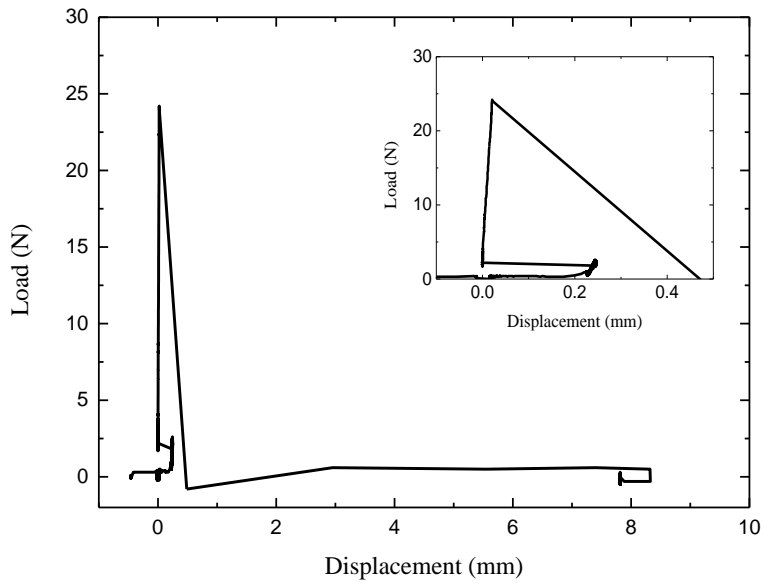


Figure 3-9 One representative fracture process with initial crack length 5 mm

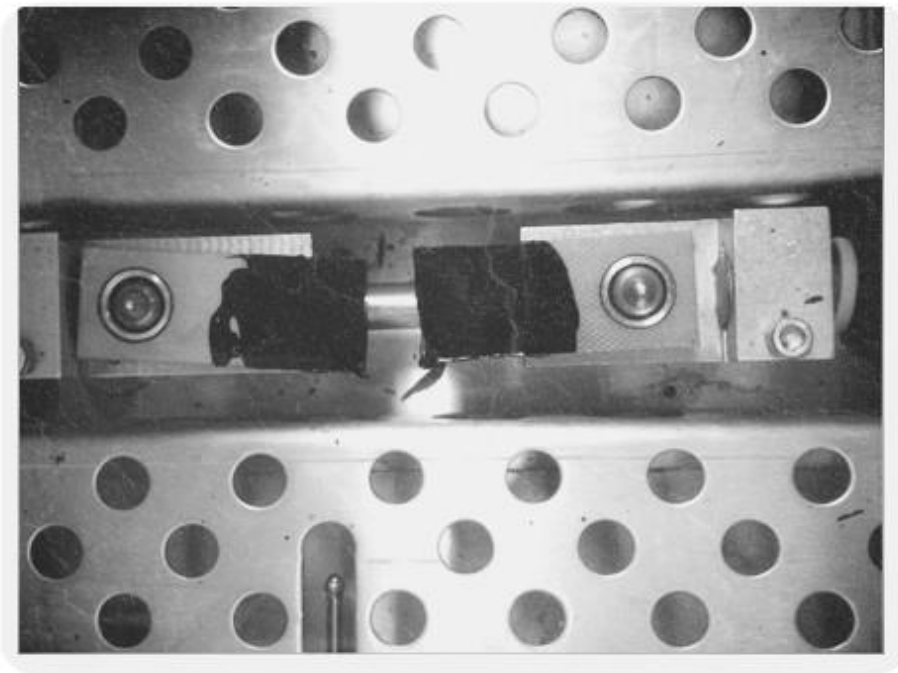


Figure 3-10 The broken specimen after tension loading

In the classic fracture mechanics [8, 23], the Griffith criterion for Mode I crack growth reads

$$K_I \geq K_{Ic} \quad (3-34)$$

where K_I is the mode I stress intensity factor and K_{Ic} is the mode I fracture toughness which is a material parameter. For the direct tension test specimen, the stress intensity factor is related to the tensile stress as [23]

$$K_I = \sigma \sqrt{\pi a} \sqrt{\frac{2b}{\pi a} \tan \frac{\pi a}{2b}} D \left(\frac{a}{b}\right) \quad (3-35)$$

where a is the crack length, b is the specimen width (c.f. Figure 3-7), and

$$D = \frac{0.752 + 2.02 \frac{a}{b} + 0.37 \left(1 - \sin \frac{\pi a}{2b}\right)^3}{\cos \frac{\pi a}{2b}} \quad (3-36)$$

The corresponding fracture energy is then determined from

$$G_c = \frac{K_{Ic}^2 (1 - \nu^2)}{E} \quad (3-37)$$

Ponniah *et al.* tested 5 different asphalt binders and reported K_{Ic} that ranges from $48.4 \text{ kNm}^{-3/2}$ to $70.1 \text{ kNm}^{-3/2}$ [5]. In our calculations, we choose $K_{Ic} = 48.4 \text{ kNm}^{-3/2}$. The elastic modulus of asphalt specimen is 5.8 MPa based on the stress-strain relationship by the uniaxial tensile test at $-20 \text{ }^\circ\text{C}$ besides the cracking test, which corresponds to a fracture energy $G_c = 367.54 \text{ J/m}^2$. The uniaxial tension testing is a force-controlled test. The applied load at two ends of the specimen is set to increase linearly with time at 10 N/s and the sample dimensions are 40 mm (length) \times 20 mm (width) \times 6 mm (thickness).

Note that this fracture energy actually includes contributions from both the reversible surface energy and many irreversible processes such as plastic dissipation. In the phase-field theory, both contributions are lumped into the surface energy or surface tension, i.e.,

$$G_c = 2\gamma \quad (3-38)$$

Table 3-1 Comparison of Critical Fracture Stress by Three Approaches

Crack length (mm)	Experiment (MPa)	CFM (MPa)	PFM (MPa)
5	0.212	0.259	0.25
8	0.1274	0.145	0.16
9	0.0844	0.119	0.145
11	0.06917	0.0778	0.091
13	0.050833	0.0480	0.052

The comparison between experimental results, CFM and PFM calculations is shown in Table 3-1. The computational domain of PFM is set according to the geometry of test specimen as shown in Figure 3-5. It should be noted that in PFM, the critical fracture stress is considered as the loading stress at the time instant when ϕ at the crack tip reaches -1. The good agreement between experimental results and CFM at $a = 5\text{mm}$, 8 mm , 11mm and 13 mm indicates that the current choice of $K_{IC}=48.4\text{ kNm}^{-3/2}$ is acceptable (relative errors are 17.92%, 25.58%, 31.56% and 21.97%, correspondingly). At all crack lengths, the PFM matches CFM well (relative errors are 3.48%, 10.34%, 21.85%, 16.97% and 8.3%, correspondingly). Due to the extra dissipation associated with the Allen-Cahn equation, the phase-field simulations require slightly higher

stresses to advance the crack than the CFM predictions. This observation is also reported by Eastgate *et al.* in their conserved Cahn-Hilliard simulations of crack propagation [11].

3.2.5.2 Three-point bending test

The three-point bending beam method, as shown in Figure 3-11, is a standard testing method to determine fracture toughness in ASTM (1990). Hesp carried out a series of experiments on asphalt binders using this method [7]. In his experiments, the failure load is measured and the fracture energy is determined from a stress-strain relationship. To validate our phase-field method, we simulate the three-point bending specimen with the fracture energies obtained from experiments, and then compare the failure loads with experiments. The elastic modulus, Poisson's ratio and fracture energy are all adopted from Hesp's results [7].

The critical failure load from both Hesp's experiments and simulations are shown in Figure 3-12 and Table 3-2. Since the specimen reaches the glass transition temperature at -27°C , it is very brittle in his experiment. The failure occurs almost immediately after the crack starts to propagate. In the phase-field simulations, we apply a force load that increases with time and pick the load value at the time instant when ϕ at the crack tip reaches -1 to be the critical load. We can see that the numerical results match very well with the experimental results obtained by Hesp. Based on Table 3-1 and Table 3-2, it can be seen that PFM is capable of simulating fast Mode I fracture of asphalt binder of small specimen configurations at a low temperature. However, note that our current PFM is not suitable for ductile fracture and cracking analysis when considering viscous effect.

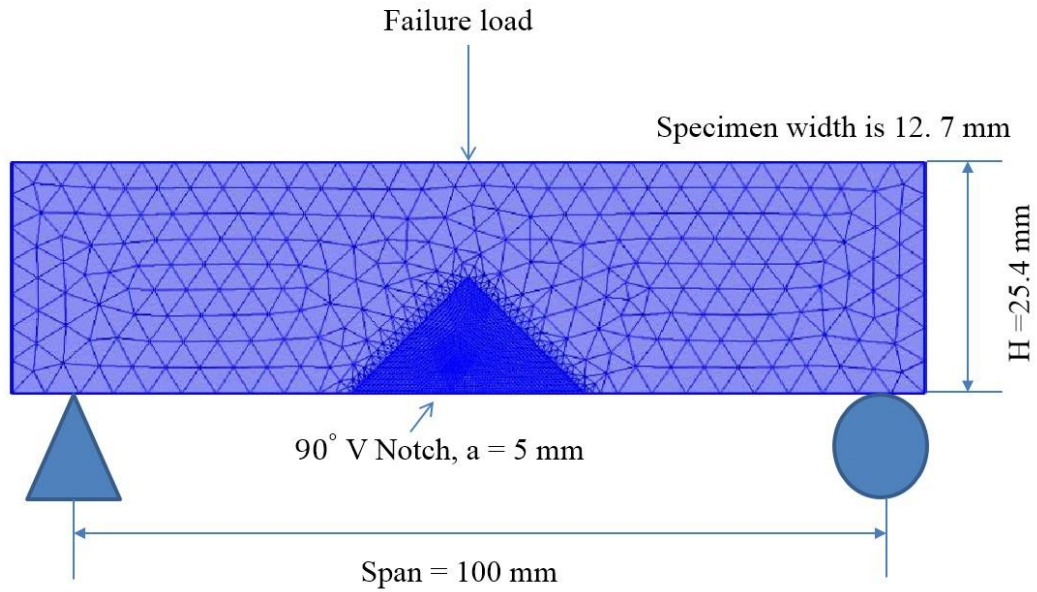


Figure 3-11 Determination of the failure load with an initial V notch crack

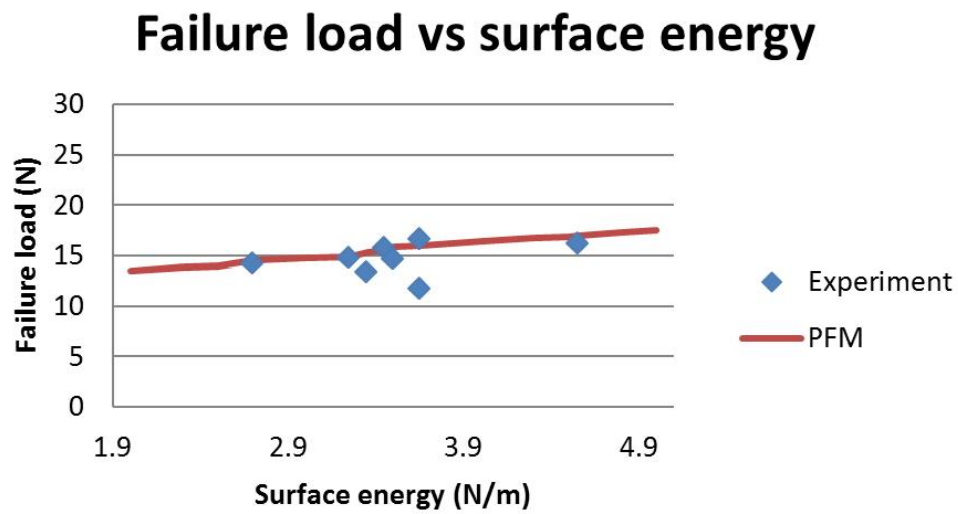


Figure 3-12 Comparison of failure load with respect to surface energy between experiment and PFM

Table 3-2 Comparison of The Failure Load Between Experiment and PFM

Sample	Fracture E (J/m^2)	Surface energy (J/m^2)	Failure load	
			Experiment (N)	PFM (N)
1	6.5	3.25	14.7	14.9
2	6.9	3.45	15.7	15.5
3	9.1	4.55	16.1	15.7
4	6.7	3.35	13.3	15.3
5	7.3	3.65	16.6	16
6	5.4	2.7	14.2	14.5
7	7.3	3.65	11.7	16

3.2.6 Summary

In this section, we present a non-conserved phase field model for mode I cracking failure in asphalt binders at a low temperature. Tests on two types of specimens, namely, the direct tension specimen and the three-point bending specimen, are simulated. Experiments of direct tension tests are also conducted to verify the reasonable choice of fracture properties of asphalt binder. The critical loadings that lead to crack propagation agree very well with those predicted using classical fracture mechanics. Due to the extra dissipation associated with the phase-field equation, the critical loads obtained in the simulations are always slightly greater than those predicted by classical fracture mechanics. Overall, compared with the classic fracture mechanics, the Phase-field model does not need to explicitly treat the crack surface and can easily handle the

topological changes. It is capable of simulating Model I fast fracture in asphalt binder with reasonable accuracy, which will lead to a better quantitative understanding of the binder behavior.

However, there are still several aspects that are not covered by the current work and need further investigation. For example, in the real cracking process, there may be energy loss due to temperature variance, plastic deformation, viscous dissipation, etc.; the asphalt binder may not be linearly elastic, especially at a temperature above -20°C ; the asphalt binder, which is a mixture of several components, may exhibit nonhomogenous properties and require multi-component simulations. All these issues will be addressed in our future work. The fatigue cracking, which is one of the principal distresses that affect the design life of asphalt pavements, also needs to be investigated. At present, the simulations of mixed mode fractures and interactions between multiple fractures are already ongoing.

3.3 Mode II cracking

Mode II cracking usually happens when putting on the brake although it does not happen as common as Mode I cracking. Besides the Mode I cracking research, some researchers has also done experiments and analyses of Mode II cracking. Braham et al. (2009) studied the Mode II fracture of asphalt concrete and discovered that the Mode II test tends to transition into a sliding friction test [24], unlike the Mode I test. Repeat the steps in the Mode I cracking section, we can similarly establish the Mode II cracking simulation.

Consider a homogeneous model of asphalt concrete and use a two-dimensional finite element model to simulate the cracking process in COMSOL under shear loading. A fixed Eulerian mesh is used to describe the internal interfaces between the intact solid and crack void. The mesh refines adaptively at the interface, as shown in Figure 3-13, to resolve the ϕ profile across the

interface. As we can see, a double – notch exist on both edges. And then two edges will move in the opposite direction so that shear stress will make the initial crack propagate.

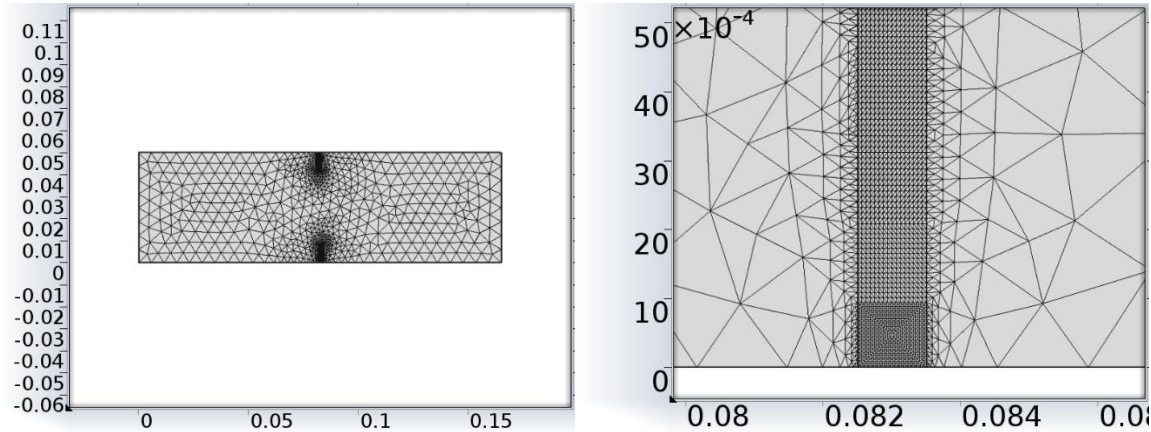


Figure 3-13 (a) Unstructured triangular mesh generated by COMSOL with interfacial refinement (b) Magnified view of crack

We consider plane strain and the computational domain is a rectangular with length 0.165m and width 0.05m. We then choose the interfacial thickness $\epsilon = 0.0004 \text{ m}$ and the initial crack length $a = 0.008 \text{ m}$. Because of the diffuse nature of the phase-field method, we need to impose a finite crack width, which we use $W = 0.001 \text{ m}$ in this simulation. The finest mesh size is set to be $\Delta x = \frac{1}{33} W$ (i.e., $\epsilon \approx 6.6 \Delta x$) as previously.

Figure 3-14 shows that shear movement happens on top and bottom boundaries where the velocity is 0.0002 m/s. The elastic modulus is set as 3450MPa.

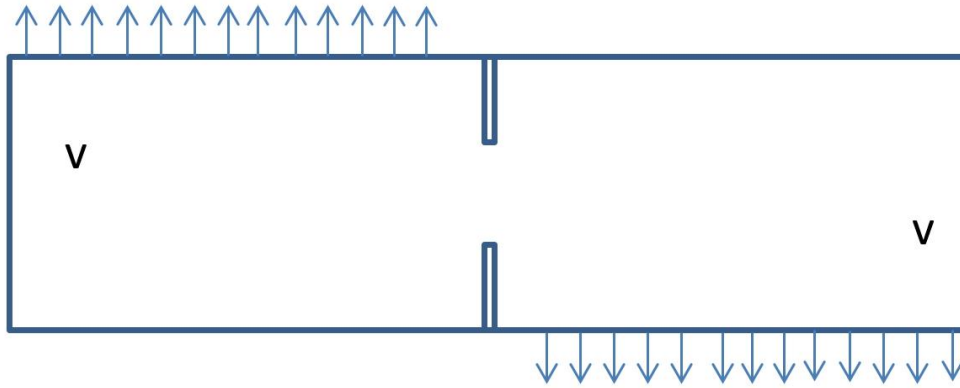


Figure 3-14 Opposite movements happens on top and bottom boundaries

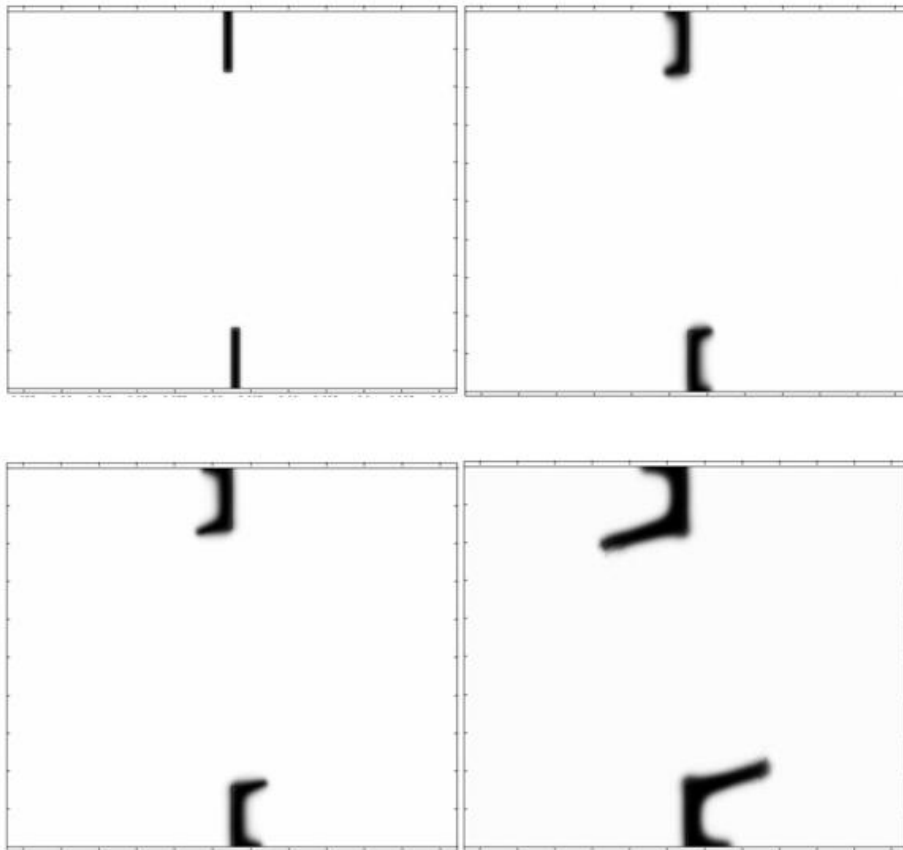


Figure 3-15 Magnified view of crack propagation. The snapshots are taken at $t=0$, $15 \Delta t$, $20 \Delta t$ and $60 \Delta t$ where $\Delta t = 0.01s$ is the time step used in the simulation. $\gamma = 100 J/m^2$

Crack propagation at different time instants is shown in Figure 3-15. The dark part represents the crack state while the white part represents the intact state. It can be clearly seen that crack propagates by applying the boundary moving condition while there is a diffuse interface between the crack phase and the intact phase.

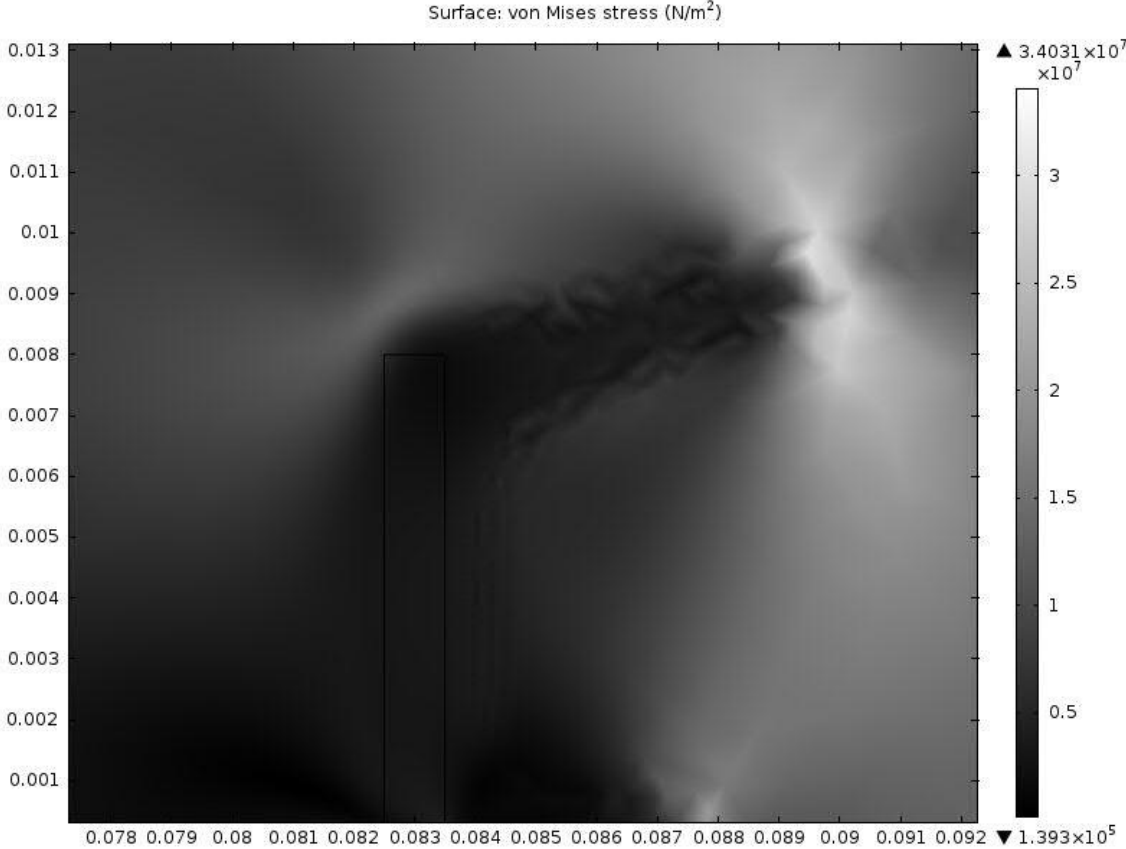


Figure 3-16 Magnified view of von Mises stress distribution near crack tip at $t=30 \Delta t$

As expected, there is a stress concentration at the crack tip, as shown in Figure 3-16. In the region near the crack tip, the von Mises stress is much larger than that in the intact regions in front of the crack. Immediately above and below the crack, the stress is much lower than the average, since the elastic energy has been released to create new fracture surface area. This observation is in agreement with the classical fracture mechanics.

3.4 Mixed Mode Cracking (Mode I & II)

We have presented the Mode I and Mode II cracking research in the previous sections. However, in the real situation the loading condition is much more complex, and is generally mixed-mode such as the combination of tension and shear loading (Mode I & II), tension and torsion loading (Mode I & III), etc. The possible formation and propagation of mixed mode cracking will cause serious distresses in asphalt materials and will affect the normal pavement use. Braham *et al.* (2010) conducted laboratory experiment of mixed mode cracking of asphalt binder [25]. Their result show that the fracture work increases as the level of Mode II increase.

In this section, considering that the crack phase always develops in the system, the development of a non-conserved Allen-Cahn phase-field model is implemented in the commercial finite element software COMSOL. The model is validated by comparing the two-dimensional simulations of mixed-mode cracking and comparison with the experimental results. The ultimate goal is to simulate the crack propagation in asphalt binder under various complex loading conditions (Mode I & II, I & III, I & II & III etc.), which occur in reality.

3.4.1 Generalized Eshelby tensor and J - integral

Note that the energy potential proposed in the Mode I cracking section could also be employed in this section. The only difference between Mode I cracking and Mixed mode cracking is the obtaining of Mixed-mode J -integral as shown in Figure 3-17.

We first set the calculation body as Ω and contour over the boundary as $\Gamma = \Gamma_1 + \Gamma_2 + \Gamma_3 + \Gamma_4$ around the crack tip shown in Figure 3-14, where Γ_4 is the major arc from $B \rightarrow A$ and Γ_5 is the minor arc from $A \rightarrow B$.

We can further integrate equation (3-21) over the body Ω as

$$\int_{\Omega} \nabla \cdot b \, dV + \int_{\Omega} g \, dV = 0 \quad (3-39)$$

Using Divergence Theorem, the integral of the body can be derived as the contour integral over the boundary as

$$\int_{\Gamma} b \, dS + \int_{\Omega} g \, dV = 0 \quad (3-40)$$

Note the contour boundary can be split into four parts, which means

$$\int_{B \rightarrow A} b \, dS + \int_{A \rightarrow B} b \, dS + \int_{\Omega} g \, dV = 0 \quad (3-41)$$

which is

$$\int_{\Gamma_1} b \, dS + \int_{\Gamma_2} b \, dS + \int_{\Gamma_3} b \, dS + \int_{\Gamma_4} b \, dS + \int_{\Omega} g \, dV = 0 \quad (3-42)$$

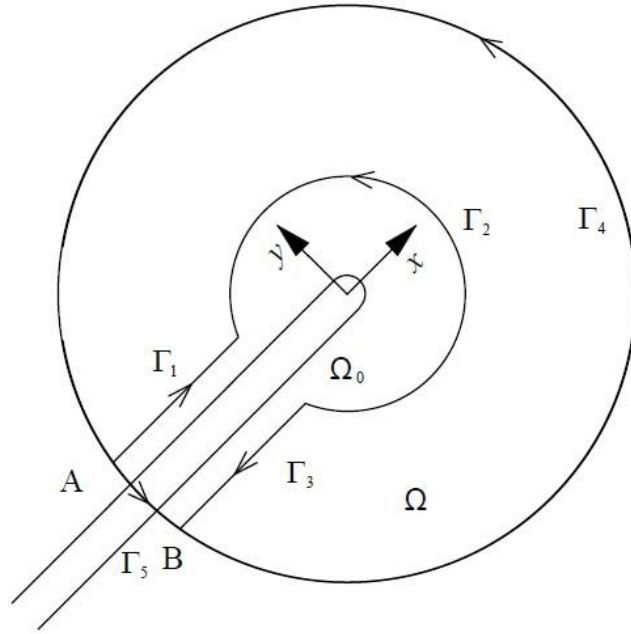


Figure 3-17 Phase field contour in the mixed mode cracking

The contour integral over Γ_1 , Γ_2 and Γ_3 should be equal to contour integral over Γ_5 since the total contour integral over Γ_1 , Γ_2 , Γ_3 and Γ_5 is zero because it's closed, which means

$$\int_{\Gamma_1} b dS + \int_{\Gamma_2} b dS + \int_{\Gamma_3} b dS - \int_{\Gamma_5} b dS = 0 \quad (3-43)$$

The negative sign used before the term of contour integral over Γ_5 is because it represents the integration direction from $A \rightarrow B$ but not from $B \rightarrow A$ to make the contour closed.

Move the integration term over Γ_5 to the right hand side of equation (3-43) and we have

$$\int_{\Gamma_1} b dS + \int_{\Gamma_2} b dS + \int_{\Gamma_3} b dS = \int_{\Gamma_5} b dS \quad (3-44)$$

Consider equation (3-40) and equation (3-44), we have

$$\int_{\Gamma_4} b dS + \int_{\Gamma_5} b dS + \int_{\Omega} g dV = 0 \quad (3-45)$$

Since Γ_4 represents the intact material state where phase-field variable $\phi = 1$ and under this circumstance, no surface energy exists on this contour and the integration term over Γ_4 in equation (3-45). For integration over Γ_5 , since it represents the cracking state ($\phi = -1$), there is no stress or elastic energy inside but surface energy.

Consider the one-dimensional situation from $A \rightarrow B$ and obtained the result from [21], we can see the situation degenerates to the normal Mode I cracking as we have derived previously, i.e.,

$$J - 2\gamma + \int_{\Omega} g dV = 0 \quad (3-46)$$

Leave the body force term to one side of the equation and we have

$$\int_{\Omega} g dV = -(J - 2\gamma) \quad (3-47)$$

Note the expression for the body force term is given in equation (3-23). For crack propagation, $\frac{\partial \phi}{\partial t} \leq 0$ and thus $\int_{\Omega} g dV \leq 0$, which gives $J \geq 2\gamma$. It is seen that under mixed mode cracking our phase-field theory fundamentally agrees with the Griffith's theory that crack propagates when the elastic energy is large enough to create two new surfaces. It is noted that our mixed surface energy model does not split the mixed mode cracking to Mode I and Mode II like the other researcher did in [25]. The mixed mode surface energy is the only criterion for the crack to propagate in our model, where it may be expressed as a function of the Mode I surface energy and Mode II surface energy.

3.4.2 A simple simulation

A two-dimensional finite element model for the mixed mode cracking analysis by using COMSOL, where plane strain is employed for convenience. A fixed Eulerian mesh is used to describe the internal interfaces between the intact solid and crack void. The mesh refines adaptively at the interface, as shown in Figure 3-18, to resolve the ϕ profile across the interface. One thing should be mentioned is that the units show model geometry in Figure 3-18 and Figure 3-20 are centimeters. Our model is a square with side length $L = 0.1$ m. The interfacial thickness is then selected as $\epsilon = 0.01 L = 0.001$ m and the initial crack length $a = 40\epsilon = 0.04$ m. In order to generate a mixed mode cracking, the crack direction is set 45° with the x -axis as shown in Figure 3-19 while the external loading is a tension loading vertical to the top and bottom boundary. Note we impose a finite crack width, which we use $W = 0.005$ m in this simulation. Because of the diffuse nature of the phase-field method.

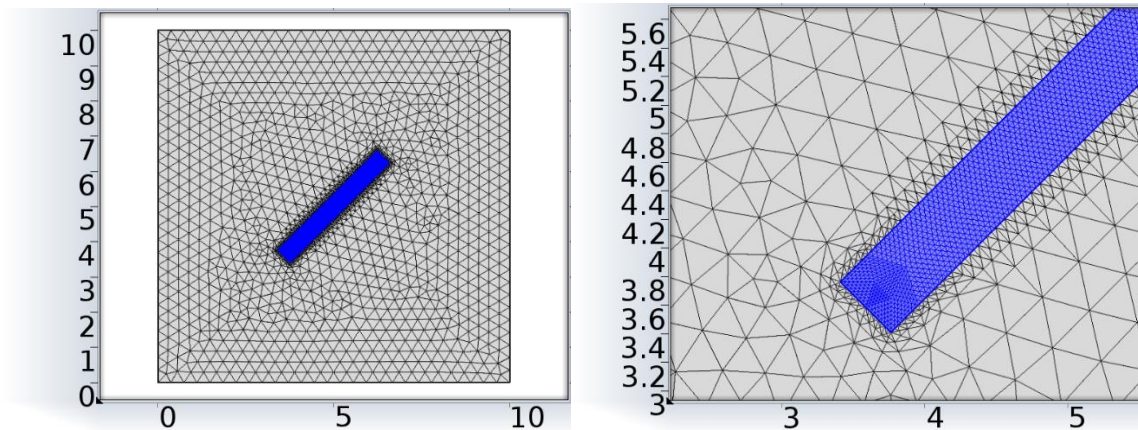


Figure 3-18 (a) Unstructured triangular mesh generated by COMSOL with interfacial refinement. (b) Magnified view of the crack

Figure 3-19 shows that pure tension loading is applied on top and bottom boundaries. For convenience we set the bottom boundary as fixed and the tension loading is given increases linearly with time until the critical loading at which the crack starts to propagate is reached. Set

$$\sigma(t) = \frac{\sigma_0}{t_0} \cdot t \text{ where } \frac{\sigma_0}{t_0} = 2 \times 10^6 \frac{\text{N}}{\text{m}^2\text{s}}.$$

Crack propagation at different time steps is shown in Figure 3-20. The black region represents the crack part while the white region represents the intact part. It can be clearly seen that crack propagates and changes from the initial direction while there is a diffuse interface (controlled by ϵ) between the crack phase and the intact phase. It should be noted that under the current force loading condition, the crack propagation is not stable once it starts.

As expected, there is a stress concentration at the crack tip, as shown in Figure 3-21. In the region near the crack tip, the von Mises stress is much larger than that in the intact regions in front of the crack. Immediately above and below the crack, the stress is much lower than the average (1.42×10^5 Pa), since the elastic energy has been released to create the new fracture surface area.

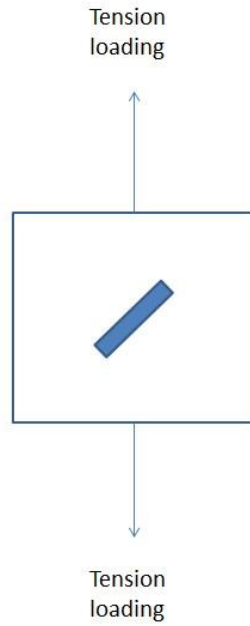


Figure 3-19 Tension loading applied on the mixed mode cracking

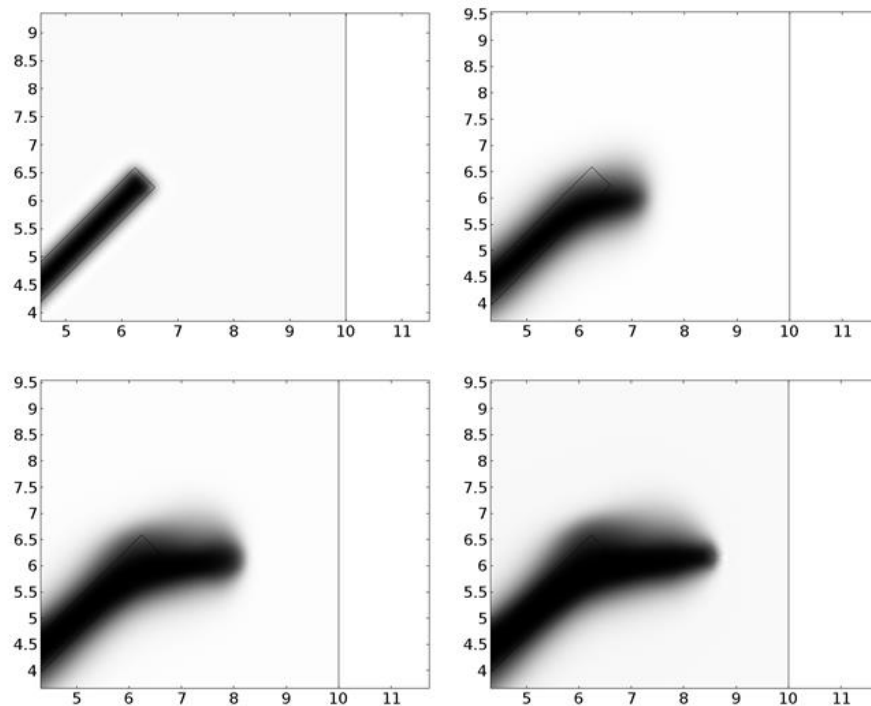


Figure 3-20 Magnified view of crack propagation. The snapshots are taken at time step 0,

75, 76 and 84 where the time step interval $\Delta t = 0.001s$. $\gamma = 200 \text{ J/m}^2$. $E = 5.8 \text{ Mpa}$.

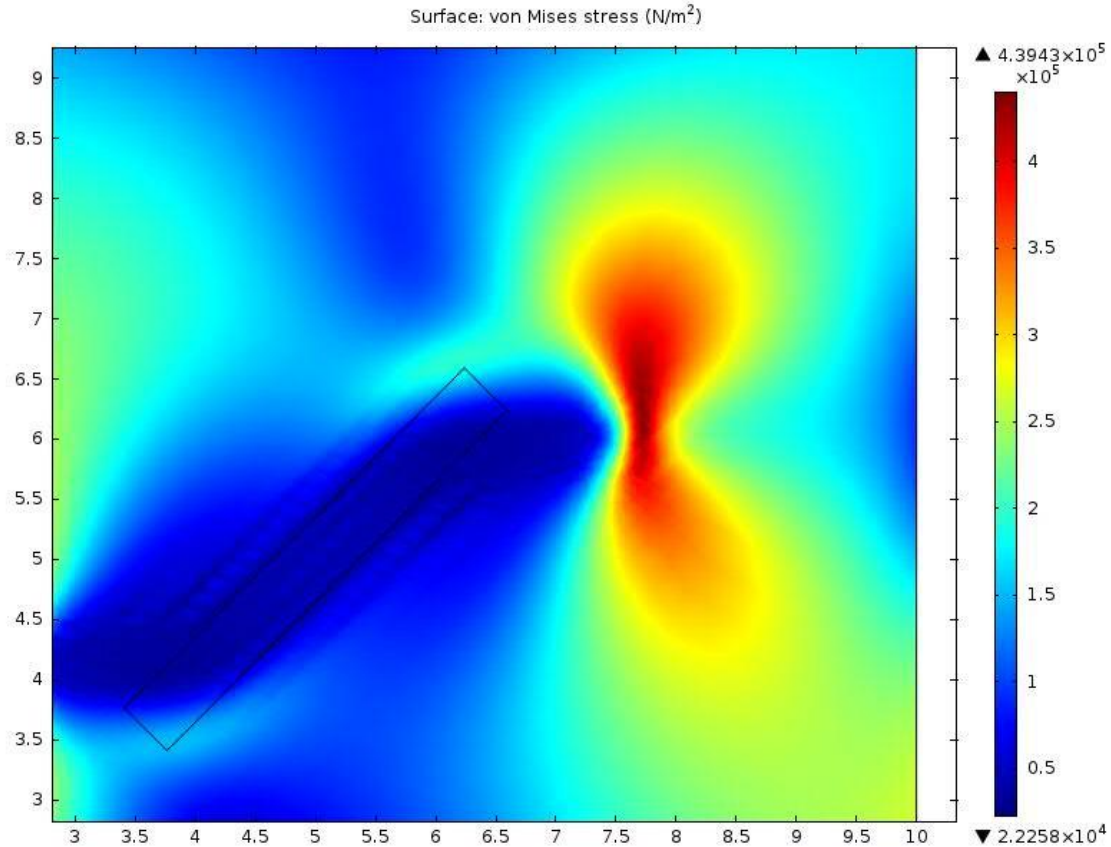


Figure 3-21 von Mises stress distribution at t=0.076s

3.4.3 Cracking experiments and comparisons

In order to verify our PFM simulation, the cracking experiments are conducted to find out reasonable fracture properties and to provide benchmarks. The Direct Tension Tester (DTT) machine of Interlaken Technology Corporation, as shown in Figure 3-22, is the main instrument used for testing. By inputting certain commands, pure tension loading in the forms of either tensile force or displacement can be applied by the machine.

Figure 3-23 shows the original and modified geometry of the asphalt binder specimen. The thickness is 6mm. The specimen is prepared in an aluminum mold, and glycerin mixture is

brushed on the mold surface to prevent asphalt binder from sticking onto the mold. Two plastic ends are attached to the specimen so that the specimen can be put in the Direct Tension Tester. By inserting an aluminum sheet so as to simulate an initial crack in the asphalt specimen, we can conduct the corresponding mixed-mode cracking experiments. To simulate the crack in winter, the specimen is put in the environmental chamber and the testing temperature is set as -20°C using the Julabo cooling system.



Figure 3-22 The direction tension tester by Interlaken Technology Corporation

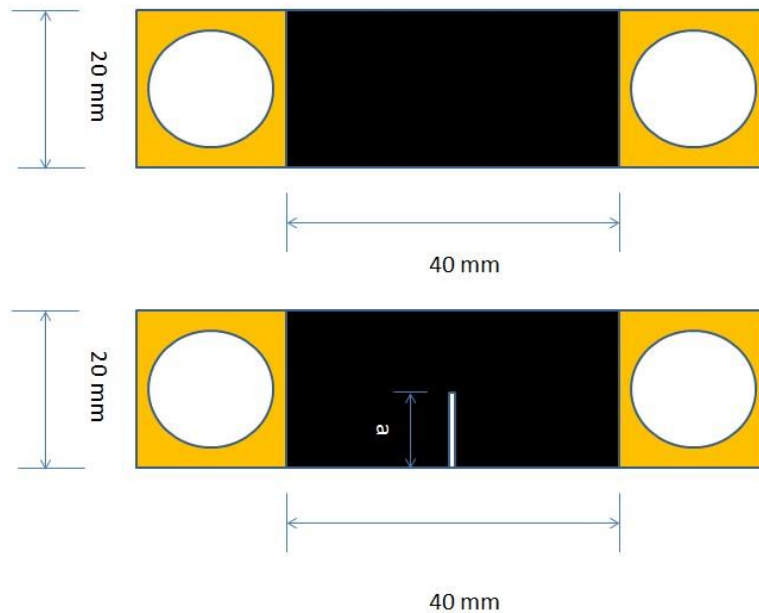


Figure 3-23 Geometry of standard asphalt binder specimen on DTT and the modified specimen by inserting aluminum sheet as the initial crack in Mode I cracking simulation

The right end of the testing specimen is then fixed on the DTT machine, and a tensile force that increases with time is applied on the left end. Both the force and the corresponding displacement on the left end are recorded in the computer throughout the experiment. Note that $-20\text{ }^{\circ}\text{C}$ falls below the glass transition temperature of asphalt in our lab, the asphalt becomes very brittle and fails very quickly, the specimen will suddenly break apart when the tensile stress (or equivalently tensile force) reaches a critical value. Thus we consider the stress that initiates the crack is the critical failure stress.

We first investigate the pure Mode I and Mode II fracture toughness (K_{IC} & K_{IIC}) of our asphalt binder since they are relevant to the mixed mode fracture energy in our phase-field model, which reflects the maximum fracture resistance. Note the Mode I fracture energy $G_I = 237.32\text{ J/m}^2$ obtained in the Mode I cracking section is employed here.

For the Mode II fracture toughness of asphalt binder, there is no current research data or reference regarding it and we are not able to test the value due to instrument limitation. In this way, we present the possible values and calculate the corresponding Mode II fracture energy.

In the mixed mode phase-field model, the crack begins to propagate when

$$J \geq G_{total} \quad (3-48)$$

where the mixed mode fracture energy G_{total} is very complex and based on the studied material, crack length, crack angle, loading condition and many other factors.

There are currently many models suggested to obtain the mixed mode fracture energy based on the specific mixity. Reeder (1992) suggest two criteria shown as [26]

$$G_I + G_{II} = G_{total} = G_{Ic} = G_{IIc} \quad (3-49)$$

and

$$\left(\frac{G_I}{G_{Ic}}\right)^\alpha + \left(\frac{G_{II}}{G_{IIc}}\right)^\beta = 1 \quad (3-50)$$

where α and β are the material responses which need to be determined by accurate experiment. Consider the limitation of our instrument, we simply employ equation (3-49) for simulation. The mixed mode fracture toughness under this assumption is not to be a function of mixed-mode ratio. Note that for pure mode I or mode II cracking, the mixed mode surface energy is pure mode I or mode II surface energy. Besides, note that the power law shown in equation (3-50) will have a better accuracy if the parameters α and β can be found by curve fitting through the experimental data, which is our next goal.

It should be mentioned that the fracture energy actually includes contributions from both the reversible surface energy and many irreversible processes such as plastic dissipation. In the phase-field theory, both contributions are combined into the surface energy or surface tension, i.e., $G = 2\gamma$. Based on these assumptions, the phase-field simulations can be conducted. We consider a stress that increases with time and select the stress value at the time instant when ϕ at the crack tip reaches -1 to be the critical stress. The corresponding mixed-mode cracking tests are also conducted. The specimen and the corresponding broken one are shown in Figure 3-24 (a) and (b), respectively. As can be seen, the initial crack angle is approximately 45° . The crack propagates in a direction almost vertical to the loading, which demonstrates that the crack path shown in Figure 3-20 is reasonable. The reason why it behaves in this manner is that the system has the maximum energy release rate in this direction. The same test is performed 10 times in order to minimize the random error during the cracking experiment.

The final average critical stress of mixed mode cracking experiment is 0.293 MPa. Based on the geometry from Figure 3-23, we can conduct the corresponding simulation and result shows that the critical load is 0.245 MPa using equation (3-49). Compare our simulation result with the experiment results, the relative error is 16.38%. The main reason why we have error is that the employment of equation (3-49) but not equation (3-50). It should be noted that the accurate determination of mixed-mode fracture energy will affect the prediction of critical fracture stress. Thus the next research target in this area should be focused on the determining this important material property through accurate experiment.

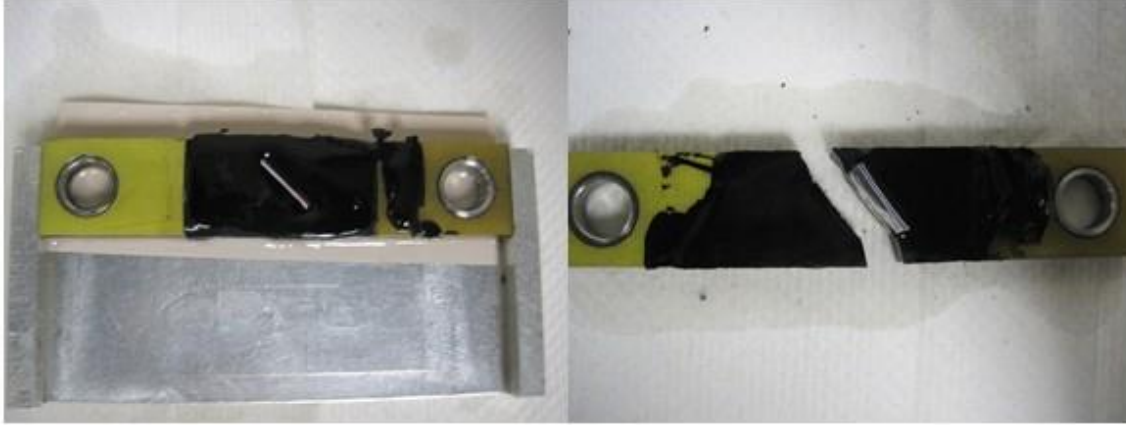


Figure 3-24 (a) The new made sample with crack length = 12 mm (b) broken sample after testing

3.4.4 Summary and conclusions

In this section, a non-conserved phase field model for mixed-mode cracking failure in asphalt binders at a low temperature is presented. Mixed mode cracking experiments of direct tension tests are conducted to verify the reasonable choice of fracture parameters of asphalt binder and the critical stress. The critical loading that leads to crack propagation in our simulation agrees well with the experimental result. Due to the extra dissipation associated with the phase-field equation, the critical stresses obtained in the simulations are always slightly greater than the experiment data. Compared with the classical fracture mechanics, the Phase-field model does not need to explicitly track the crack surface and can easily handle the typological changes. Theoretical analysis and experiment comparison show that it is capable of simulating the initiation of mixed mode fracture in asphalt binder. Therefore, the phase field method presents a promising and innovative method for modeling the low-temperature mixed mode cracking of asphalt binder for better quantitative understanding of the binder behavior.

However, there are several aspects that are not covered by the current work and need to be further investigated:

- 1) In our current research, the cracking process is considered as linearly elastic since the corresponding experiment is performed at $-20\text{ }^{\circ}\text{C}$. In the near future we plan to study how the visco-elastic property will affect the asphalt cracking with the introduction of the cohesive zone at crack tip;
- 2) The accuracy of our experimental results is limited by the instrument. Our future plan is to determine the fracture energy obtained by equation (41) by using more accurate experiment methods. Besides, we are planning to expand our research area to the asphalt mixtures.
- 3) The numerical model presented in this paper needs an existing crack as the initial condition, which limit the applicability of Phase-field Method on the mixed mode fracture of asphalt binder. We are planning to expand the research to a broader situation which does not need an existing discontinuity.

3.5 Crack interaction

The current research of single mode cracking has achieved some satisfactory results but there still lacks relevant research when it comes to crack interaction. And thus the studying of such problem is urgent and realistic. In this section, the crack interaction will be studied by using Phase-field method.

3.5.1 Generalized Eshelby tensor and J - integral

Since we want to study crack interaction, we first assume that there exist a macro crack Γ_1 and an arbitrary very close micro crack Γ_2 as shown in Figure 3-25. According to the conservation law of J-integral, we have the following equation referring to Tian *et al.*'s conclusion [27]

$$J(\Gamma_\infty) + J(BC) + J(DE) + J(\Gamma_2) + J(ED) + J(\Gamma_1) + J(FA) = 0 \quad (3-51)$$

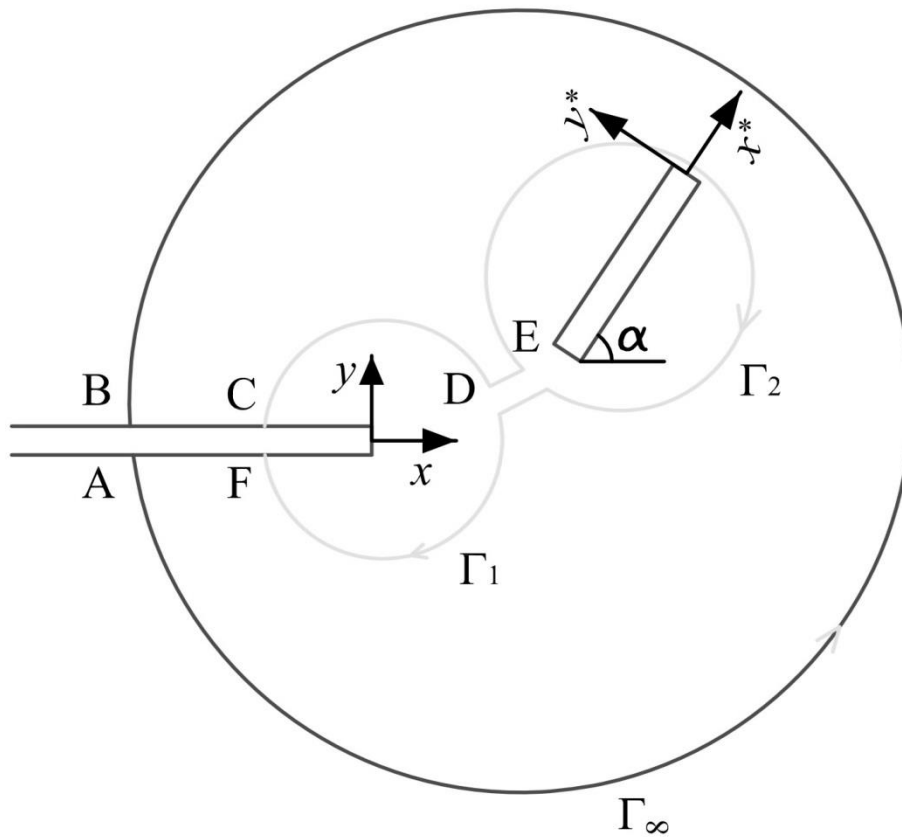


Figure 3-25 Crack contour in crack interaction

Note that integral over path DE is cancelled with the one on ED. Consider traction-free condition on the crack surfaces, we have $J(BC) = J(FA) = 0$ and thus equation (3-51) can be further derived as

$$J(\Gamma_\infty) + J(\Gamma_1) + J(\Gamma_2) \quad (3-52)$$

Where $J(\Gamma_\infty)$ is the J -integral from the remote stress field, $J(\Gamma_1)$ is the J -integral from the macro-crack tip and $J(\Gamma_2)$ is the J -integral from the micro-crack tip. Note that $J(\Gamma_2)$ is the J -integral effect from Γ_2 in the total overall system. For the local coordinate system x^*y^* , we have the following equation (3-53) based on the transformation of the two coordinate systems [28]

$$J(\Gamma_2) = J_1^* \cos\alpha - J_2^* \sin\alpha \quad (3-53)$$

where $J_1^* = \oint_{\Gamma_2} (f_{el} dy^* - T_i^* u_{i,1}^* dl)$ and $J_2^* = \oint_{\Gamma_2} (-f_{el} dy^* - T_i^* u_{i,2}^* dl)$

in which T_i^* is the projection of the traction in the local coordinates system x^*y^* .

Since the overall J -integral is expressed as the sum of two, we then study the criterion for cracking of $J(\Gamma_\infty)$ in phase field. Figure 3-25 is then simplified as shown in Figure 3-2 from the remote stress field. And as have been proved previously, the criterion for cracking is $J(\Gamma_\infty) \geq 2\gamma$. It is seen that our phase-field theory agrees with the Griffith's theory that crack propagates when $J(\Gamma_\infty)$ in the remote stress field is large enough to created two new surfaces.

3.5.2 Numerical simulation

A two-dimensional finite element model is established in COMSOL for the fracture analysis under tension loading. A fixed Eulerian mesh is used to describe the internal interfaces between

the intact solid and crack void. The mesh refines adaptively at the interface, as shown in Figure 3-26, to resolve the ϕ profile across the interface.

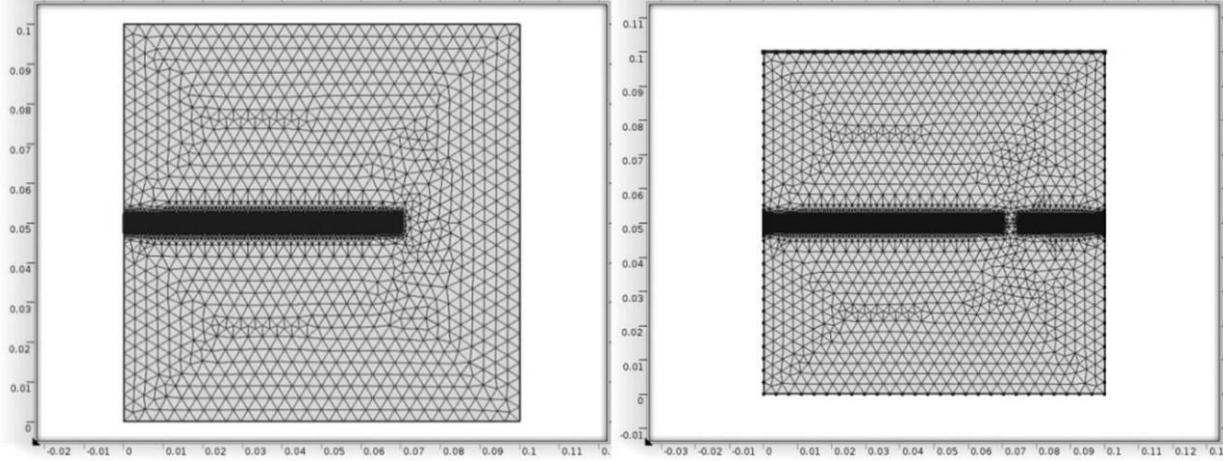


Figure 3-26 (a) Unstructured triangular mesh generated by COMSOL with one initial crack (b) Mesh with two initial cracks

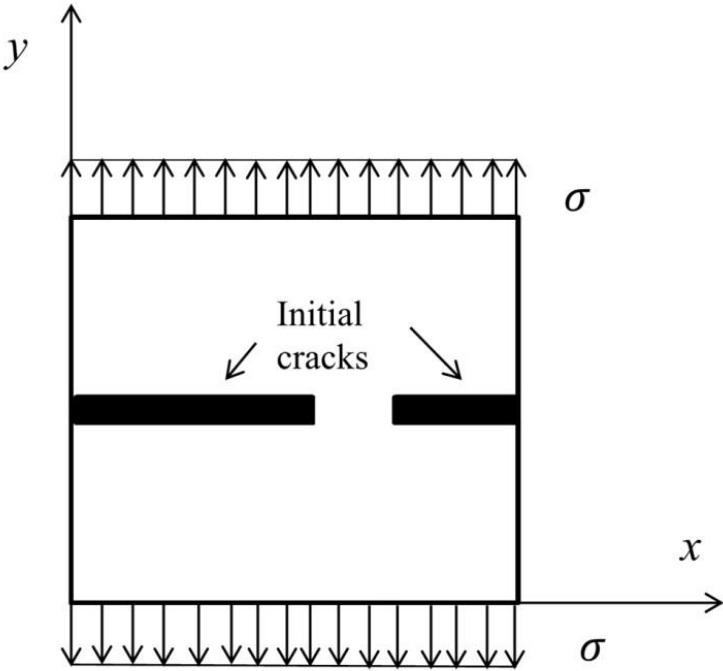


Figure 3-27 Pure tension loading is applied on our model

We consider plane strain and the computational domain is a square with side length $L = 0.1$ m. We choose the interfacial thickness $\epsilon = 0.0025$ m and the initial macro-crack length 0.07 m and the initial micro-crack length 0.025 m. For simplicity, two cracks are set as pure Mode I as shown in Figure 3-27. Because of the diffuse nature of the phase-field method, we need to impose a finite crack width, which we use $W = 0.005$ m in this simulation. The finest mesh size is set to be $\Delta x = \frac{1}{33}W$ (i.e., $\epsilon \approx 6.6\Delta x$).

Figure 3-27 shows that pure tension loading is applied on top and bottom boundaries. For convenience we set the bottom boundary as fixed in our simulation. The loading condition is set as $\sigma(t) = \frac{\sigma_0}{t_0} \cdot t$ where $\frac{\sigma_0}{t_0} = 2 \times 10^5 \frac{\text{N}}{\text{m}^2\text{s}}$ in our simulation.

The comparison between the single crack propagation and crack interaction at different time instants are shown in Figure 3-28. The snapshots are taken at time step = 0, 0.08 s and 0.083 s respectively. $\gamma = 368 \text{ J/m}^2$. $E = 5.8 \text{ Mpa}$. It can be clearly seen that crack propagates along the x-direction while there is a diffuse interface between the crack phase and the intact phase. Notice that at the same time, the single same macro crack without micro crack does not propagate which demonstrate that crack interaction does more easily tends to fail due to higher J -integral value at the propagating crack tip.

The critical load for the single Mode I macro cracking is calculated as 0.0160 MPa based on the classic fracture mechanics [9, 22], we can see that external load that causes crack interaction in Figure 3-28 does not reach the critical load for single Mode I crack case. If we pick the load value at the time instant when ϕ at the crack tip reaches -1 to be the critical load in phase field, the critical stress for Mode I is 0.0204 MPa and 0.0162 MPa for crack interaction.

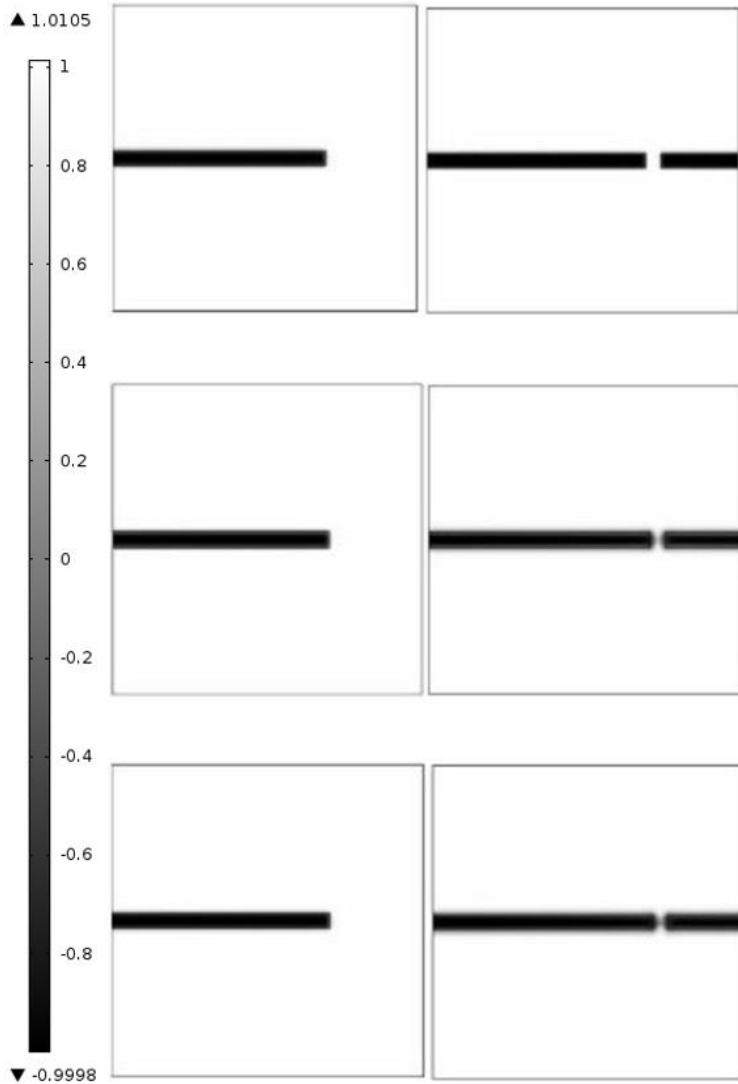


Figure 3-28 Crack interaction at different time instants

As expected, there is a stress concentration at the crack tip, as shown in Figure 3-29. In the region near the crack tip, the von Mises stress is much larger than that in the intact regions in front of the crack. Immediately above and below the crack, the stress is much lower than the average (1.7×10^4 Pa), since the elastic energy has been released to create new fracture surface area. This observation is in agreement with the classical fracture mechanics.

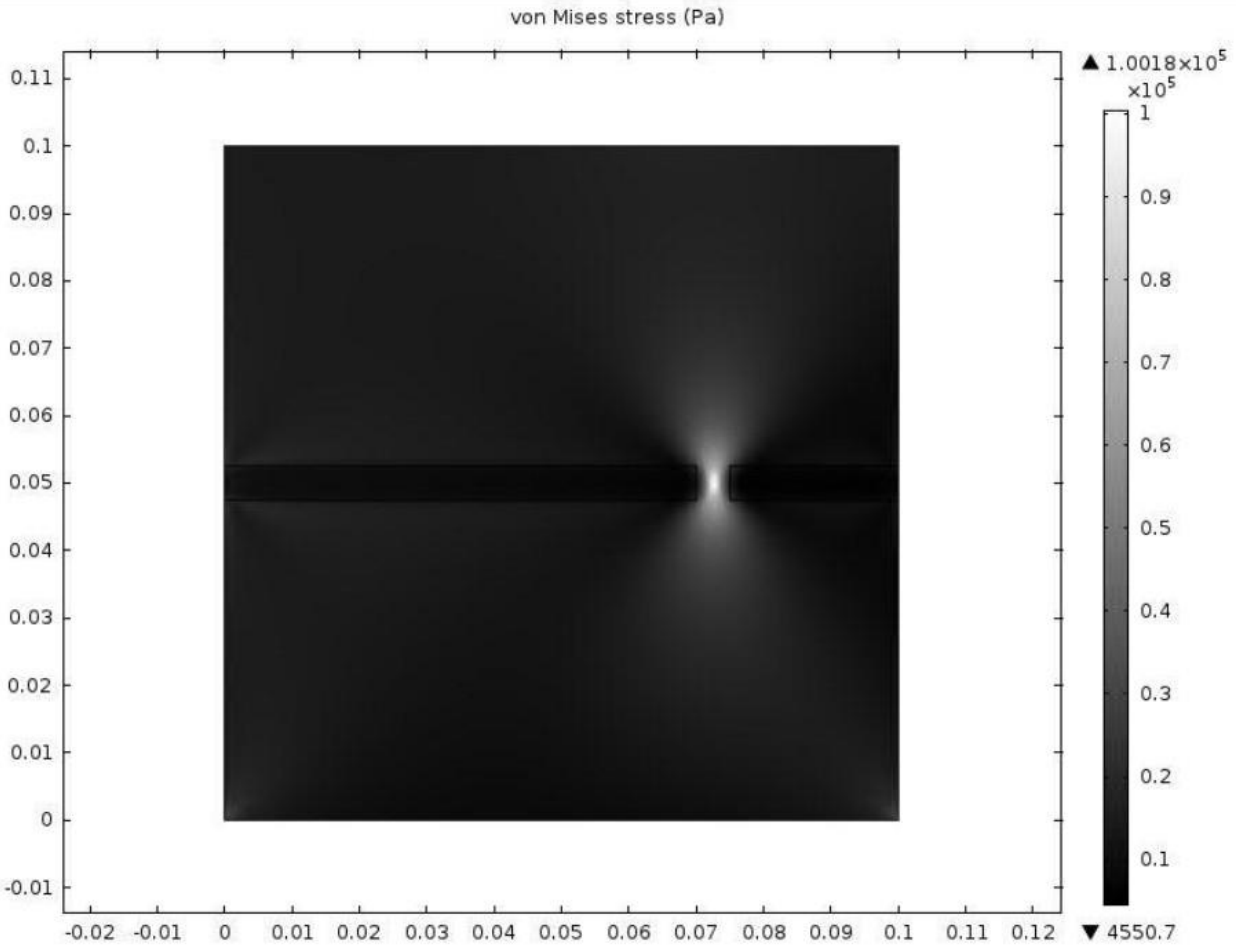


Figure 3-29 von Mises stress distribution

3.5.3 Experiments and comparisons

In order to verify the simulation results in PFM for crack interaction, we conducted experiments to provide benchmarks on the Direct Tension Tester (DTT) of Interlaken Technology Corporation with the Julabo cooling system. Figure 3-30 shows the geometry of an asphalt binder specimen and the thickness is 6mm. The specimen is prepared in an aluminum mold, and glycerin mixture is brushed on the mold surface to prevent asphalt binder from sticking onto the mold. Two plastic ends are attached to the specimen so that the specimen can be put in the Direct

Tension Tester. Two initial cracks are simulated by inserting thin aluminum sheets in the specimen. The initial crack length $a = 5$ mm is fixed and $b = 5$ mm and 10 mm. The relative positions of the two cracks are shown in Figure 3-30. The crack angle is set as three situations: $0^\circ, 45^\circ, 90^\circ$, corresponding to each b length. The specimen is then put in an environmental chamber that will keep the temperature at -20°C using the Julabo cooling system.

The asphalt binder specimen is fixed on the right end, and a tensile force that increases with time is applied on the left end at a rate of 10 N/s. Both the force and the corresponding displacement on the left end are recorded in the computer throughout the experiment. At -20°C , the specimen will suddenly break apart when the tensile load reaches a critical value.

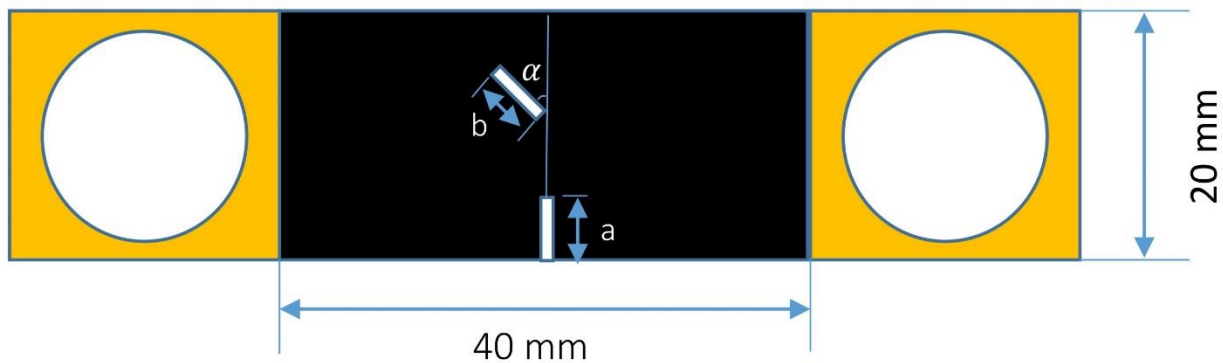


Figure 3-30 Geometry of asphalt binder specimen for crack testing

In order to reduce the random errors, 10 specimens are prepared for each crack length b and each crack angle α . The direct tension test is conducted on all the specimens, and the average critical load is selected as the representative value. Figure 3-31 shows the broken asphalt specimen after crack interaction experiment of $a = 5$ mm vs $b = 5$ mm in a crack angle $= 90^\circ$.

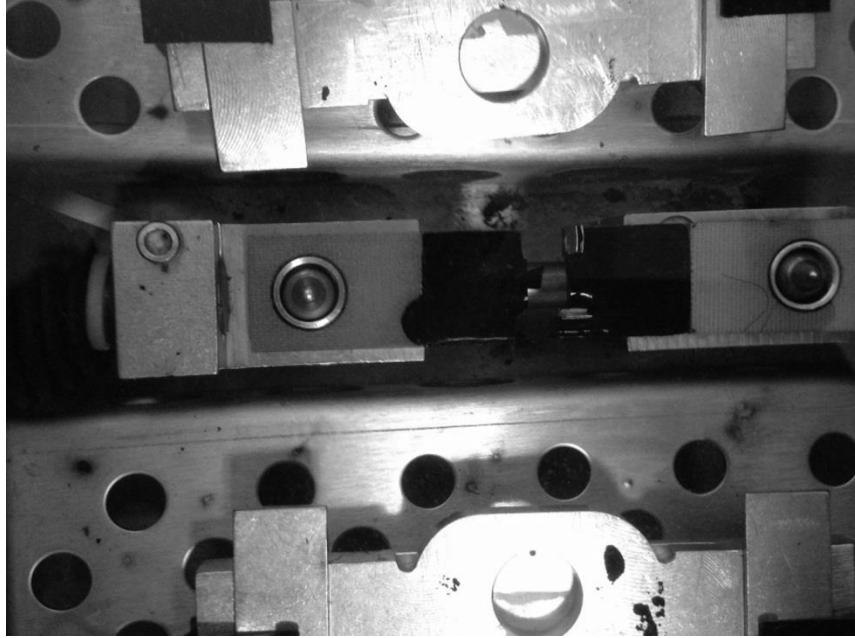


Figure 3-31 The broken specimen after tension loading

The comparison between comparisons between experiment results and PFM model calculations are shown in Table 3-3.

It is seen that our PFM results have a good agreement with the experimental result (relative error 20.1%, 13.3%, 24.0%, 17.2%, 24.1% and 20.1%, respectively). The maximum critical load occurs when the crack angle is 45° in each crack interaction lengths group. Our results matches the simulation results by Lam *et al.*'s work (1991) that the maximum critical load happens at the crack angle $\theta = 45^\circ$ in the testing three crack angles [29].

Table 3-3 Comparison between experiment and PFM

Critical load (MPa)	Crack interaction 5 mm vs 5 mm			Crack interaction 5 mm vs 10 mm		
	Crack angle (°)			Crack angle (°)		
	0	45	90	0	45	90
	0.254	0.30	0.270	0.239	0.266	0.254
PFM (MPa)	0.305	0.34	0.335	0.28	0.33	0.305

3.5.4 Summary

In this section, we present a non-conserved phase field model for fracture failure in crack interaction of asphalt binders at a low temperature. Tests on the direct tension specimen are conducted to verify the corresponding cracking simulation results. The critical loadings that lead to crack propagation agree well with those predicted using Phase Field Model. Overall, compared with the classic fracture mechanics, the Phase-field model does not need to explicitly treat the crack surface and can easily handle the topological changes. It is capable of simulating fast fracture failure in crack interaction of asphalt binder with reasonable accuracy, which will lead to a better quantitative understanding of the binder behavior.

However, there are still several aspects that are not covered by the current work and need further investigation. For example, in the real cracking process, the temperature may be much higher than -20°C and asphalt binder may not be linearly elastic; the asphalt mixture, which is a mixture of asphalts and other materials, may exhibit non-homogenous properties. All these issues will be addressed in our future work.

REFERENCES

- [1] Peterson, C., Buttlar, W. and Braham, A. (2009). "Mixed-mode cracking in asphalt concrete." *Advanced Testing and Characterization of Bituminous Materials*, 2, 785-795.
- [2] Dave, E., Song, S., Buttlar, W. and Paulino, G. (2007) "Reflective and thermal cracking modeling of asphalt concrete overlays." *Advanced Testing and Characterization of Bituminous Materials*, 2, 1241-1252.
- [3] Anderson, D., Christensen, D., Bahia, H., Sharma, M., Antle, C. and Button, J. (1994). *Binder Characterization and Evaluation*. Strategic Highway Research Program (SHRP) A-369, National Research Council.
- [4] American Society for Testing and Materials E 399-90: Standard Test Method for Plane-Strain Fracture Toughness of Metallic Materials. Annual Book of ASTM Standards, 03.01, ASTM, Philadelphia, Pennsylvania, 1990, 413-443.
- [5] Ponniah, J., Cullen, R., Hesp, S. (1996). "Fracture energy specifications for modified asphalts." *Proceedings in ACS Division of Fuel Chemistry*, 4(41), 1317-1321.
- [6] Hoare, T., and Hesp, S. (2000). "Low temperature fracture testing of asphalt binders." In *Transportation Research Record: Journal of the Transportation Research Board*, No. 1728, Transportation Research Board of the National Academies, Washington, D.C., 36-42.
- [7] Hesp, S. *Development of a fracture mechanics-based asphalt binder test method for low temperature performance prediction*. National Cooperative Highway Research Program's

Innovations Deserving Exploratory Analysis (NCHRP-IDEA) Program Project 84 Final Report, 2004.

[8] Griffith, A. (1921). "The phenomena of rupture and flow in solids." *Philosophical Transactions of the Royal Society of London, Seria A*, 22, 163-197.

[9] Karma, A., Kessler, D. and Levine, H. (2001). "Phase-field model of mode III dynamic fracture." *Physical Review Letter*, 87, 045501.

[10] Henry, H. and Levine, H. (2004). "Dynamic instabilities of fracture under biaxial strain using a phase-field model." *Physical Review Letter*, 93(10), 105504.

[11] Eastgate, L., Sethna, J., Rauscher, M., Cretegny, T., Chen, C. and Myers, C. (2002). "Fracture in mode I using a conserved phase-field model." *Physical review E*, 65, 036117.

[12] Kuhn, C., and Muller, R. (2010). "A continuum phase field model for fracture." *Engineering Fracture Mechanics*, 77, 3625-3634.

[13] Schanzel, L., Hofacker, M. and Mieche, C. (2011). "Phase field modeling of crack propagation at large strains with application to rubbery polymers." *Proceedings in Applied Mathematics and Mechanics*, 11, 429-430.

[14] Song, Y., Soh, A. and Ni, Y. (2007). "Phase field simulation of crack tip domain switching in ferroelectrics." *Journal of Physics D: Applied Physics*, 40, 1175-1182.

[15] Yue, P., Zhou, C. and Feng, J. (2010). "Sharp-interface limit of the Cahn-Hilliard model for moving contact lines." *Journal of Fluid Mechanics*, 645, 279-294.

- [16] Yue, P., Zhou, C., Feng, J., Ollivier-Gooch, C. and Hu, H. (2006). "Phase-field simulation of interfacial dynamics in viscoelastic fluids using finite elements with adaptive meshing." *Journal of Computational Physics*, 219, 47-67.
- [17] Harvey, J. and Cebon, D. (2005). "Fracture tests on bitumen films." *Journal of Materials in Civil Engineering*, 17, 99-106.
- [18] Wise, S., Lowengrub, J., Frieboes, H. and Cristini, V. (2008). "Three-dimensional multispecies nonlinear tumor growth - I. Model and numerical method." *Journal of Theoretical Biology*, 255, 257-274.
- [19] Kim, J. and Paulino G. (2003). "Mixed-mode J-integral formulation and implementation using graded elements for fracture analysis of nonhomogeneous orthotropic materials." *Mechanics of Materials*, 35, 107-128.
- [20] Rice, J. (1968). "A path independent integral and approximate analysis of strain concentration by notches and cracks." *Journal of Applied Mechanics*, 35, 379 - 86.
- [21] Yue, P., Feng, J., Liu, C. and Shen, J. (2004). "A diffuse-interface method for simulating two-phase flows of complex fluids." *Journal of Fluid Mechanics*, 515, 293-317.
- [22] Spatschek, R., Muller-Gugenberger, C., Brener, E. and Nestler, B. (2007). "Phase field modeling of fracture and stress-induced phase transitions." *Physical Review E*, Vol. 75, 06611.
- [23] Gross, D., and Seelig, T. (2006). *Fracture Mechanics with an introduction to micromechanics*. Springer, New York.

- [24] Braham A., Buttlar W., “Mode II cracking in asphalt concrete”, *Advanced Testing and Characterization of Bituminous Materials*, Vol. 2, 2009, p. 699-706.
- [25] Braham A., Buttlar W., Ni, FJ. “Laboratory Mixed-Mode Cracking of Asphalt Concrete Using the Single-Edge Notch Beam”, *Road Materials and Pavement Design*, 11:4, 2010, p. 947-968.
- [26] Reeder JR., NASA technical memorandum 104210: an evaluation of mixed-mode delamination failure criteria, National Aeronautics and Space Administration, Langley Research Center, Hampton, Virginia 23665, 1992.
- [27] Tian W., Chau K. and Chen Y. 2001. “J-integral analysis of the interaction between an interface crack and parallel subinterface cracks in dissimilar anisotropic materials”, *International Journal of Fracture*, 111:305-325.
- [28] Zhao L., Chen Y. 1996. “The J integral analysis of an interface main crack interacting with near tip subinterface microcracks”, *International Journal of Fracture*, 80:25-30.
- [29] Lam K.Y., Phua S.P. 1991. “Multiple crack interaction and its effect on stress intensity factor”, *Engineering Fracture Mechanics*, **40**:585-592.

Chapter 4. Investigation of Asphalt Self-healing Mechanism Using Phase-field Model¹

4.1 Introduction

The asphalt self-healing phenomenon has always been a challenging issue for pavement engineers due to the internal very complex chemical and physical mechanism. In the past decades, researchers have proposed many approaches to understand the asphalt healing mechanism and have made significant progress in this area. Bommavaram *et al.* (2009) employed the Wetting Distribution Function as the basic mathematical model to describe the wetting of two surfaces of a nano-crack and conducted corresponding experiment to determine the parameters in his controlling equation [1]. Qiu *et al.* (2011) used the Dynamic Shear Rheometer to investigate the self-healing behavior of pure asphalt [2]. Liu *et al.* (2011) found that the self-healing rate of asphalt mastic and porous asphalt concrete can be increased by induction heating [3]. Garcia (2011) discovered that once a crack is formed in the asphalt pavement, it starts healing and even can heal 100% if given enough time [4]. And, since self-healing means the diffusion of molecules at the molecular level, the Molecular Dynamic (MD) simulation can be employed to investigate the internal mechanism. Bhasin *et al.* (2011) used MD

¹ Part of this chapter is published as journal paper.

Hou, Y., Wang, L., Pauli, T., and Sun, W. (2014). "An Investigation of Asphalt Self-healing Mechanism Using Phase-field Model." *Journal of Materials in Civil Engineering*. 10.1061/(ASCE)MT.1943-5533.0001047, in press, proofreading.

simulation to investigate the correlation of chain length and chain branching to self-diffusivity of asphalt molecules [5].

However, current research of asphalt self-healing mainly focuses on describing the “results and effects” and still lack clear experimental and theoretical explanations of the self-healing “process”. In general, there are two questions needed to be answered: how to understand the two inverse processes fracture and self-healing comprehensively from the microstructure view; why and how the initial crack in asphalt materials would propagate or heal itself. To investigate the two problems, we first use the Atomic Force Microscopy (AFM) to study the phase separation phenomenon of Strategic Highway Research Program (SHRP) asphalts [6] and then use Phase-field Model.

In this section, we try to provide answers to the two questions raised above. First, we will understand the relationship between healing and fracture from a material re-arrangement point of view by using the conserved Cahn-Hilliard model; second, we will study the cracking and self-healing of formed asphalt crack from a mechanical point of view by using the non-conserved Allen-Cahn model. Both of the two models are implemented in the finite element software COMSOL using the two-dimensional simulations and validate by the AFM results. The ultimate goal is to comprehensively simulate the asphalt self-healing using the Multi-phase-field Model in both of the material re-arrangement and the mechanical aspects.

4.2 Atomic Force Microscopy

In our research, asphalt microstructure is the key to understanding self-healing. Over the past two to three decades, many researchers conducted studies of asphalt microstructure by using Optical

Microscopy. Lu *et al.* (2006) employed optical microscopy to investigate the asphalt chemical compositions and structural characteristics [7]. Senra *et al.* (2009) applied it in analyzing the development of microstructure in waxy crude oils [8]. However, considering the limitation of optical microscopy due to the opacity of asphalt, the Atomic Force Microscopy (AFM) is used as an alternative advanced and comprehensive scanning technology to investigate the asphalt microstructure. In the AFM imaging process, an extremely fine probe tip is rastered across the sample surface, and various interactions between the tip and sample are measured and recorded electronically. The AFM technique does not rely on optical transparency, and the image resolution is not limited by the wavelength of light.

In our experiment, we consider the Wave-Mode AFM of SHRP [6] core asphalt (AAC and AAK) and chromatographic fractions based on these materials. Samples are each prepared as a uniform thin-film sample of well-defined thickness which is “developed” by a solvent spin casting technique. Samples are prepared as asphalt plus toluene solutions (1.0g sample per 10.0 mL toluene) which are spin cast onto glass slide substrates at rates of 400-1000 rpm (varied in increments of 100 rpm) using an International Crystal Laboratories Rotational Casting Roto-Film™ film maker. Uniform films are obtained by slowly depositing 2 μL of the solution, dispensed from a 25 μL syringe onto a spinning glass slide. The samples are stored in a nitrogen-purged dry box at room temperature prior to imaging. Sample film thicknesses are determined by refractive light measurements using a Filmetrics F20 instrument based on a pre-established method.

A Quesant Q-Scope 250 AFM equipped with a Peltier heating/cooling stage was used to image asphalt thin-film samples. All of the samples considered in this study were imaged in

Intermittent Contact (IC) mode. In WM-AFM, a cantilever is oscillated at its resonance frequency above and in IC with soft material surfaces such as polymers or asphalt. The oscillating cantilever dissipates energy as it interacts with features on the sample surface. In this mode of imaging, the instrument provides three different image types: phase-contrast image which is generated relative to the time delay between the cantilever driving and response oscillations as the probe encounters the sample; topography image which is relevant to the topography of the sample surface; and error images which is not employed in our analysis. Mikromasch brand NSC16 IC mode “non-contact” cantilevers were purchased directly from Quesant Instrument Co. The average nominal force constant for the cantilevers employed in these studies was reported by the manufacturer to be 40 N/m (nominal range of 25 to 60 N/m). The average resonant frequency of operation ranges between 155 to 170 kHz. The average amplitude of oscillation for a batch of cantilevers ranges between 0.1 and 0.3 Volts. The set point force is initially set by the instrument software, and is observed to be consistently -0.5 ± 0.2 Volts. Samples were typically imaged at a scan frequency of 1.0 Hz (0.75 Hz and 2.0 Hz scan rates were also used to scan samples in certain cases).

AFM thermal cycle imaging is employed as the experiment condition. Imaging of sample thin films is conducted by initially imaging samples at room temperature, then increasing the temperature by 3 °C increments. The sample is allowed to stabilize for 20 to 30 minutes and then capture images at that temperature. This process is repeated until a maximum temperature usually around 40 °C or 50 °C is attained. This process is then repeated in the reverse order, where the temperature is decreased by 3 °C, again allowing the sample to stabilize for 20 to 30 minutes, then imaging at each temperature until the sample reaches room. Throughout the whole process, intermittent-contact mode is used for all thermal cycled imaging. Precautions are taken

to minimize sample oxidation and water condensation on the film by purging a small fixture, which is installed around the sample, and AFM scanner head with argon. Figure 4-1, Figure 4-2 and Figure 4-3 show the AFM results of AAC-1-C5 sample at 19 °C, 25 °C, 28 °C; 31 °C, 34 °C, 37 °C; 40 °C, 43 °C, 46 °C in the thermal cycling. Figure 4-4 shows the AFM images of AAC-1-C5 at 40°C, 31°C and 21°C in the decreasing temperature process. The two images in each row are from the same AFM scan but different image-scan types. The image on the right is a topography scan where the one on the left phase contrast image. We can see the thermal conditions strongly affect the microstructure of asphalt thin-film samples. It is also noted that the bumble-bee structure [9] appears during the thermal cycling process. Especially, when temperature goes up the images tend to show a smooth microstructure; when temperature goes down, phase separation happens as shown in Figure 4-4. These bumble-bees structure appear in agreement with Kringos *et al.*'s research (2011) on SHRP Core asphalts AAA-1, AAB-1, AAC-1, AAD-1, AAF-1, AAG-1, AAK-1 and AAM-1 in the AFM images [10].

Some conclusions can be obtained based on our AFM results as follows: first, bees are paraffin wax micro single crystal lamellae that melt and crystallize at the surface of asphalt bitumen film surfaces. Second, it is currently unknown what wax looks like in the bulk asphalt, but it is established that wax is distributed throughout a film of asphalt. It is likely that wax crystals present in the bulk phase are comprised of smaller structures, more rounded and 3-dimensional. Wax could also be partially dissolved in the bulk asphalt. The term wax gel (network structure) has been proposed for the bulk phase. Third, asphaltenes are also thought to constitute discrete and partially phase separated species in asphalt. These structures are likely very small nano-aggregates 5-nm to 50-nm in diameter. We are convinced that bumble-bee structure only occurs when paraffin wax is in high enough concentration in asphalt, approximately greater than 1%. In

general, we believe that understanding the forming of such bumble-bee structure by phase separation is the key to understand the microstructure evolution mechanism of asphalt and especially, self-healing since the observed material re-arrangement will significantly change the asphalt mechanical property. One possibility must be excluded before we begin our analysis. That is the phase separation of the “bumble-bees” structure may be caused by surface tension effect but not a “bulk” effect. Kringos *et al.* (2010) conducted Small Angle Neutron Scattering (SANS) experiments by comparing the SANS response with surface and bulk models and proved that the phase-separation features observed on the asphalt sample’s surface are also present in the bulk [10]. We can also notice that our asphalt sample performs a two-phase morphology. Due to the very complex chemical components of asphalt, we are unable to tell the exact physical property and chemical potential of the two phases. However, it is reasonable to believe that the overall asphalt physical property is close to the separated phases properties.

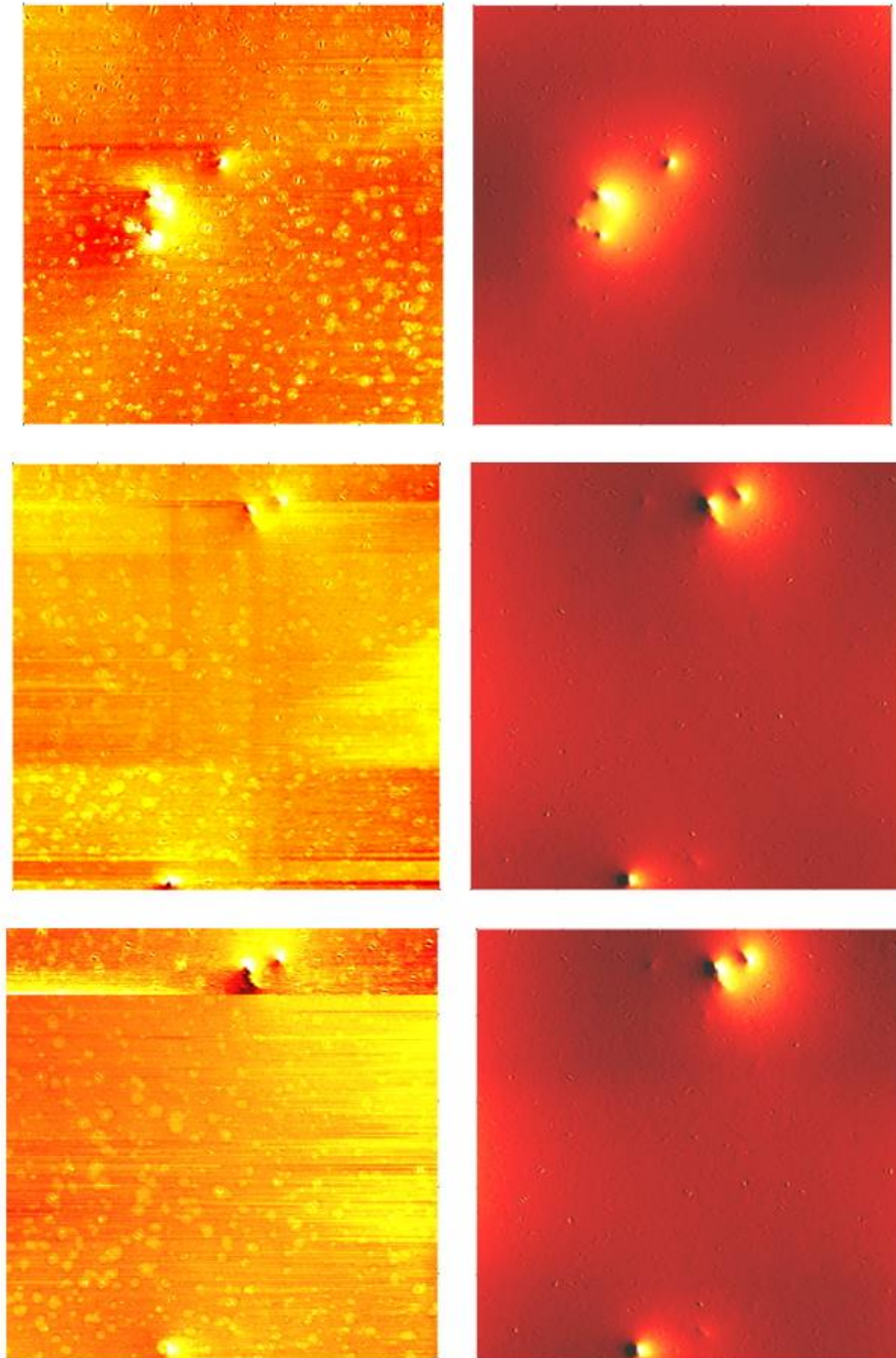


Figure 4-1 AFM images (l.h.s, phase contrast scans, r.h.s. topography scan) of AAC-1-C5 in a temperature increasing process at 19°C, 25°C and 28°C

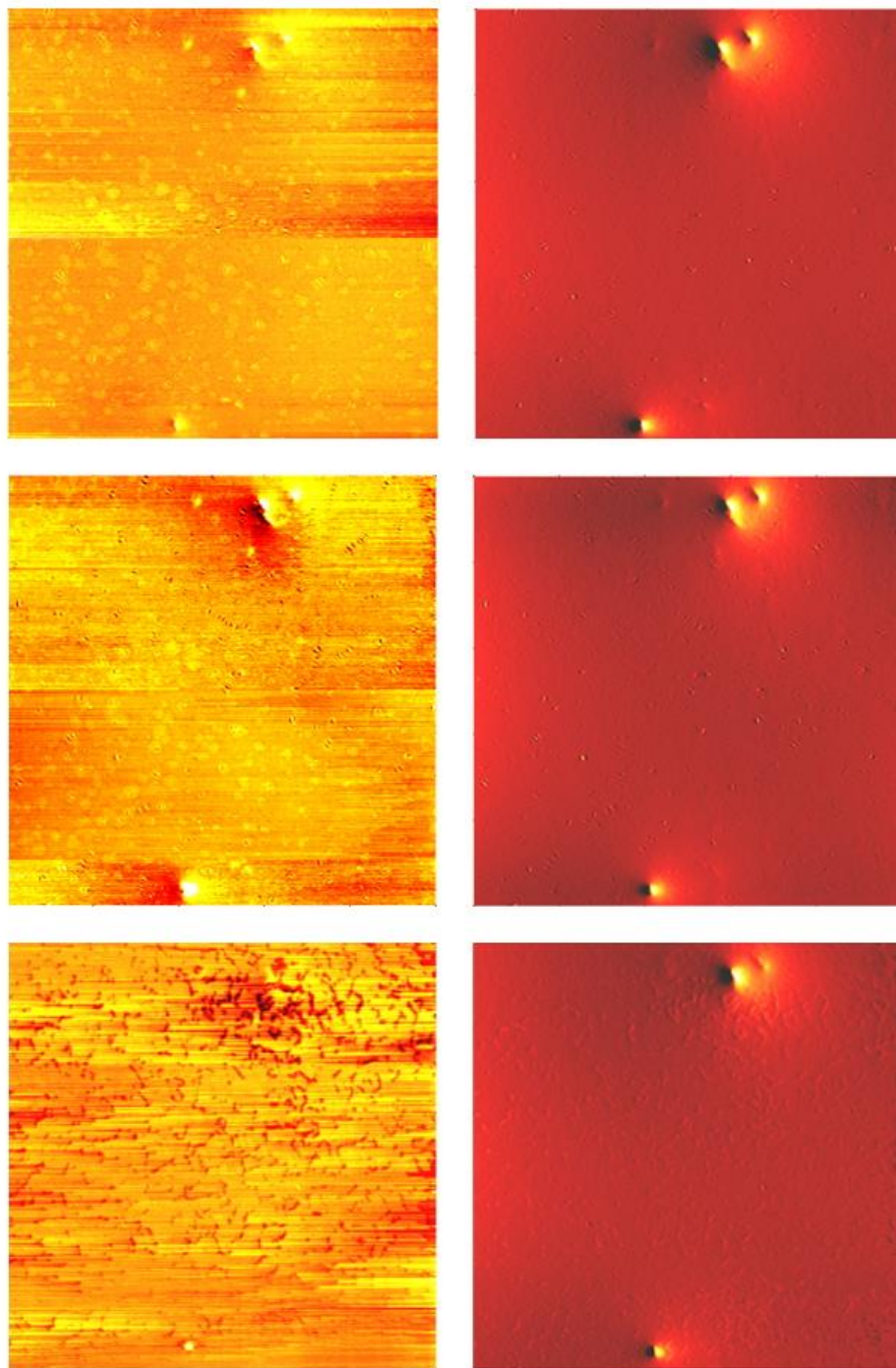


Figure 4-2 AFM images of AAC-1-C5 in a temperature increasing process at 31°C, 34°C and 37°C

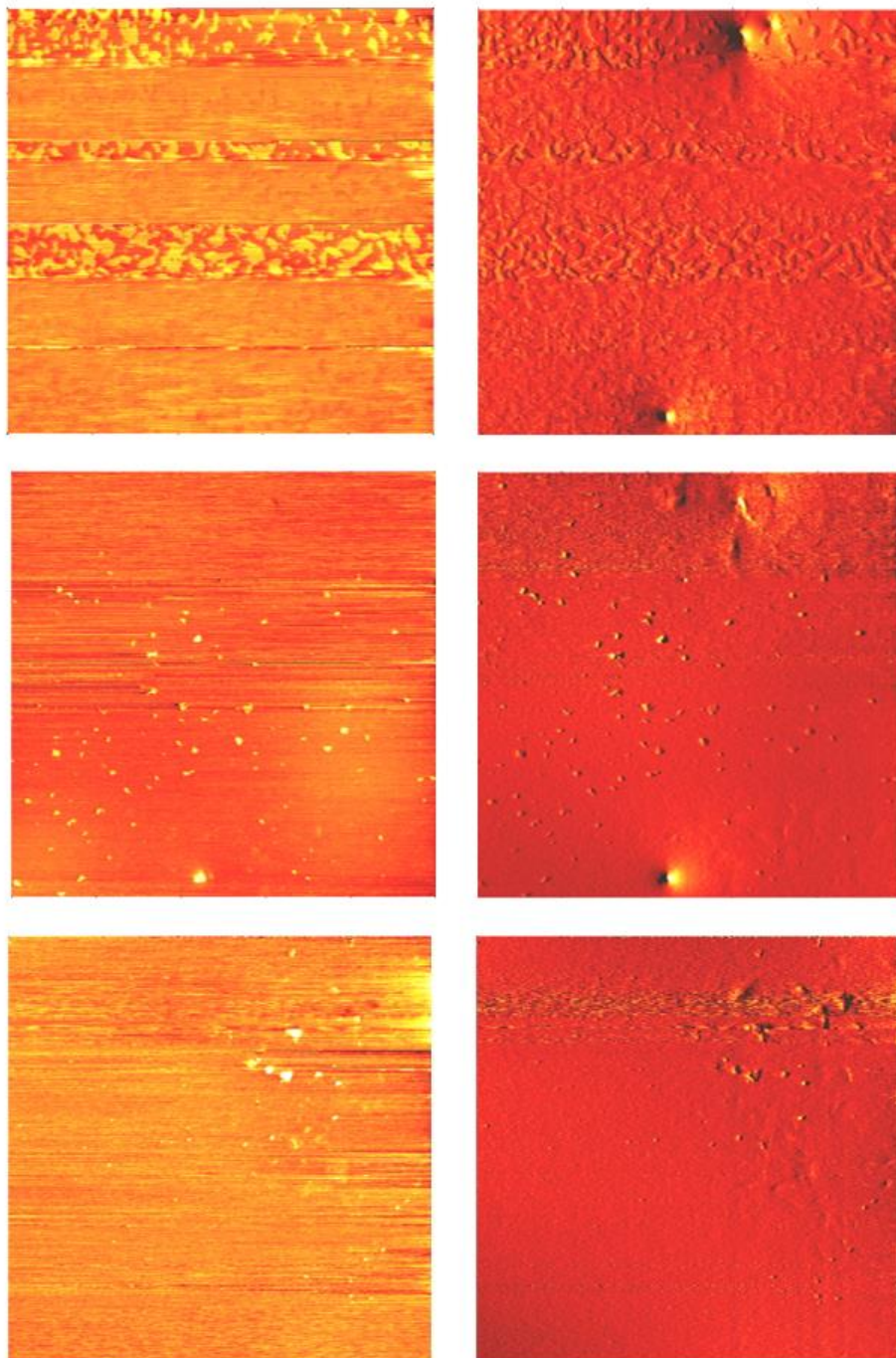


Figure 4-3 AFM images of AAC-1-C5 in a temperature increasing process at 40°C, 43°C, 46°C.

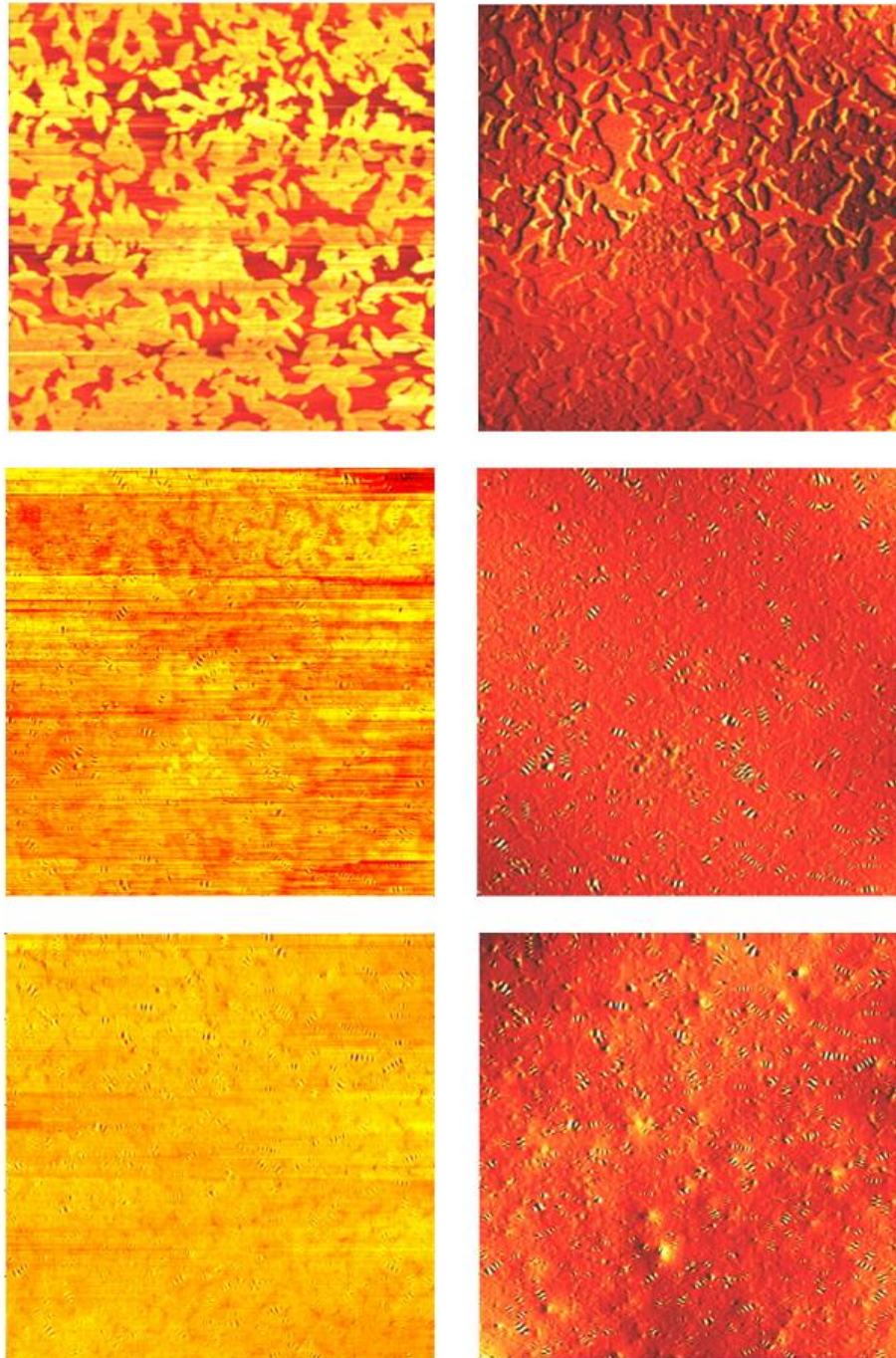


Figure 4-4 AFM images of AAC-1-C5 in a decreasing temperature at 40°C, 31°C and 21°C

4.3 Phase-field Model

As introduced in the beginning, we simulate asphalt self-healing using Phase-field model to answer the two raised questions using two different approaches.

4.3.1 *Material re-arrangement approach*

First we try to understand why asphalt will perform crack and self-healing from a microscopic view based on the AFM results as shown from Figure 4-1 to Figure 4-4.

4.3.1.1 Phase kinetics

It is observed that two phases get separation to reach the equilibrium state as shown in Figure 4-4 that the phase separation occurs in the cooling process and in the heating process, the two phases diffuse into each other and co-exists. In the classic thermodynamic theory, whether the co-existence of different phases occurs or not is dependent on the system free energy. Two types of free energy are used: Gibbs free energy (G) is also the chemical potential that is minimized when the studying system reaches equilibrium at constant pressure and constant temperature (**NPT**), and Helmholtz free energy is the thermodynamic potential in the studying system at constant temperature and constant volume (**NVT**).

Consider **NPT**, the evolution of the microstructure is determined by the Gibbs free energy and driven by the chemical potential (non-conserved case) or gradient of chemical potential (conserved case). A simple free energy model is the double well potential as shown in top figure of Figure 3-5 . The system has two metastable energy states ϕ_1 and ϕ_2 , which represent two different phases α_1 and α_2 , respectively. Note that the region under the negative curvature

between two spinodes A and B (where $\frac{\partial^2 G}{\partial \phi^2} = 0$) is unstable. Since a system always tends to reach a lower energy state, a homogenous mixture is unstable in this region and spinodal decomposition occurs. As a result, the mixed system spontaneously separates into the two co-existing phases (α_1 and α_2) In the region where $\frac{\partial^2 G}{\partial \phi^2} > 0$ the system remains metastable and phase separation does not happen unless the perturbation is large enough. The phase kinetic information can be intuitively codified into the phase diagram as shown in the bottom figure of Figure 4-5.

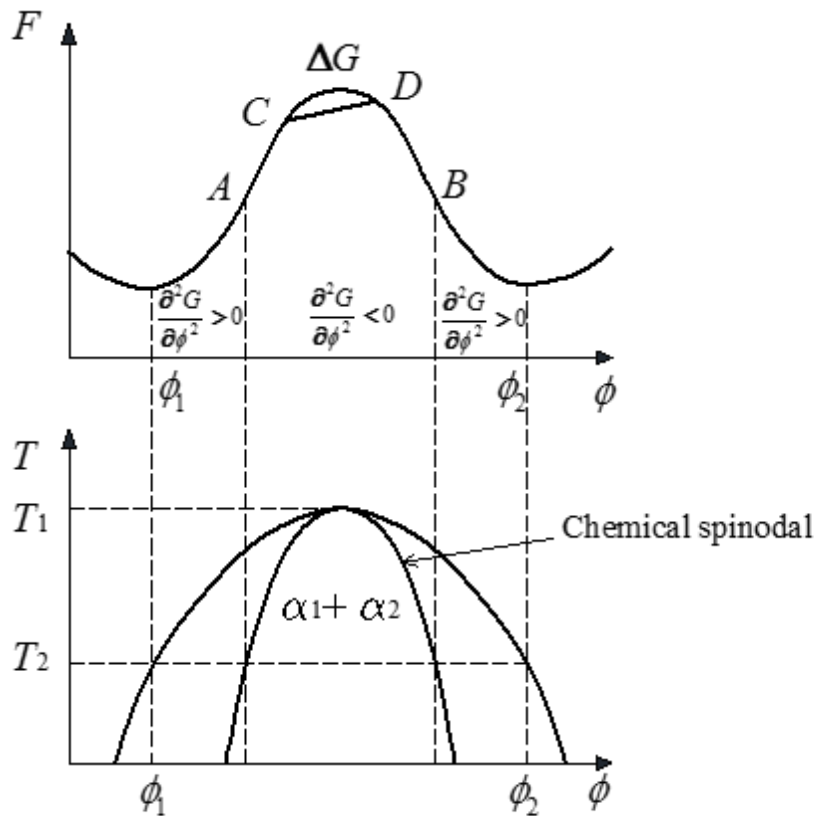


Figure 4-5 Schematic view of phase separation in terms of free energy and phase diagram

4.3.1.2 Mathematical model

Since there are two separated phases observed in the AFM results, we consider a Binary Phase-field Model including two different phases $\alpha_1(\phi = +1)$ and $\alpha_2(\phi = -1)$. The interface between the two phases is represented by the $\phi = 0$ level set. Note that equation (2-1) to equation (2-13) are all employed for numerical simulation.

4.3.1.3 Simulation of material re-arrangement

Based on phase-field model, we simulate a whole thermal cycling process. Note that the observance in AFM results can only demonstrate the existence of two phases but we are unaware of the exact physical property of the two in asphalt due to the instrument limitation. We are only convincing that the two phases should have different physical properties in elastic modulus, thermal expansion rate, etc. However, the assumption that the overall asphalt binder physical properties should be close to the two phases' properties is reasonable. By setting reasonable parameters, we implement a 2-dimensional model in the finite element software COMSOL to calculate the Phase-field governing equations as shown in Figure 2-1. An Eulerian mesh is used as shown in Figure 6. Six-node triangular elements (P2) are used in our finite element calculations. 15,284 elements are used in the initial mesh.

We consider the cooling process similar to our AFM experiment. Figure 4-6 shows the phases separation results at several time instants (left column) and the corresponding contours of von Mises stress (right column). Note that large von Mises stress gradient distributes along the interface between two different phases. It is easy to conclude that the diffuse interface has lowered the stress concentration than the sharp interface while in Figure 4-4 a sharp interface would have a larger stress concentration. Interestingly, Uehara (2011) also discovered that a high

equivalent stress distribution occurs at the interface [11]. Almost the same conclusions in different physical process demonstrate that stress concentration at interface is reasonable. We can also easily conclude that micro-cracks tend to happen in these stress concentration areas and further form bigger cracks. Suppose if there does not exist stress concentration near the interface, it is reasonable to conclude that the possible micro-cracks will disappear.

Besides, note that in the heating process of the thermal cycling, the patterns in AFM results tend to be more homogenous which implies a possible well-mixing of the two phases. And under this circumstance, double well potential will simply evolve to a convex function $f_{loc} = (\phi^2 - 1)$ [12] and the simulation results are shown in Figure 4-7.

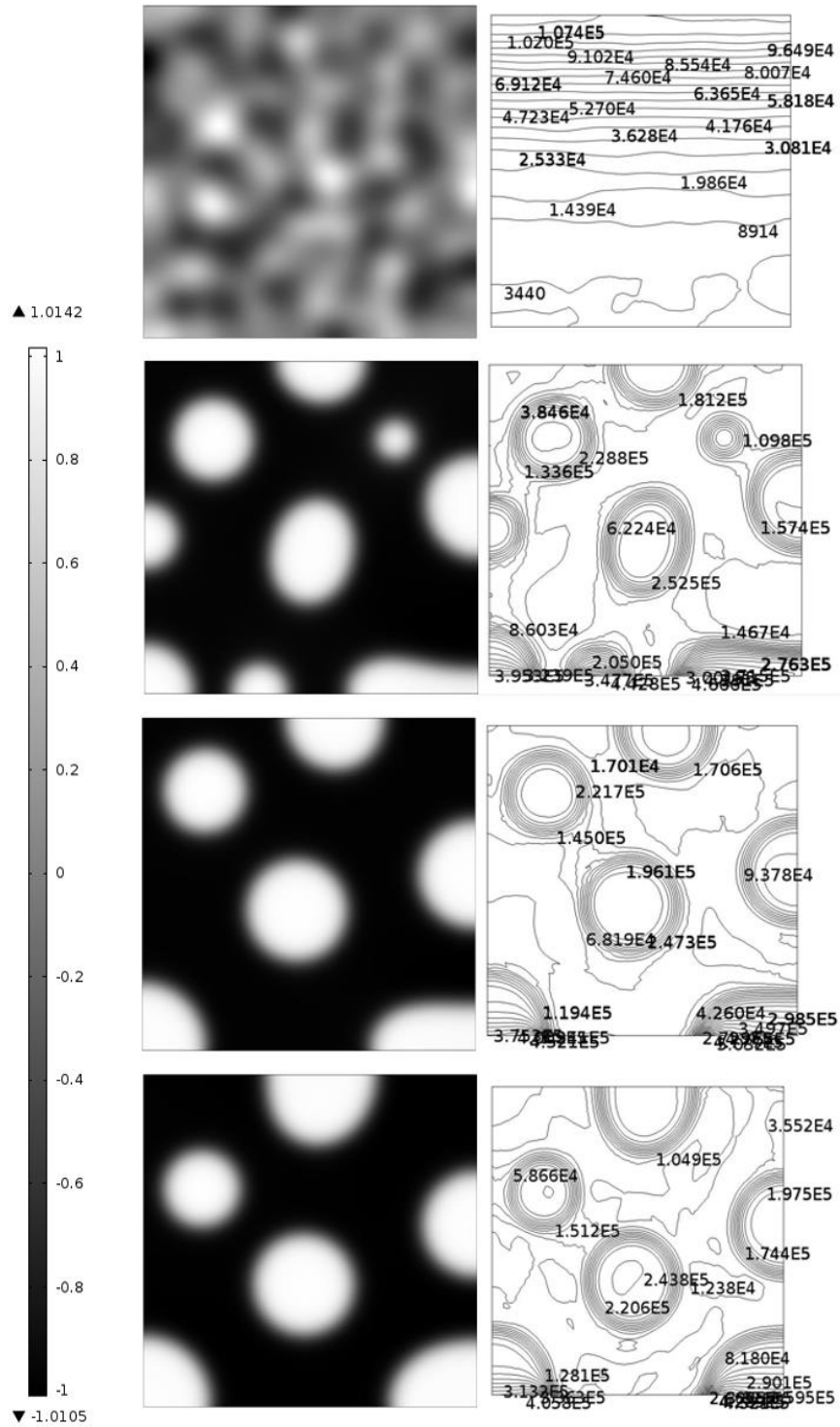


Figure 4-6 Phase separation during the temperature dropping process and the corresponding von Mises stress distribution contour plot

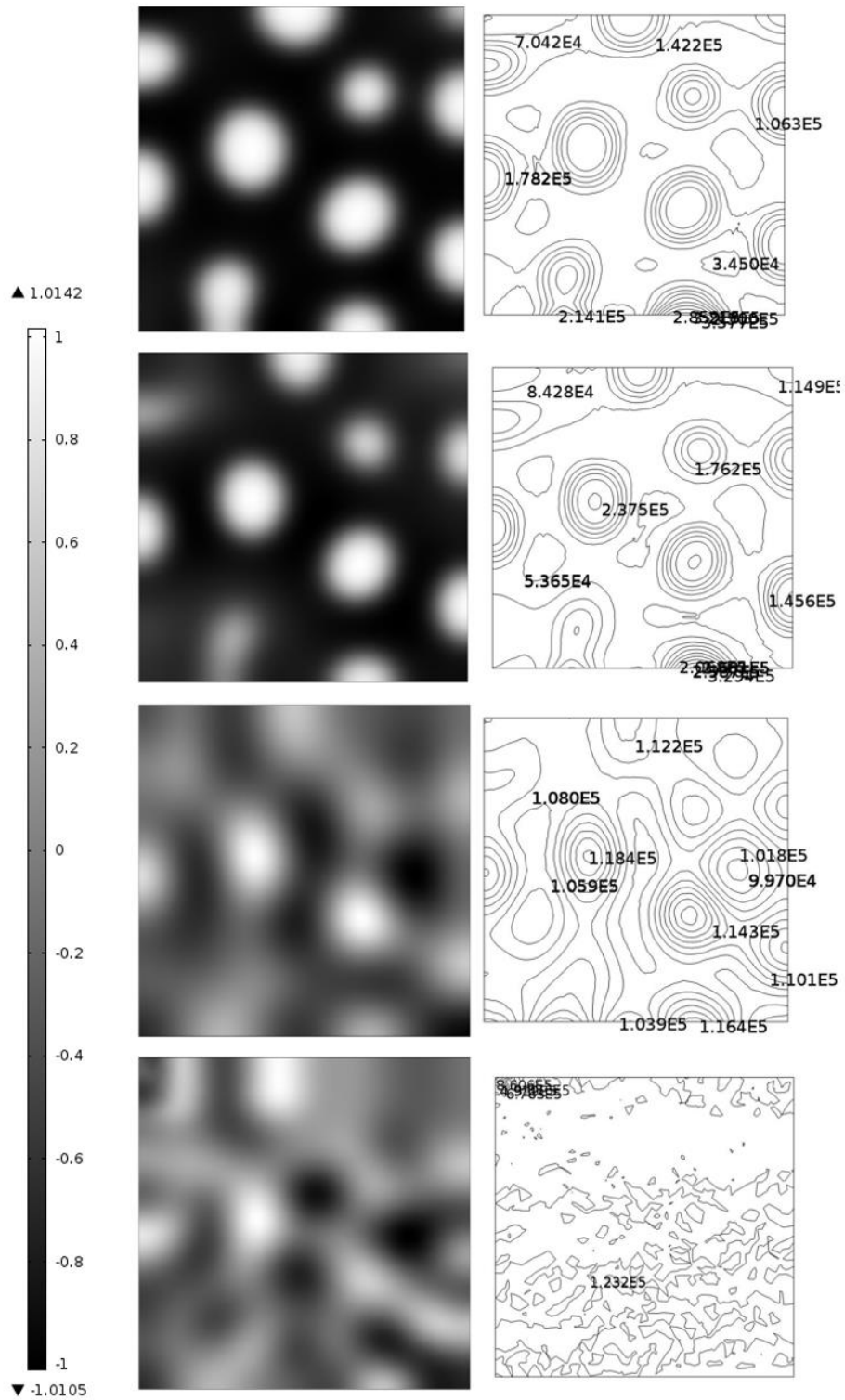


Figure 4-7 Phase mixing during the temperature rising process and the corresponding von

Mises stress contour plot

It is observed that in Figure 4-7, two separated phases get well mixed, the von Mises stress distribution becomes even and the initial high stress concentration zones disappear as the temperature increases. Based on the simulation results, we can conclude that possible micro-cracks disappear as temperature increases, which corresponds to self-healing of asphalt.

4.3.1.4 Comparison with AFM result

Compare Figure 4-4 and Figure 4-7, it is noted that both two illustrate the phase separation phenomenon. However, why the bumble-bee structure does not show in our simulation is because these bees are the crystallization of paraffin wax micro single crystal lamellae at the surface of asphalt bitumen film surfaces, which we don't implement in our free energy model as shown from equation (2-1) to equation (2-4). Our current simulation is a binary coupling of Phase-field model and Thermal model. In the future we will consider a trinary coupling of Phase-field model, Thermal model and Crystallization model.

Compare Figure 4-1, Figure 4-2, Figure 4-3 with Figure 4-7, note that the “bright” spots in AFM figures finally disappear during the heating process and it corresponds to the phase-diffusion process in our simulation. Since these spots are not caused by surface tension as proved in Reference (10), it is reasonable to believe the spots are generated during one possible thermal process which causes phase separation during the making of sample, with stress concentration surrounding. Identify the “bright” spot as one phase while other as a different phase, the heating process diffuse the two phases and eliminate the stress concentration as shown in Figure 4-7.

Note that our current simulation can preliminarily explain the possible causes of AFM results from Figure 4-1 to Figure 4-4. Further experiment and research on the “bright” spots and

different phases as well as bumble-bee structure are needed to determine the exact properties of them.

4.3.2 Mechanical approach

In this section, we are trying to understand the self-healing process from the mechanical view. The phase field variable ϕ is used to identify the intact solid (+1) and the fully broken phase inside the crack (-1). The system is driven by the chemical potential, which is the variation of the free energy with respect to the phase-field variable.

4.3.2.1 System preference and phase-field equations

Note that during the asphalt healing process, generally there are three stages [1]: wetting of two surfaces, instantaneous strength gain and long-term strength gain resulting from molecular diffusion. In Phase-field model, we are only able to simulate the first stage but unable for the second. Governing equations from equation (2-1) to equation (2-8) are also valid in this approach where the double well potential is set as $f_{loc} = \frac{\lambda}{4\epsilon^2}(1 - \phi)^2(1 + \phi)^2$ and the gradient energy is $f_{gr} = \frac{1}{2}\lambda|\nabla\phi|^2$. Here λ is the mixing energy density; and ϵ is used to represent the interface thickness. We use the non-conserved Allen-Cahn equation

$$\frac{\partial\phi}{\partial t} = -M\psi \tag{4-1}$$

where M is the mobility parameter and ψ is the chemical potential

$$\psi = \frac{\delta F}{\delta \phi} = -\nabla \cdot \lambda \nabla \phi + \frac{\lambda}{\epsilon^2} (\phi^2 - 1) \phi \quad (4-2)$$

The mobility parameter is usually expressed as $M = \chi \xi^2$ where ξ is called the mobility tuning parameter and τ is used to represent the interface thickness.

Figure 4-5 shows an even-well double well potential, in which the system prefers the energy state $\phi = -1$ (broken vacuum) and the energy state $\phi = +1$ (intact solid) equally. However, with the effect of the elastic energy, the double well potential will become uneven as show in Figure 4-8. The system prefers the state $\phi = -1$ since it is a lower energy state. By setting appropriate initial conditions, we can get sufficient large perturbation near the state $\phi = +1$ that overcome the energy barrier and reach the minimum stable state $\phi = -1$. Physically, we can understand it as an appropriate environmental condition to initiate the asphalt cracking process. On the other hand, if there does not exist elastic energy affecting the system, the gradient energy will dominate and self-healing occurs.

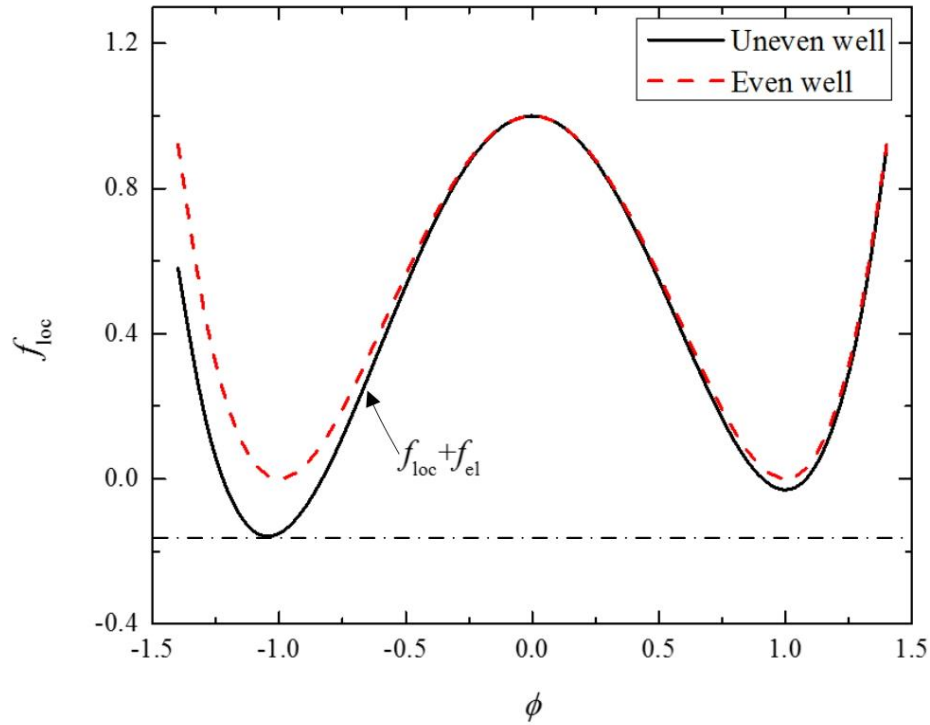


Figure 4-8 Uneven double well potential

Since the self-healing is the inverse process of cracking from mechanical view, equation (3-1) to equation (3-32) are employed here for numerical simulation.

4.3.2.2 J-integral and simulation results

The total J-integral analysis process is similar to the cracking analysis in Chapter 3. For self-healing, note that no external loading exists and thus no elastic energy is considered in the whole free energy system. What's more, it is easy to conclude that no traction exists on the broken surfaces as shown in equation (3-24). And thus we can easily get

$$J < 2\gamma \quad (4-3)$$

always holds for any circumstance as long as there exists surface free energy. And it simply means the surface energy will dominate the microstructure evolution process and thus self-healing happens.

With the above governing equations, we establish a two-dimensional finite element model in COMSOL for the fracture and self-healing analysis. A fixed Eulerian mesh is used to describe the internal interfaces between the intact solid and crack void. Six-node triangular elements (P2) are used in our finite element calculations. 31,254 elements are used in the initial mesh. The surface free energy is $\gamma = 183.77 \text{ J/m}^2$ and the elastic modulus $E = 5.8 \text{ MPa}$. The mesh refines adaptively at the interface to resolve the ϕ profile across the interface. We consider plane strain and the computational domain is a square with side length $L = 0.1 \text{ m}$. We choose the interfacial thickness $\epsilon = 0.01 L = 0.001 \text{ m}$ and the initial crack length $a = 20\epsilon = 0.02 \text{ m}$. Because of the diffuse nature of the phase-field method, we need to impose a finite crack width, which we use $W = 0.005 \text{ m}$ in this simulation. The finest mesh size is set to be $\Delta x = \frac{1}{33} W$ (i.e., $\epsilon \approx 6.6\Delta x$) which sufficiently resolves the diffuse interface.

Figure 4-9 shows the cracking and self-healing process of the formed crack. Each time instant t_i refers to the corresponding left figure. At time t_1 and t_2 , we apply tension loading on the top and bottom boundary and thus crack propagates. And then we don't apply any loading and the self-healing occurs as shown from time t_3 to t_6 . It is seen that due to the surface free energy, the initial formed crack begins to shrink and gradually disappear as we theoretically proved. It should be noted that ϕ may not be exactly in $[-1, 1]$ in the simulations. However, the deviation is always less than 2%, and therefore can be neglected. And, consider equation (34), it is easy to understand Garcia's finding (2011) that self-healing is always happening once a crack is formed.

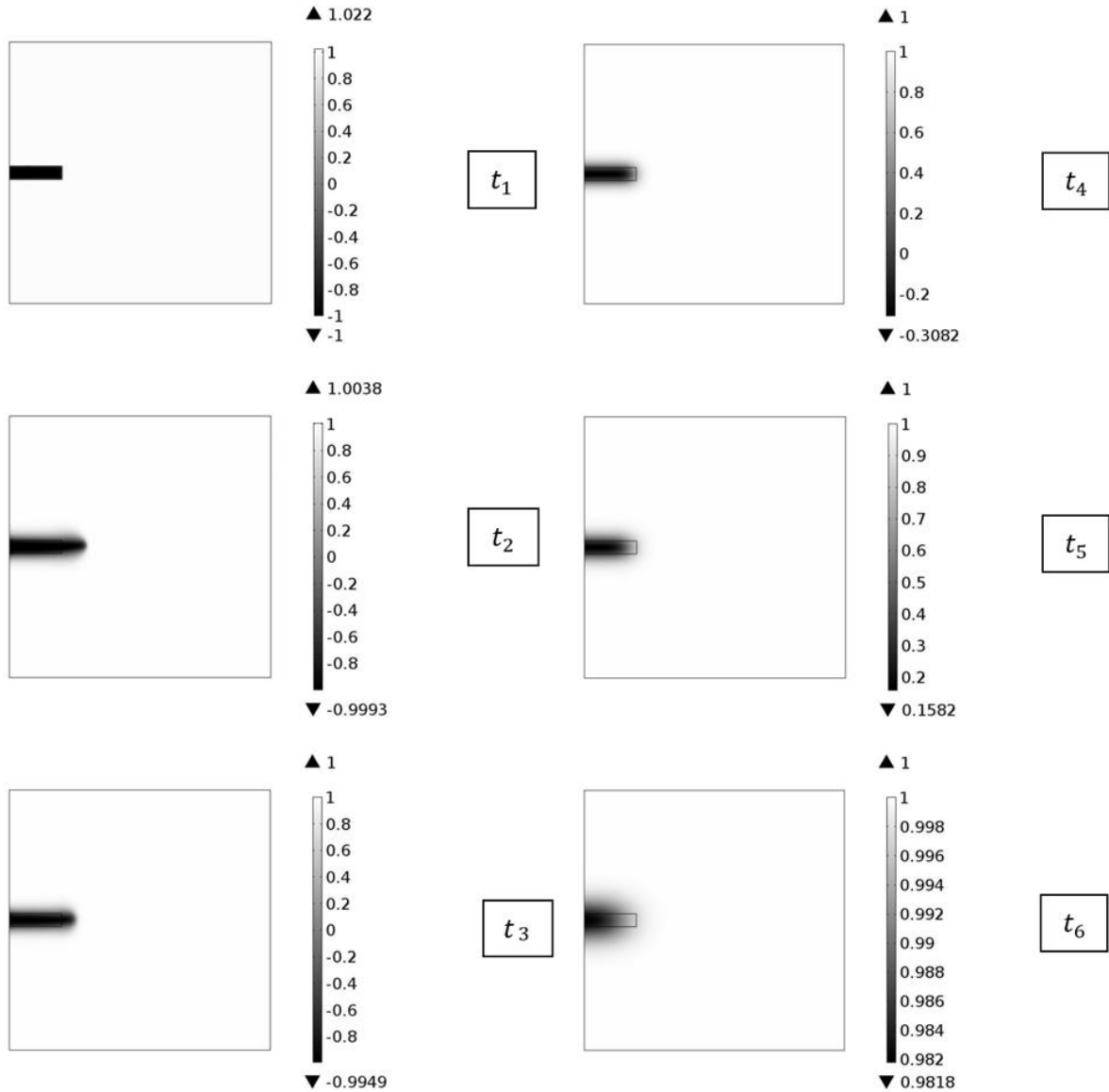


Figure 4-9 Cracking and self-healing at different time steps

4.4 Summary and conclusions

In this section, we presented a study of asphalt self-healing mechanism from two approaches based on the Phase-field Model: first, the general understanding of self-healing and fracture is that the initiation and disappearing of micro-cracks are relevant to material re-arrangement, i.e.

phase separation phenomenon; second, we present a model to characterize the self-healing process of a formed crack from the mechanical view. It was discovered that the surface free energy is the key factor that causes the initial cracks shrink and then gradually disappear in asphalt, as temperature increases.

However, there are still some limitations in our study: first, we still don't know the exact physical properties of the separated phases during the thermal cycling experiment; second, we are currently still on the way to "understand" the self-healing mechanism lacking of accurately quantitative measurements of the healing properties. We are planning to use a comprehensive Multi-phase model that considers both of the material chemistry and mechanical property to further investigate the self-healing phenomenon of asphalt in the future.

REFERENCES

1. Bommavaram, R., Bhasin, A. and Little, D. 2009. Determining Intrinsic Healing Properties of Asphalt Binders. Transportation Research Record: Journal of the Transportation Research Board, No. 2126, Transportation Research Board of the National Academies, Washington, D.C., pp. 47-54. DOI: 10.3141/2126-06.
2. Qiu, J., M.F.C van de Ven, Wu, S.P. and Yu, J.Y. 2011. "Molenaar. Investigating self healing behavior of pure bitumen using Dynamic Shear Rheometer", *Fuel*, 90 (2011) 2710-2720. DOI: 10.1016/j.fuel.2011.03.016.
3. Liu, Q., Garcia, A., Schlangen, E. and Martin van de Ven. 2011. "Introduction healing of asphalt mastic and porous asphalt concrete", *Construction and Building Materials* 25:3746-3752.

4. Garcia, A. 2012. "Self-healing of open cracks in asphalt mastic", *Fuel*, 93: 264-272. DOI: 10.1016/J.fuel. 2011.09.009.
5. Bhasin, A., Bommavaram, R., Greenfield, M. and Little, D. 2011. "Use of Molecular Dynamic to Investigate Self-Healing Mechanisms in Asphalt Binders", *Journal of Materials in Civil Engineering*, Vol. 23, No.4.
6. Branthaver, J.F. 1993. SHRP-A-368: binder characterization and evaluation, volume 2: chemistry. Washington, DC: Strategic Highway Research Program, National Research Council.
7. Lu, X. and Redelius, P., 2006. Compositional and structural characterization of waxes isolated from bitumens. *Energy and Fuels*, 20, 653– 660.
8. Senra, M. 2009. Role of polydispersity and cocrystallization on the gelation of long-chained n-alkanes in solution. *Energy and Fuels*, 23, 5947– 5957.
9. Pauli, T., Grimes, R. W., Beemer, A. G., Turner, T.F. and Branthaver, J.F. 2011. "Morphology of asphalts, asphalt fractions and model wax-doped asphalts studied by atomic force microscopy", *International Journal of Pavement Engineering*. iFirst article, 1-19. DOI: 10.1080/10298436.2011.575942.
10. Kringos, N., Schmets, A., Scapas, A. and Pauli, T. 2011. "Towards an understanding of the self-healing capacity of asphaltic mixtures", *Heron*. Vol. 56 (2011), No. ½, pp 45-74.
11. Uehara T. 2011. "Computer simulation of Microscopic Stress Distribution in Complex Microstructure Using a Phase Field Model", *Journal of Shanghai Jiaotong University (Science)*, Vol. 16, p. 291-295.
12. Stroud, D. 1973. "Simple Mean-Field Approach to Phase Separation in Liquid-Metal Alloys", *Physical Review B*, Volume 8, No. 4.

13. Kuhn, C., and Muller R. (2010). “A continuum phase field model for fracture.”
Engineering Fracture Mechanics, Vol. 77, 3625-3634.
14. Rice, J. (1968). “A path independent integral and approximate analysis of strain concentration by notches and cracks.” *Journal of Applied Mechanics* 35, 379 – 86.
15. Yue, P., Feng, J., Liu, C. and Shen, J. (2004). “A diffuse-interface method for simulating two-phase flows of complex fluids.” *Journal of Fluid Mechanics*, Vol. 515, 293-317.
16. Griffith, A. A. (1921). “The phenomena of rupture and flow in solids.” *Philosophical Transactions of the Royal Society of London, Seria A*, Vol. 221, 163-197.
17. Yue, P., Zhou, C., Feng, J. (2010). “Sharp-interface limit of the Cahn-Hilliard model for moving contact lines.” *Journal of Fluid Mechanics*, Vol. 645, 279-294.

Chapter 5. A Multi-scale Approach of Mode I crack in ettringite based on Phase-field Theory and Molecular Dynamic Simulation¹

5.1 Introduction

In the pavement industry, one of the most serious problems that may lead to rigid pavement failure is cracking in hydrated cement paste, which may be caused by traffic overloading, thermal loading, etc. The cracking dynamics in cement paste has always been a challenging issue for pavement engineers [1]. Generally, the state-of-art research of the pavement cracking failure is mainly based on the Griffith's Classic Fracture Mechanics on the continuum scale, which needs to clearly depict the crack front conditions and thus may be very complicated to handle topological changes during the cracking. Besides, the current used continuum fracture mechanics is unable to very accurately explain and understand the non-linear mechanical behavior at the crack tip. Many Cohesive Zone Models (CZMs) are proposed [2, 3] to solve this problem but the applicability and accuracy of these models are case by case and cannot be employed in the general fracture process.

¹ Part of this chapter is submitted to Journal of Wuhan University of Technology Materials Science Edition.

Hou, Y., Sun, W., Wang, L. and Pauli, T. (2014). "A Multi-scale approach of Mode I Crack in ettringite based on Phase-field Theory and Molecular Dynamics Simulation." *Journal of Wuhan University of Technology Materials Science Edition*. (Submitted 3/13/2014)

Ettringite, as one of the most important hydration product of cement paste, is our main research target in this section. The fracture mechanism of ettringite needs to be clearly figured out. In order to simulate the fracture concisely and comprehensively from both of macroscopic and microscopic levels, a multi-scale modeling approach combining Phase-field Theory (PFT) and Molecular Dynamic (MD) Simulation so as to connect the continuum scale and atomistic scale is presented in this paper. In this modeling, the whole fracture dynamics are split into two scales:

1. The first is the continuum scale, which is simulated by the mathematical tool Phase-field Theory. As proved in the previous sections, Phase-field Theory can handle the cracking problems on the continuum level. Due to the non-conserved nature of crack growth, the Allen-Cahn dynamics has dominated the phase-field modeling of fracture.
2. The second is the atomistic level. Since the mechanical property at the crack tip is complex due to its atomistic-structure-dependence and unable to be accurately solved by the phase-field system, the Molecular Dynamic Simulation is employed for analysis. The molecular structure of ettringite will be input into the simulation software Large-scale Atomic/Molecular Massively Parallel Simulator (LAMMPS). It is expected that the continuum Phase-field system will control the cracking process, and at the crack tip, MD simulation will dominate. The stress and strain from PFT will be used as the boundary condition in LAMMPS ($P \rightarrow M$) and then MD simulation returns the elastic energy into the two-way coupling system ($M \rightarrow P$). One thing should be noted is that at molecular level, elastic modulus will be dependent on the molecular structure. For consistence, we use the value of elastic modulus calculated in MD Simulation in our continuum Phase-field Model. Figure 5-1 shows the flowchart of our multi-scale modeling scheme.

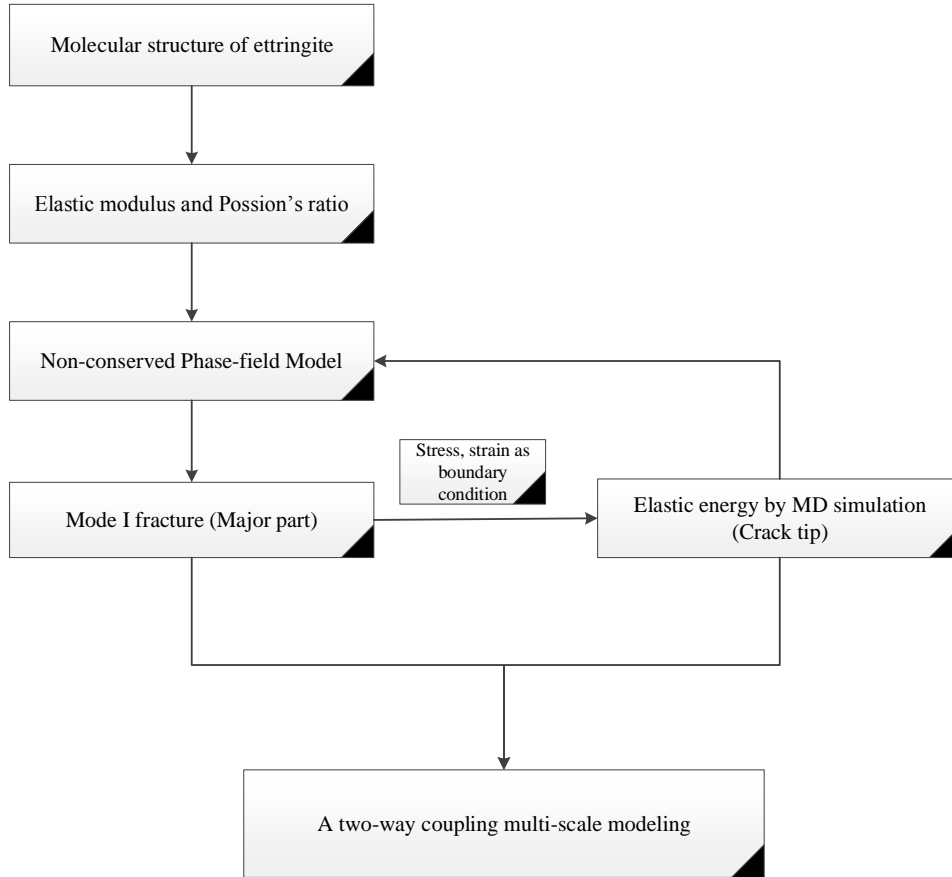


Figure 5-1 Flowchart of multi-scale modeling scheme

Since the Phase-field Theory has been introduced in the previous sections, the emphasis is the Molecular Dynamics Simulation in this section. The detailed Molecular Dynamics Simulation in LAMMPS is conducted by Wenjuan Sun as a research partner. The ultimate goal of this multi-scale approach modeling is to simulate the crack propagation of ettringite under complex loading conditions, which occurs in reality.

5.2 Multi-scale Modeling

For the continuum level, we use Phase-field to calculate the cracking dynamics of ettringite. But one problem raises that we are unable to investigate the very tiny singularity – crack tip since our Phase-field modeling is solved by the numerical finite element method.

And then we apply the MD Simulation at the crack tip to study ettringite - one of the hydration product of cement paste - by using the simulation software Large-scale Atomic/Molecular Massively Parallel Simulator (LAMMPS). The stress and strain information obtained from Phase-field modeling are used as the boundary conditions in LAMMPS. Note that considering the very much complex structure of pavement materials, only typical atomistic structures are picked up for analysis.

It is known that the hydration products of cement paste play very important role in the mechanical behavior of cement concrete and there are mainly four types of cement hydrates: calcium silicate hydrate (C-S-H), calcium hydroxide (CH), "alumina, ferric oxide, tri-sulfate" (AFm) and "Alumina, Ferric oxide, mono-sulfate" (AFt) phases (including ettringite, monosulphate, and monocarbonate, etc. Figure 5-2 shows the volume percentage of each composition in hydrated Portland cement paste after the hydration of 14 months. Among these cement hydration products, ettringite is a calcium aluminium sulfate mineral crystalizing in the trigonal system with the chemical formula of $\text{Ca}_6\text{Al}_2(\text{SO}_4)_3(\text{OH})_{12} \cdot 26\text{H}_2\text{O}$. It plays an important role in the crystallization development of cement hydration products and in the deterioration of hardened cement concrete due to sulphate attack.

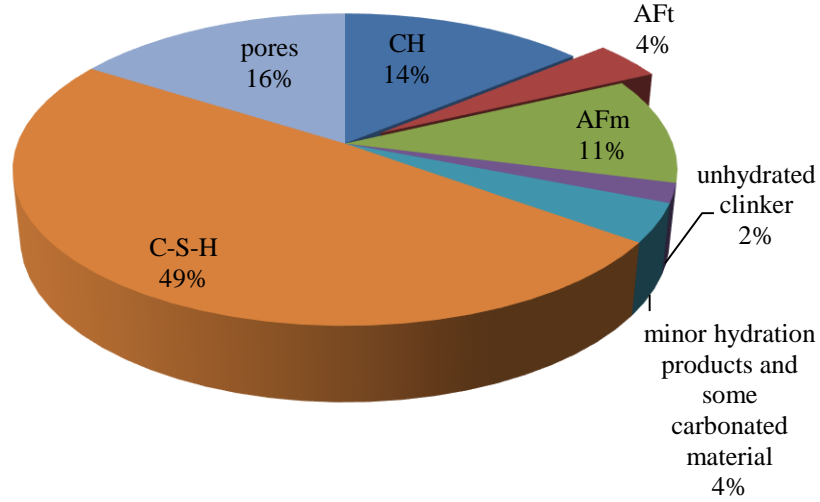


Figure 5-2 Volume percentage of different phases in hydrated Portland cement paste, water/cement ratio = 0.5, hydrated for 14 months

5.2.2 Computational theory

Ettringite molecular structure is established based on ReaxFF force field in LAMMPS; the optimized parameters are documented in a field file with atom positions in a data file from Liu *et al.*'s work [4]. The ReaxFF force field calculates the atomic interactions in ettringite with good accuracy. The total energy in ReaxFF is partitioned in different energy terms as defined by the following equation.

$$E_{totalpotential} = E_{bonds} + E_{angles} + E_{torsions} + E_{H-bonds} + E_{vdW} + E_{coulomb} + E_{lp} + E_{over} + E_{under} + E_{open} + E_{coa} + E_{C_2} + E_{triple} + E_{conj} \quad (5-1)$$

where E_{bonds} is the sum of all bonded pairwise interactions directly derived from bond orders; E_{angles} , $E_{torsions}$, $E_{H-bonds}$, E_{vdW} , and $E_{Coulomb}$ are angle, torsional, hydrogen bond, van der Waal, and

Coulomb interactions, respectively; E_{lp} is the sum of the long pair energy, a penalty for breaking up long pairs in O, N; E_{over} is the sum of overcoordination energy, penalty for overcoordinating atoms; E_{under} is the undercoordination energy, contribution for the resonance of π -electron between undercoordinating atoms; E_{pen} is the penalty for “allene”-type molecules ($H_2C=C=CH_2$); E_{coa} is the energy term due to the contribution of three-body angle conjugation in $-NO_2$ groups; E_{C2} is an energy correction that destabilizes the stability of $C=C$; E_{triple} is a triple bond stabilization energy in CO bonded pairs; E_{conj} describes the contribution of conjugation stability to the molecular energy.

A ReaxFF force field was developed for ettringite to simulate the first principles quantum mechanism interaction in hydrous calcium aluminium sulphate systems (H/Ca/Al/S/O) with good accuracy. The geometries and energies of species and complexes in ettringite were calculated according to density functional theory (DFT); ReaxFF parameters were adjusted with the minimum differences between ReaxFF energies and DFT energies. Figure 5-3 plots a $2 \times 2 \times 1$ molecular triclinic supercell structure, a basic calculation structure in the simulation using LAMMPS. The conformity and structure stability of proposed molecular structure using the aforementioned ReaxFF force field parameters were validated in an isothermal-isobaric (NPT) ensemble at room-temperature.

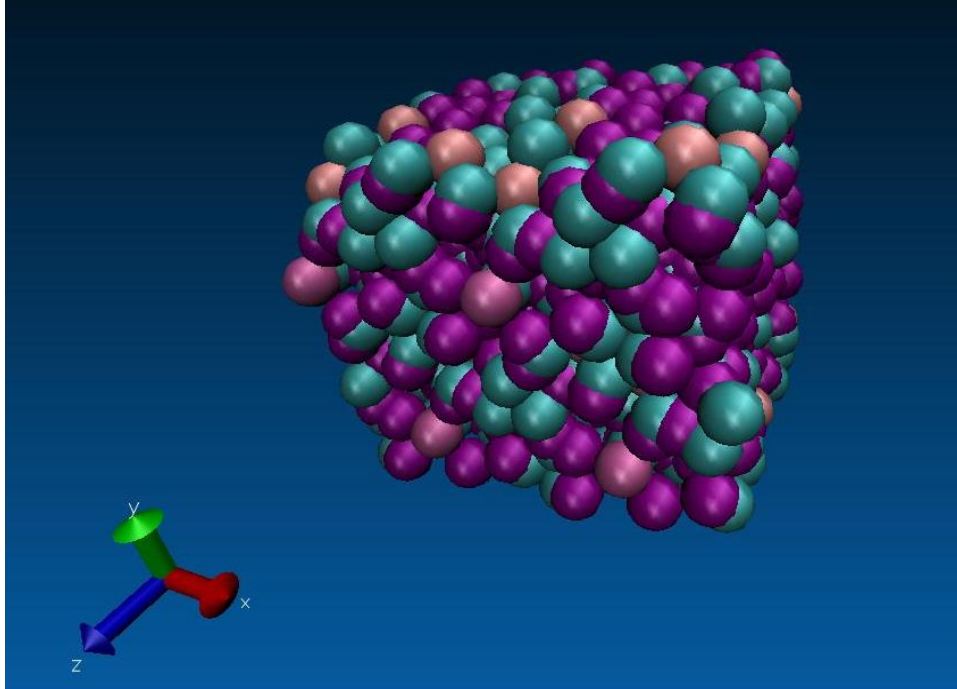


Figure 5-3 $2 \times 2 \times 1$ supercell molecular structure of ettringite (Green is the Oxygen atom; red is the Hydrogen atom; pink is the Calcium atom; Sulphate and Aluminium atoms cannot be seen from this point of view in the figure.)

5.2.3 Multi-scale Approach

As stated in the introduction section that the two material properties elastic modulus and Poisson's ratio used in our Phase-field Model are obtained from the MD Simulation, which are shown in Table 5-1. Elastic constants were determined from the stress-strain relationships in LAMMPS simulations within very small strain ranges, where the stress-strain relationship is linear.

Table 5-1 Elastic constants of ettringite by MD Simulation

Elastic constants (GPa)	MD Simulation
C_{11}	30
C_{12}	20.1
C_{13}	20
C_{14}	1.5
C_{33}	52
C_{44}	12.2
C_{66}	4.9
Bulk modulus (K)	25.8
Shear modulus (G)	12.2
Poisson's ratio (ν)	0.335

We then establish our marco level system by using a two-dimensional finite element model in COMSOL. A fixed Eulerian mesh is used to describe the internal interfaces between the intact solid and crack void. The mesh refines adaptively at the interface, as shown in Figure 5-4, to resolve the ϕ profile across the interface. We consider plane strain and the computational domain is a square with side length $L = 0.1 \mu m = 100nm$. We choose the interfacial thickness $\epsilon = 0.01 L = 1\mu m$ and the initial crack length $a = 20\epsilon = 20nm$. Because of the diffuse nature of the phase-field method, we need to impose a finite crack width, which we use $W = 5nm$ in this simulation.

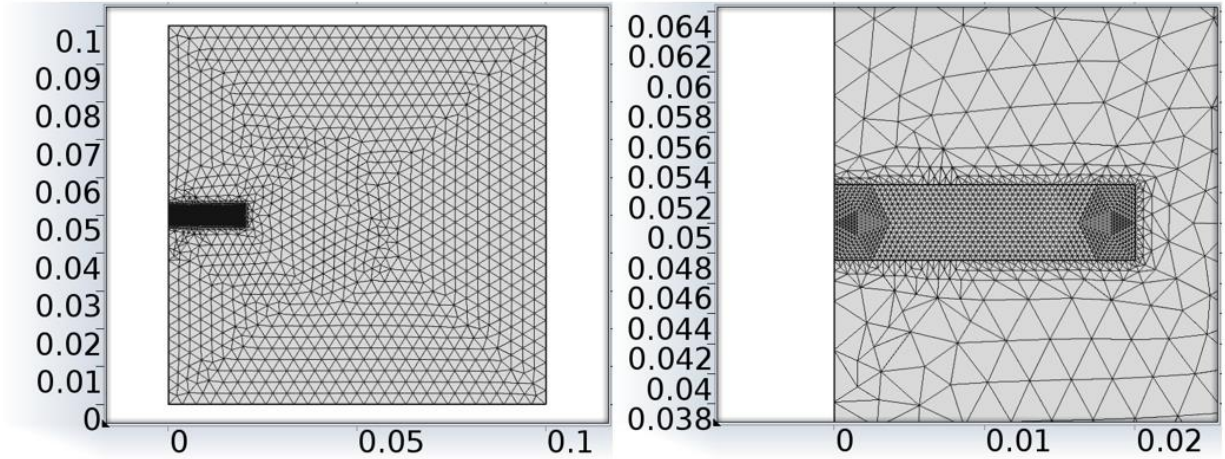


Figure 5-4 (a) Unstructured triangular mesh generated by COMSOL with interfacial refinement. (b) Magnified view of the crack

Pure tension loading is applied on top and bottom boundaries as $\sigma(t) = \frac{\sigma_0}{t_0} \cdot t$ where $\frac{\sigma_0}{t_0} = 5 \times 10^8 \frac{\text{N}}{\text{m}^2\text{s}}$ in our simulation.

Our multi-scale coupling steps are as follows: we first run the Phase-field model as the start-force of our system. After running for a certain time t_1 , we then use the stress and strain obtain at this time instant as the periodical boundary condition and input into the LAMMPS and calculate for a certain time t_{MD} . Then the calculated elastic energy is substituted and renew the total system elastic energy f_{el} . The given constant engineering strain rate of 0.001 fs^{-1} is applied. The ensemble was equilibrated by performing an energy minimization of the system with a stopping tolerance for energy of $1 \times 10^{-6} \text{ Kcal/mole}$ and for force of $1 \times 10^{-6} \text{ Kcal/mole-Angstrom}$. Timestep was set as 0.002 fs , and a total of 1000 fs was applied. The deformations of the ettringite molecules in three directions and the stresses of the whole ensemble were documented for each

timestep, and the last 400 fs was used for data collection. 20,480 atoms are calculated in LAMMPS.

What should be mentioned is that in order to simulate natural defects such as dislocation in the real situation, we manually assign the defects in the structure as shown in Figure 6. Under tension loading, the initial defects will begin to propagate and finally cause the failure of the crystal structure.

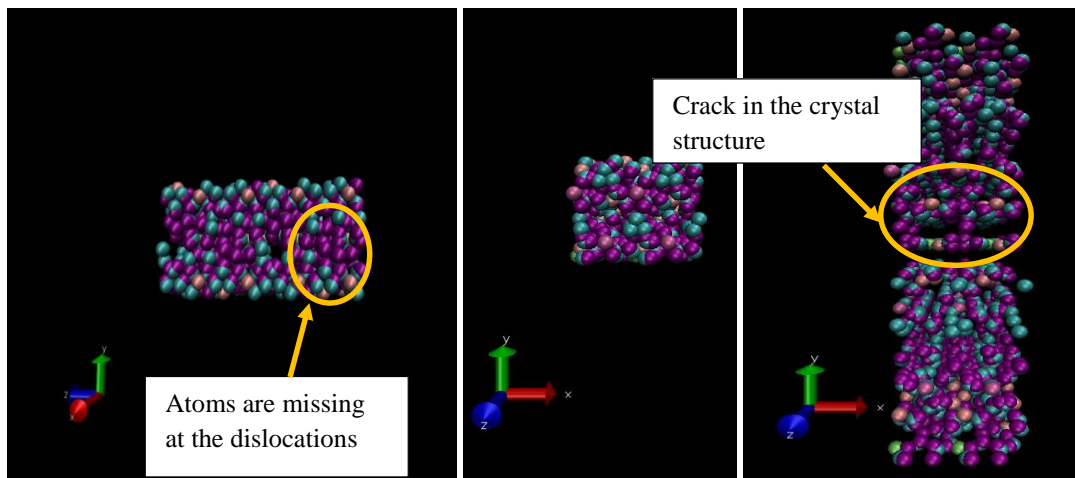


**Figure 5-5 Molecular structure of ettringite 2x4x1 in the molecular dynamics (MD) model:
(a) & (b) initial view molecular structure of ettringite from different views (c) molecular
structure after tension failure**

The total energy in LAMMPS is expressed as the summation of the potential energy and the kinetic energy as

$$E_{Total} = E_{potential} + E_{kinect} \quad (5-2)$$

If we consider from the structure aspect, the total energy during the fracture process could also be divided as the plastic work $W_{plastic}$ and elastic energy $E_{elastic}$, where the plastic work can be calculated as variation of potential energy at 0K as

$$W_{plastic} = \Delta E_{potential}(0K) \quad (5-3)$$

And, in order to find the variation, we need to identify the minimum value of the potential energy at the given time t where the Molecular Statics reads

$$E_{potential}^{min}(t) = \min_{\mathbf{R}=(r_1, \dots, r_N)} E_{potential}(\mathbf{R}(t)) \quad (5-4)$$

where $\mathbf{R} = (r_1, \dots, r_N)$ represents the atom coordinates.

And correspondingly, the plastic work at time t is calculated as

$$W_{plastic}(t) = E_{potential}^{min}(t) - E_{potential}^{min}(0) \quad (5-5)$$

Combined equation (5-2), (5-3), (5-4) and (5-5) and obtain the elastic energy. And then the overall multi-scale modeling of ettringite fracture can then be simulated as shown in Figure 5-6. The snapshots are taken at time step = 0, 1.51s, 1.53s, 1.55s, 1.57s and 1.59s, respectively. $\gamma = 18.997 \text{ J/m}^2$. $E = 2G(1 + \nu) = 32.574 \text{ GPa}$. $K_{IC} = 800 \text{ kN} \cdot \text{m}^{-\frac{3}{2}}$. It can be clearly seen that crack propagates along the x direction while there is a diffuse interface between the crack phase and the intact phase.

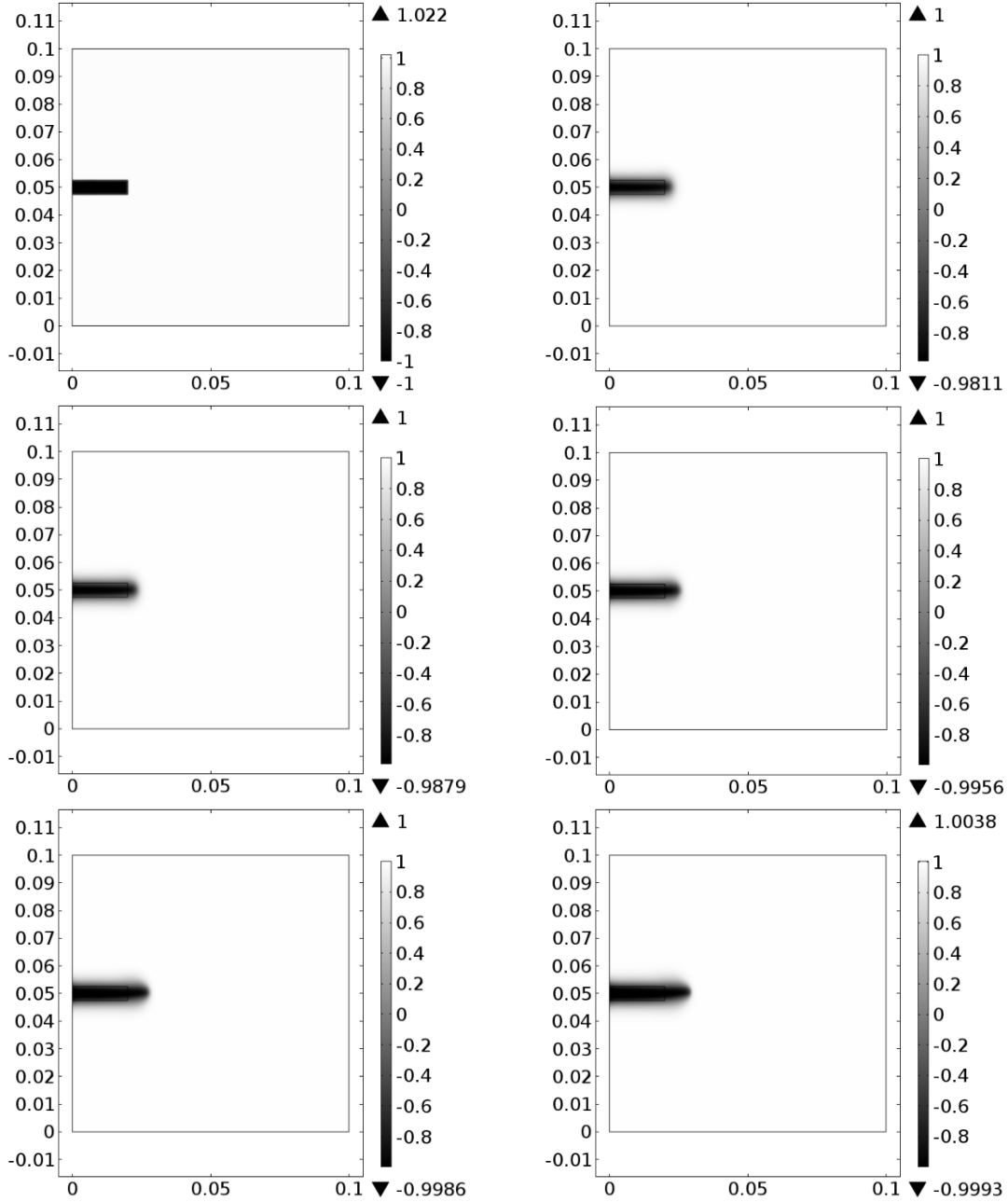


Figure 5-6 Crack propagation in the multi-scale modeling at different time instants

Note that surface energy is determined by

$$\gamma = \frac{1}{2} G_c = \frac{K_{Ic}^2(1-\nu^2)}{2E} \quad (39)$$

Figure 5-7 shows the crack tip region in multi-scale modeling at 1.53s as the red square. Note that for different time instants, the crack tip region position is different since it moves with the developing of the crack. In order to keep the consistence in the whole calculation, the size of the crack tip region is always set as $0.01\mu\text{m} \times 0.01\mu\text{m}$.

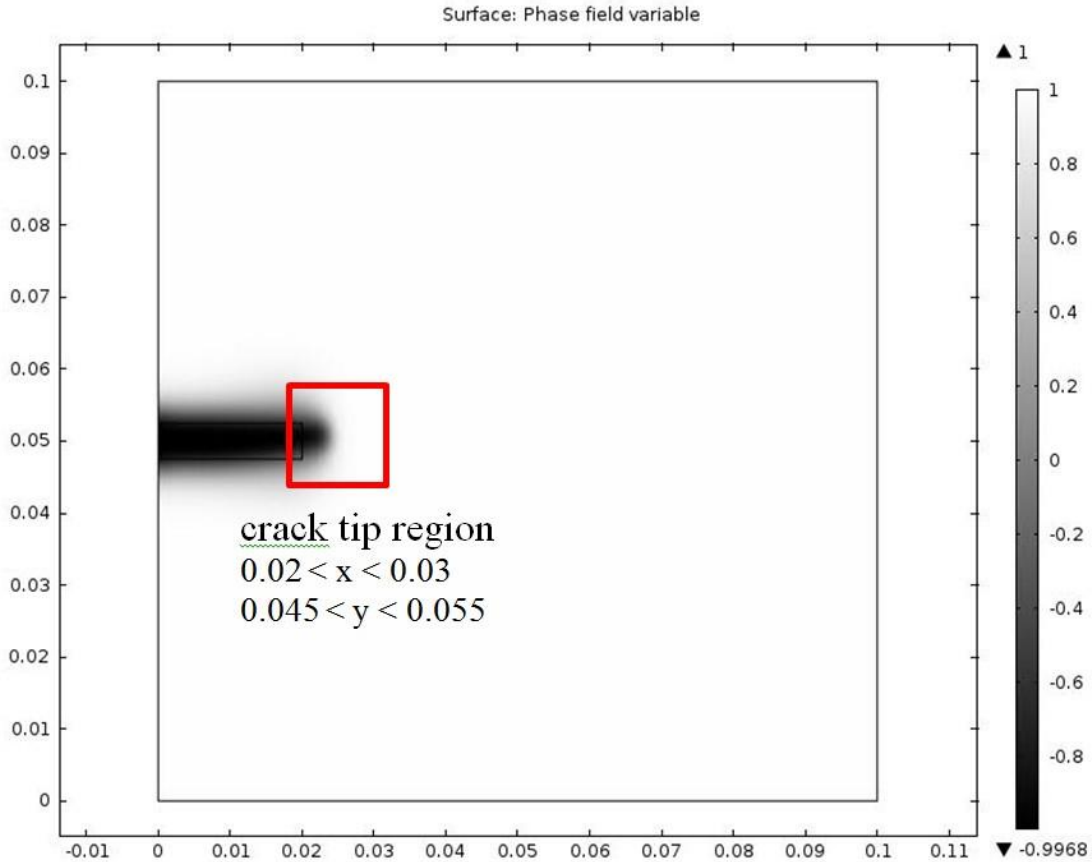


Figure 5-7 Crack tip region in multi-scale system at $t = 1.53\text{s}$

We then compare the maximum stress in Phase-field model and MD simulation shown in Table 2. It is seen that the maximum stress in MD simulation is almost ten times more than the results obtained from continuum mechanics. This is reasonable because, in MD simulation, the maximum stress refers to the magnitude of strength that the molecular structure resist to break,

which means that at this level, this maximum strength can be considered as the yield strength of ettringite. The maximum stress in Phase-field increases since the external loading force causes an increasing elastic deformation.

Table 5-2 Stress comparison between Phase-field and MD

Time	External stress (Pa)		Phase-field stress (Pa)	MD Simulation (Pa)
1.51	7.55E+07	Maximum	1.67E+08	1.15E+09
		Minimum	1.27E+07	
1.53	7.65E+07	Maximum	1.85E+08	
		Minimum	1.33E+07	
1.55	7.75E+07	Maximum	2.01E+08	
		Minimum	1.40E+07	
1.57	7.85E+07	Maximum	1.97E+08	
		Minimum	1.44E+07	

If we consider the critical state as the phase-field variable value of the node that just in front of the crack reach -1, the von Mises stress distribution before multi-scale coupling at 1.53s is shown in Figure 5-8. A magnified view at the crack tip shows the stress concentration occurs at the crack tip. However, if consider from the molecular structure level, it is easy to conclude that the stress distribution should be different. Figure 10 shows the von Mises stress distribution at the crack tip after the multi-scale coupling, where maximum stress will occur in some particular regions that correspond to some particular atom bonds (we are still doing research on what kind of atom bonds they are). The comparison between Figure 5-8 and Figure 5-9 demonstrates that

our multi-scale coupling is necessary in order to understand the intrinsic mechanism of ettringite fracture.

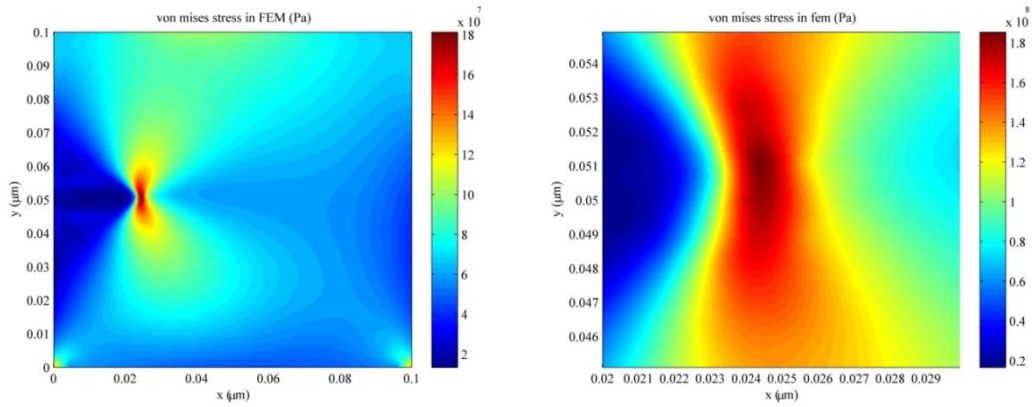


Figure 5-8 Von mises stress distribution and magnified view of crack tip region by Phase-field at 1.53s

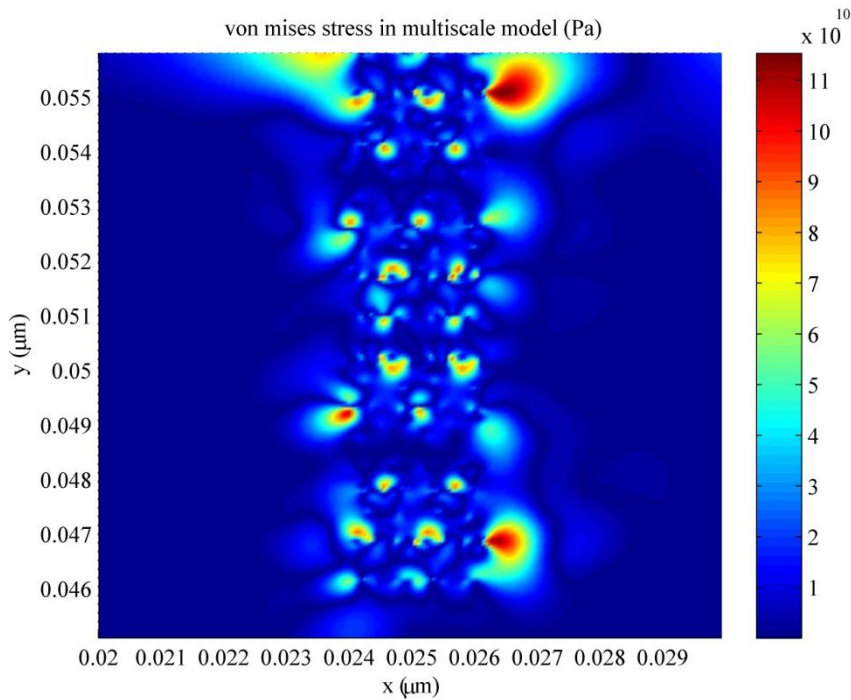


Figure 5-9 von Mises stress distribution after the multi-scale coupling

5.3 Summary and discussion

In this section, we present a multi-scale modeling of Mode I fracture of ettringite based on the non-conserved Phase-field Theory and Molecular Dynamic Simulation. Theoretical analysis has shown that our Phase-field Theory agrees well with the classic Griffith's theory on the continuum level. MD simulations of the ettringite molecular structure were conducted in a NPT ensemble using LAMMPS. The two-way coupling of the two scales on elastic energy constitutes our multi-scale modeling. Overall, compared with the classic fracture mechanics, the Phase-field model does not need to explicitly treat the crack surface and can easily handle the typological changes on the macro-level while MD simulation can better explain the intrinsic mechanism at the crack tip where continuum mechanics are unable to. The combination of the two overcomes the shortcoming of each and thus presents a promising and innovative method for modeling the Mode I fracture of ettringite for better quantitative understanding. Future research should be conducted on the derivation of this multi-scale system to more pavement materials.

REFERENCES

1. Lura P., Ole Mejihede Jensen, Jason Weiss. Cracking in cement paste induced by autogenous shrinkage. *Materials and Structures* (2009) 42: 1089-1099.
2. Li, H. and Chandra, N. (2003). "Analysis of crack growth and crack-tip plasticity in ductile materials using cohesive zone models." *International Journal of Plasticity*, Vol. 19, 849-882.
3. Elices, M., Guinea, G.V., Gomez, J. and Planas, J. (2002). "The cohesive zone model: advantages, limitations and challenges." *Engineering Fracture Mechanics*, Vol. 69, 137-163.

4. Liu, L., Jaramillo-Botero, A., Goddard, III, W. and Sun, H. (2012). “Development of a ReaxFF Reactive Force Field for Ettringite and Study of its Mechanical Failure Modes from Reactive Dynamics Simulations.” *The Journal of Physical Chemistry*, Vol. 116, 3918-3925.

Chapter 6. Conclusions and future work

6.1 Overview

Cracking resistance and self-healing are two important material properties of asphalt. Both mechanisms are very complicated and up to now not completely understood by pavement engineers. There have been many researches and it is expected that more are needed to solve the problems in the future.

The traditional way to solve the fracture problem is based on Griffith's theory. Stress Intensity Factor, as one of the most important fracture parameter, is used to depict the fracture process. Another emerging method is the Molecular Dynamic (MD) Simulation. It has the advantage to explain the cracking mechanism from the fundamental molecular structure. But there are two problems if we want to employ the MD simulation in asphalt binder cracking: first is that we need to know the exact molecular structure of asphalt which is unable to since there's lack of such research currently; second there will be massive calculation for even a micro-scale crack (up to 10^9 atoms).

The Phase-field method, as shown in this thesis, could capture the interface development and further describe the microstructure evolution naturally. The application of phase-field method in asphalt mechanical performance evaluation is reasonable and has satisfactory accuracy in almost every research aspect in this PhD thesis.

6.2 Major findings

The major findings of this study are shown below:

- 1) Phase-field Method is able to calculate the residual stress of asphalt binder under a given thermal loading process by using the simplified Marcusson model of asphalt chemistry. Asphalt is considered to have two main components resin and oil that will affect the physical properties. By doing a one-way coupling, the effect of the phase separation process on the residual thermal stress is studied. An overall view of the thermal loading process demonstrates that phase separation does have a significant effect on the residual stress. Due to the phase separation, the stress distribution becomes non-uniform and especially, stresses in some regions of the system show an increase while stresses in some other regions show a large decrease. The main reason why it behaves so is that the elastic modulus is not uniform after phase separation. High stress gradient zone occurs at the interface between the resin phase and the oil phase. It appears and moves with the interface. Our calculation results have a good agreement with the previous research results;
- 2) The non-conserved phase field model could be used for cracking failure (Mode I, Mode II, Mixed mode and crack interaction) in asphalt binders at a low temperature. Tests on two types of specimens, namely, the direct tension specimen and the three-point bending specimen, are simulated. Experiments of direct tension tests are also conducted to verify the reasonable choice of fracture properties of asphalt binder. The critical loadings that lead to crack propagation agree very well with those predicted using classical fracture mechanics. Due to the extra dissipation associated with the phase-field equation, the critical loads obtained in the simulations are always slightly greater than those predicted by classical fracture mechanics. Overall, compared with the classic fracture mechanics, the Phase-field model does not need to explicitly treat the crack surface and can easily

handle the topological changes. It is capable of simulating different fast fracture in asphalt binder with reasonable accuracy, which will lead to a better quantitative understanding of the binder behavior.

- 3) The multi-scale modeling based on the non-conserved Phase-field Theory and Molecular Dynamic (MD) Simulation could be employed to analyze the Mode I fracture of ettringite. MD simulations of the ettringite molecular structure were conducted in a NPT ensemble using LAMMPS. The two-way coupling of the two scales on elastic energy constitutes our multi-scale modeling. Overall, compared with the classic fracture mechanics, the Phase-field model does not need to explicitly treat the crack surface and can easily handle the topological changes on the macro-level while MD simulation can better explain the intrinsic mechanism at the crack tip where continuum mechanics are unable to. The combination of the two overcomes the shortcoming of each and thus presents a promising and innovative method for modeling the Mode I fracture of ettringite for better quantitative understanding. Future research should be conducted on the derivation of this multi-scale system to more pavement materials.
- 4) Phase-field method could be used to investigate the asphalt self-healing mechanism from two approaches: first, the general understanding of self-healing and fracture is that the initiation and disappearing of micro-cracks are relevant to material re-arrangement, i.e. phase separation phenomenon; second, we present a model to characterize the self-healing process of a formed crack from the mechanical view. It was discovered that the surface free energy is the key factor that causes the initial cracks shrink and then gradually disappear in asphalt, as temperature increases.

6.3 Recommendations for future work

Although the current research of application of Phase-field method on pavement materials has made some progress, there are still many limitations of this work and thus the corresponding future work should be conducted in order to overcome the shortcomings and develop this theory.

- 1) In the thermal cycling loading experiments of asphalt, we can see phase separation happens in the test samples. Our Phase-field model is only able to depict the phenomenon but unable to catch the crystallization that happens at the same time. Besides, our phase-field model is binary system, which greatly limits the applicability since in the reality, there always exist more than only two phases. In the future, research should be carried out on the Multi-phase model. One major challenge we are facing during the simulation is that there exist a strong relationship between the interface and the stress distribution but there lacks the explanation of the mechanism from the microscopic view. The Molecular Dynamic simulation as a further study is expected to solve this problem.
- 2) For simulation of asphalt cracking by Phase-field, there also exist some limitations of the current model. In the real cracking process, there may be energy loss due to temperature variance, plastic deformation, viscous dissipation, etc.; the asphalt binder may not be linearly elastic, especially at a temperature above -20°C ; the asphalt binder, which is a mixture of several components, may exhibit nonhomogenous properties and require multi-component simulations. All these issues will be addressed in our future work. The fatigue cracking, which is one of the principal distresses that affect the design life of asphalt pavements, also needs to be investigated. In the near future we plan to study how

the visco-elastic property will affect the asphalt cracking with the introduction of the cohesive zone at crack tip;

- 3) The accuracy of our experimental results is limited by the instrument, e.g. the mixed mode fracture experiment. Our future plan is to determine the fracture energy obtained by equation (3-50) by using more accurate experiment methods. Besides, we are planning to expand our research area to the asphalt mixtures. The numerical model presented in this paper needs an existing crack as the initial condition, which limit the applicability of Phase-field Method on the mixed mode fracture of asphalt binder. We are planning to expand the research to a broader situation which does not need an existing discontinuity.
- 4) For the self-healing modeling, that are some limitations in our current study: first, we still don't know the exact physical properties of the separated phases during the thermal cycling experiment; second, we are currently still on the way to “understand” the self-healing mechanism lacking of accurately quantitative measurements of the healing properties. We are planning to use a comprehensive Multi-phase model that considers both of the material chemistry and mechanical property to further investigate the self-healing phenomenon of asphalt in the future.

What should be mentioned is that the necessary improvement for phase field application in asphalt cracking is the introduction of viscoelastic property as suggested above, which we do not discuss in our current model. The possible way to solve the viscoelastic cracking by phase field is consider the decomposition of stress field to elastic part and viscous part as [1]

$$\sigma_{ik}^{total} = \sigma_{ik}^{el}(\varepsilon_{ik}) + \sigma_{ik}^{vis}(\dot{\varepsilon}_{ik}) \quad (6-1)$$

The elastic part can be obtained according to Hooke's law as

$$\sigma_{ik}^{el} = \frac{E}{1+\nu} (\varepsilon_{ik} + \frac{1}{1-2\nu} \delta_{ik} \varepsilon_{ii}) \quad (6-2)$$

where δ_{ik} is Kronecker delta, gives as

$$\delta_{ik} = \begin{cases} 0 & \text{if } i \neq k \\ 1 & \text{if } i = k \end{cases} \quad (6-3)$$

It should be mentioned that Einstein summation convention is used here for conveniences.

The viscous part could similarly be obtained as [1]

$$\sigma_{ik}^{vis} = \frac{\eta}{1+\zeta} (\dot{\varepsilon}_{ik} + \frac{1}{1-2\zeta} \delta_{ik} \dot{\varepsilon}_{ii}) \quad (6-4)$$

where η and ζ are two viscosity constants defined similar to the elastic constants in equation (6-2).

And in phase-field model, only elastic stress will contribute to cracking, the viscous part will not have contribution. Figure 6-1 shows the flowchart of phase-field method in solving Mode I viscoelastic fracture.

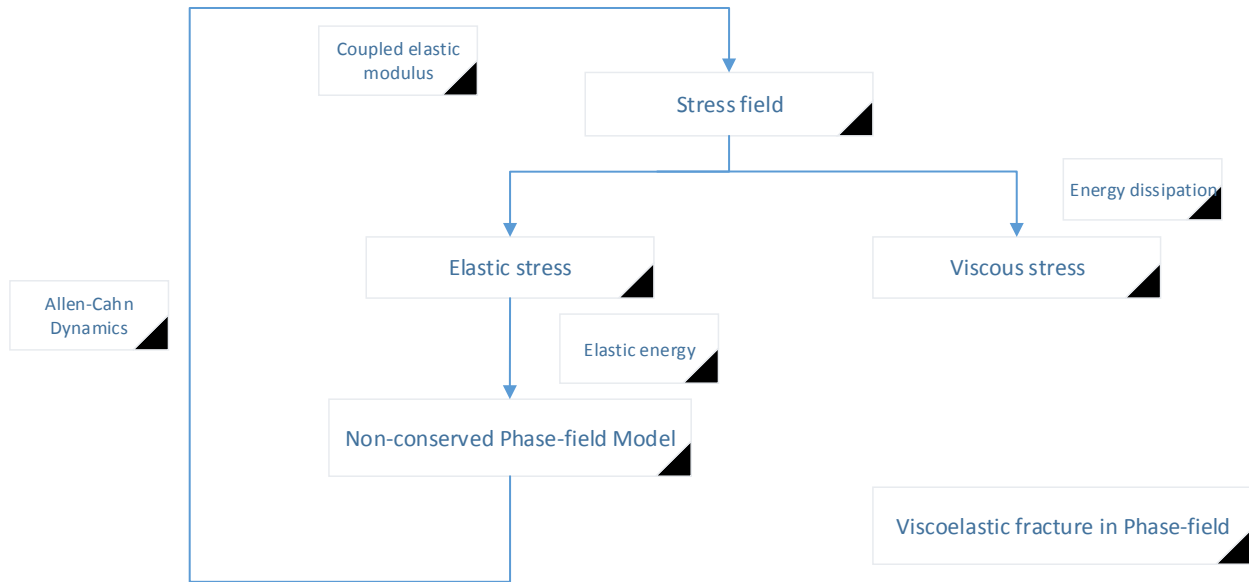


Figure 6-1 Phase-field Mode I viscoelastic fracture calculation flowchart

REFERENCES

1. Fleck, M. Solid-state transformations and crack propagation: A phase field study. Phd thesis, University of Bayreuth, Germany, 2011.

PUBLICATIONS SUMMARY

Parts of this thesis are published in the following technical papers and proceedings.

1. Hou, Y., Yue, P., Xin, Q., Pauli, T, Sun, W. and Wang, L. (2014) “Fracture Failure of Asphalt Binder in Mixed Mode (Mode I & Mode II) by Using Phase Field Model.” *Road Materials and Pavement Design*, 15(1): 167-181. DOI: 10.1080/14680629.2013.866155.
2. Hou, Y., Wang, L., Pauli, T., and Sun, W. (2014). “An Investigation of Asphalt Self-healing Mechanism Using Phase-field Model.” *Journal of Materials in Civil Engineering*. DOI: 10.1061/(ASCE)MT.1943-5533.0001047, in press, proofreading.
3. Hou, Y., Wang, L., Yue, P., Pauli, T and Sun, W. (2013). “Modeling Mode I Cracking Failure in Asphalt Binder by Using Nonconserved Phase-Field Model.” *Journal of Materials in Civil Engineering*, 26(4), 684-691.
4. Hou, Y., Wang, L., Yue, P., and Pauli, T. (2013). “Mode II Cracking Failure in Asphalt Concrete by Using A Non-conserved Phase Field Model.” *Multi-Scale Model. & Charact. Of Infrastruct. Mater.*, RILEM 8, pp 127-138.

And four technical papers are currently in review.

1. Hou, Y., Sun, W., Wang, L. and Pauli, T. (2014). “A phase field approach of viscoelastic fracture failure in asphalt mixture.” *International Journal of Pavement Engineering*. (Submitted 2/16/2014)
2. Hou, Y., Yue, P., Wang, L. and Sun, W. (2014). “Fracture Failure in Crack Interaction by Using a Phase Field Approach.” *Materials and Structures*. (Submitted 1/21/2014)
3. Wang, L., Hou, Y., Yue, P and Pauli, T. (2014). “A phase field approach for computing residual thermal stress in asphalt binder.” *The Baltic Journal of Road and Bridge Engineering*. (Submitted 1/21/2014)
4. Hou, Y., Sun, W., Wang, L. and Pauli, T. (2014). “A Multi-scale approach of Mode I Crack in ettringite based on Phase-field Theory and Molecular Dynamics Simulation.” *Journal of Wuhan University of Technology Materials Science Edition*. (Submitted 3/13/2014)